Federal University of Pernambuco
Technology and Geosciences Center
Civil Engineering Department
Postgraduate Program in Civil Engineering

Artur Castiel Reis de Souza

Conservative Multiscale Strategies for Multiphase Flow on Highly Heterogeneous Petroleum Reservoirs using Fully Unstructured Grids

Recife
2022

Artur Castiel Reis de Souza

Conservative Multiscale Strategies for Multiphase Flow on Highly Heterogeneous Petroleum Reservoirs using Fully Unstructured Grids

Thesis submitted to the faculty of the Postgraduate Course in Civil Engineering of the Federal University of Pernambuco as part of the requirements necessary to obtain the Doctor's degree in Civil Engineering

Supervisor: Paulo Roberto Maciel Lyra, PhD

Co-supervisor: Darlan Karlo Elisiário de Carvalho, PhD

External Supervisor: Michael G. Edwards, PhD

Recife

2022

Catalogação na fonte
Bibliotecário Gabriel Luz, CRB-4 / 2222

S729c Souza, Artur Castiel Reis de.
Conservative multiscale strategies for multiphase flow on highly heterogeneous petroleum reservoirs using fully unstructured grids / Artur Castiel Reis de Souza. 2022.
135 f.; il.

Orientador: Prof. Dr. Paulo Roberto Maciel Lyra.
Orientador: Prof. Dr. Michael G. Edwards.
Coorientador: Prof. Dr. Darlan Karlo Elisiário de Carvalho.
Tese (Doutorado) – Universidade Federal de Pernambuco. CTG. Programa de Pós-Graduação em Engenharia Civil, Recife, 2022.
Inclui referências e apêndices.

1. Engenharia civil. 2. MsFV. 3. Volumes finitos. 4. Malhas não estruturadas. 5. AMS-U. 6. Simulação de reservatórios. I. Lyra, Paulo Roberto Maciel (Orientador). II. Carvalho, Darlan Karlo Elisiário de (Coorientador). III. Edwards, Michael G. (Coorientador). IV. Título.

UFPE

624 CDD (22.ed.) BCTG/2022-292

ARTUR CASTIEL REIS DE SOUZA

Conservative Multiscale Strategies for Multiphase Flow on Highly Heterogeneous Petroleum Reservoirs using Fully Unstructured Grids

Tese apresentada ao Programa de Pós-Graduação em Engenharia Civil da Universidade Federal de Pernambuco, Centro de Tecnologia e Geociências, como requisito para obtenção do título de Doutor em Engenharia Civil, Área de Concentração Simulação e Gerenciamento de Reservatórios de Petróleo.

Aprovada em: 18/07/2022

BANCA EXAMINADORA

_____
Prof. Dr. Paulo Roberto Maciel Lyra (Orientador)
Universidade Federal de Pernambuco

_____
Prof. Dr. Darlan Karlo Elisiário de Carvalho (Coorientador)
Universidade Federal de Pernambuco

_____
Prof. Dr. Michael G. Edwards (Orientador Externo)
Swansea University

_____
Prof. Dr. Ramiro Brito Willmersdorf (Examinador Interno)
Universidade Federal de Pernambuco

_____
Prof. Dr. Leonardo José do Nascimento Guimarães (Examinadora Interna)
Universidade Federal de Pernambuco

_____
Prof. Dr. José Roberto Pereira Rodrigues (Examinador Externo)
Petróleo Brasileiro

_____
Prof. Dr. Rafael Jesus de Moraes (Examinador Externo)
Petróleo Brasileiro

_____
Prof. Dr. Maicon Ribeiro Correa (Examinador Externo)
Universidade Estadual de Campinas

I dedicate this work to the people who made this challenging adventure possible, my family.

ACKNOWLEDGEMENTS

The doctorate is one of the highest titles awarded by universities to individuals who dedicate their lives to the pursuit of scientific knowledge. Although this title requires an insane amount of work and dedication, no one attains the doctorate on their own. It is important to understand that a PhD, by definition, is the result of the collective work of hundreds, perhaps thousands, of people who have contributed, directly or indirectly, to make it possible. Therefore, to truly acknowledge those who contributed to this research, I would need to include more than an acknowledgement in the prologue of this thesis. Even to name the groups and individuals who have been involved in the creation of this work is a Herculean task that I will humbly take upon myself.

First and foremost, I would like to thank Dr. Paulo Lyra and Dr. Darlan de Carvalho, my supervisors, for the opportunity. The countless hours, the many debates, their selfless dedication. I could easily get lost in enumerating all the moments and lessons that were imparted to me. I hope that I have learned them well. I would also like to express my great gratitude to my PhD supervisor in the UK, Dr. Michael Edwards, who welcomed me to Swansea University. Professor Edwards has been a source of inspiration guiding me through the unusual times that the pandemic has caused. I sincerely hope that this is the beginning of an everlasting partnership.

Second, I would like to express my gratitude and appreciation to my friends who have supported me since before this journey began. I would like to express my sincere gratitude to Dr. Lázara Castrillo and Dr. Jefferson Tavares, who encouraged me to pursue a career in science before I saw it as an option. I am writing this note today because they told me it was possible and fun. I would also like to thank Dr. Kiyohide Wada, and Dr. Yawei Xie, great friends that Swansea gave me. Finally, I would like to thank the friends I made at High-Performance Processing in Computational Mechanics (PADMEC). My special thanks go to Dr. Ramiro Willmersdorf, Dr. Fernando Contreras, José Cicero Santos, Túlio Moura, Ricardo Lira, Filipe Cumaru, and João Paulo Andrade. The quality of this work is due to our excellent teamwork. It is also important to thank the organisations that funded this research. I would like to thank the Science Support Foundation of the State of Pernambuco (FACEPE), the National Council for Scientific and Technological Development (CNPq), the Coordination for the Improvement of Higher Education Personnel (CAPES) and the Energi Simulation Foundation. It is also important to highlight and acknowledge the role of some very special people who have indirectly helped me along the way. I would like to thank my former teachers who gave me a taste of knowledge. I would also like to thank the staff of the graduate civil

engineering course at UFPE. They have my fullest appreciation.

Last but not least, I need to give due credit to the people who made this work possible, my family. It is hard for me to imagine a scenario where I could have done what I did without the support that my loving, caring family gave me. I believe any attempt to thank them would be an understatement that cannot adequately reflect what they have done. All I can do is to offer this degree in retribution to all their love. I thank my siblings Bruna and Rodrigo, my parents Neyla and Artur, my paternal grandparents (in memoriam), Fernando and Noemi, my maternal grandparents, Ney and Lea, and my beautiful wife Mirella. Thanks to you, I am who I am. This work is dedicated to you.

If I have seen further
it is by standing on the shoulders of giants.
(Sir Isaac Newton)

ABSTRACT

Simulation is fundamental to the management of subsurface oil reservoirs. The ability to predict the behaviour of multiphase flow in highly heterogeneous porous media allows to optimise recovery rates and maximize profits. Techniques such as history matching and optimisation make extensive use of simulations to better understand and predict the different scenarios and their respective impacts on production curves. However, recent advances in geological characterization have made it possible to integrate petrophysical data at a scale orders of magnitude higher than the feasible scale of standard petroleum reservoir simulators can handle. To deal with this discrepancy between scales, the family of approximate and conservative Multiscale Finite Volume (MsFV) methods was developed. These methods project the fine-scale system of equations onto a coarse space where it is solved and projected back. In this way, the high-resolution data is integrated into the simulator model, allowing fast and robust solutions at the price of a small loss of accuracy. Nonetheless, the MsFV family is not suitable for simulations on non-k-orthogonal grids. In this work, techniques for generalising methods of the finite volume and multiscale finite volume families have been investigated and developed in order to extend their applications to general unstructured grids. To this end, we have investigated the three main problems that prevent standard MSFV methods from being compatible with unstructured grids: 1) the lack of a consistent flux approximation for general grids, 2) the lack of a definition of multiscale units, and 3) the development of multiscale operators for unstructured grids. As a result, we developed the Algebraic Multiscale Solver for Unstructured Grids by proposing a new approach to create primal and dual coarse grids, developing a novel technique to avoid basis function leakage, and coupling the Algebraic Multiscale Solver (AMS) with a Multipoint Flux Approximation with a Diamond Stencil (MPFA-D). Another product of this work is the Flux Limited Splitting method, a novel repair technique that splits the flux of MPFA methods in terms of TPFA and Cross Diffusion Terms (CDT), where the letter is bounded by a relaxation parameter that is calculated nonlinearly to obtain a solution that satisfies the Discrete Maximum Principle (DMP).

Keywords: MsFV; finite Volume, unstructured grids, AMS-U; petroleum reservoir simulation.

RESUMO

A simulação é fundamental para o gerenciamento de reservatórios de petróleo subterrâneos. A capacidade de prever o comportamento do fluxo multifásico em meios porosos altamente heterogêneos permite otimizar as taxas de recuperação e maximizar os lucros. Técnicas como ajuste histórico e otimização fazem uso extensivo de simulações para melhor entender e prever os diferentes cenários e seus respectivos impactos nas curvas de produção. No entanto, avanços recentes na caracterização geológica tornaram possível integrar dados petrofísicos em uma escala de ordem de magnitude maior do que a escala suportada pelos simuladores de reservatórios de petróleo padrão.Para lidar com essa discrepância entre escalas, foi desenvolvida a família de métodos conservativos e aproximados Multiscale Finite Volume (MsFV). Esses métodos projetam o sistema de equações de uma escala de maior resolução no espaço de uma malha de menor resolução onde ele é então resolvido e projetado de volta. Desta forma, os dados de alta resolução são integrados ao modelo do simulador, permitindo soluções rápidas e robustas ao preço de uma pequena perda de precisão. No entanto, a família MsFV não é adequada para simulações em malhas não k-ortogonais. Neste trabalho investigamos e desenvolvemos técnicas para generalizar métodos das famílias de volumes finitos e de volumes finitos multiescala (MsFV) para malhas gerais não estruturadas. Para isso, investigamos os três principais problemas que impedem que os métodos padrão MSFV sejam compatíveis com grades não estruturadas: 1) a falta de uma aproximação consistente de fluxo para malhas não estruturadas em geral, 2) a falta de uma definição das entidades multiescala e 3) o desenvolvimento de operadores multiescala para malhas não estruturadas. Como resultado, desenvolvemos o Algebraic Multiscale Solver for Unstructured Grids, propondo uma nova abordagem para criar as malhas primais e duais, desenvolvendo uma nova técnica para evitar vazamento de função de base e acoplando o Algebraic Multiscale Solver (AMS) com uma aproximação de fluxo do tipo Multipoint Flux Approximation com estêncil Diamante (MPFA-D). Outro produto deste trabalho é o Flux Limited Splitting, uma nova técnica de reparo que divide a expressão da vazão de métodos MPFA linear em termos de TPFA e Cross Diffusion Terms (CDT), em que ela é limitada por um parâmetro de relaxação que é calculado de forma não linear para obter uma solução que satisfaça o Princípio do Máximo Discreto (DMP).

Palavras-chave: MsFV; volumes finitos, malhas não estruturadas; AMS-U; simulação de reservatórios.

LIST OF FIGURES

LIST OF FLOWCHARTS

LIST OF TABLES

LIST OF ABBREVIATIONS AND ACRONYMS

AMS	Algebraic Multiscale Solver
AMS-U	Algebraic Multiscale Solver for Unstructured Grids
BC	Boundary Conditions
CMP	Continuous Maximum Principle
CV	Control Volume
CVD	Control Volume Distributed
DMP	Discrete Maximum Principle
FLS	Flux Limited Splitting
FV	Finite Volume
IMPES	Implicit Pressure Explicit Saturation
LDMP	Local Discrete Maximum Principle
LHS	Left Hand Side
MPFA	Multi-Point Flux Approximation
MPFA-D	Multi-Point Flux Approximation with a Diamond Stencil
MsFV	Multiscale Finite Volume
MsRSB	Multiscale Restriction-Smoothed Basis
PDE	Partial Differential Equation
RHS	Right Hand Side
SEQ	Sequential Implicit
TPFA	Two-Point Flux Approximation

CONTENTS

1 MOTIVATION AND GENERAL CONSIDERATIONS

Simulations play a crucial role in the management of subsurface oil reservoirs. Simulators are used to predict complex fluid flow fields in highly heterogeneous porous media and to optimise production rates in accordance with economic requirements. Optimisation and history matching techniques make extensive use of simulations to better understand and predict different scenarios and their impact on production curves depending on the given flow conditions at injection and production wells. Recent advances in characterisation have made it possible to integrate petrophysical data at a scale orders of magnitude higher than standard petroleum reservoir simulators (ZHOU; TCHELEPI, 2008; LUNATI; JENNY, 2006; LUNATI; JENNY, 2008; LUNATI; TYAGI; LEE, 2011; MOYNER; LIE, 2015). Furthermore, the convoluted geometry and large heterogeneity in unconventional reservoirs add a new level of complexity to simulations, making them more computationally intensive. This severely limits the use of high-resolution geological models, which in turn limits the accuracy of the simulations (SOUZA et al., 2020).

To circumvent the computational constraints and take advantage of the high-resolution scale, the Multiscale Finite Volume (MsFV) method was developed (JENNY; LEE; TCHELEPI, 2003; JENNY; LEE; TCHELEPI, 2006; ZHOU; TCHELEPI, 2008). These schemes generate sets of basis functions that are used to project the high-resolution system of equations onto a low-resolution space. The new system is solved and later projected back onto the high-resolution grid to compute a reasonably accurate conservative solution (JENNY; LEE; TCHELEPI, 2003; JENNY; LEE; TCHELEPI, 2006; SOUZA et al., 2020). The idea behind this and other related multiscale methods is that solving a set of localised high-resolution systems together with a global problem at the coarse scale (LUNATI; TYAGI; LEE, 2011) is computationally less expensive than direct simulation at the high-resolution scale.

The success of the MsFV method in representing fluid flow in homogeneous and mildly heterogeneous porous media has led to the development of new studies aimed at improving various aspects of the original method. Some authors focused on the construction of multiscale well models (WOLFSTEINER; LEE; TCHELEPI, 2006; JENNY; LUNATI, 2009); the study of techniques to incorporate more complex physical conditions into the reservoir model (LUNATI; JENNY, 2008; LUNATI; JENNY, 2006; LEE; WOLFSTEINER; TCHELEPI, 2008; HAJIBEYGI; JENNY, 2009; HAJIBEYGI; TCHELEPI, 2014), and the improvement of the boundary conditions of the localised problems (WANG; HAJIBEYGI; TCHELEPI, 2015). Moreover, inspired by multigrid methods, Zhou & Tchelepi (2008) developed a matrix representation of the prolongation and

restriction steps devising what has become the standard notation of the MsFV. In this method, the multiscale procedures are written as a series of simple matrix operations using the newly developed operators. Despite all these efforts, the standard Multiscale Finite Volume family still struggles to simulate highly heterogeneous and anisotropic reservoirs (HAJIBEYGI et al., 2008). To deal with this issue, iterative methods have been developed to ensure that the multiscale solution converges to the fine-scale solution within a certain tolerance (HAJIBEYGI et al., 2008; HAJIBEYGI; JENNY, 2011a; LUNATI; TYAGI; LEE, 2011).

The Algebraic Multiscale Solver (AMS) (ZHOU; TCHELEPI, 2011; WANG; HAJIBEYGI; TCHELEPI, 2014) generalised the classic Multiscale Finite Volume method and became its modern successor. In this method, a simple matrix notation allows the computation of the multiscale prolongation operators and a set of correction functions as a set of straightforward algebraic operations performed on the fine-scale discrete system. Combined with an iterative multiscale stage, this method has been shown to be efficient and robust, with results comparable to multigrid methods (WANG; HAJIBEYGI; TCHELEPI, 2014). Several authors have successfully modified the AMS to incorporate new features such as embedded fracture models (ŢENE; KOBAISI; HAJIBEYGI, 2016), more complex physics (ŢENE; WANG; HAJIBEYGI, 2015), multiscale multilevel simulations (CUSINI et al., 2018; HAJIBEYGI et al., 2020) and to provide a general framework that allows the integration of new models in a unified way (CORTINOVIS; JENNY, 2017).

Nevertheless,the methods referred above are not generally applicable on unstructured grids. There are three reasons for this limitation: the standard Two-Point Flux Approximation (TPFA) used in these methods is consistent only consistent for k-orthogonal grids, i.e. when the faces Γ of the volumes are aligned with the principal directions of the permeability tensor (AAVATSMARK et al., 1998) , the difficulties in generalising the multiscale geometric entities such as the primal and dual coarse grids, and a proper definition of the multiscale operators for this type of grid (SOUZA et al., 2020). The work of Moyner & Lie (2013) addressed this second issue and developed a generalisation of the MsFV for working with unstructured coarse grids. Moyner & Lie (2015) went further and redesigned the multiscale geometric entities and the multiscale operators and created the Multiscale Restriction-Smoothed Basis (MsRSB), which is only consistent on unstructured coarse grids. Bosma et al. (2017) have worked on the extension of the multiscale entities, and on creating a prolongation operator for unstructured grids by rescaling the MsFV basis functions. Mehrdoost (2019) and Mehrdoost (2021) have studied techniques to create adaptive primal and dual unstructured coarse grids.

Despite these significant contributions, these methods lack a generally con-

sistent flux approximation for anisotropic problems on unstructured grids. As for the flow equation approximation, great efforts have been made to develop consistent flux approximations, called Control Volume Distributed Multipoint Flux Approximations (CVD-MPFA), which overcome the limitations of TPFA (CRUMPTON; SHAW; WARE, 1995; AAVATSMARK et al., 1998; EDWARDS; ROGERS, 1998; CARVALHO; WILLMERSDORF; LYRA, 2007a; EDWARDS; ZHENG, 2008; CHEN et al., 2008; EDWARDS; ZHENG, 2010; GAO; WU, 2010; FRIIS; EDWARDS, 2011; CONTRERAS et al., 2016; CONTRERAS; LYRA; CARVALHO, 2019).

Monotonicity is an important property sought by authors devising numerical schemes. In the context of highly anisotropic petroleum reservoirs, the loss of monotonicity may lead to solutions that violate entropy constraints (YUAN; SHENG, 2008), causing oil to flow from regions with low pressure towards higher pressures. In media with high anisotropy ratios and permeability variations, monotonicity loss can also lead to the occurrence of negative absolute pressures, for instance. However, monotonicity is not sufficient to ensure that a discrete solution does not have spurious oscillations. In contrast, a method with a local discrete Maximum Principle (DMP) yields a discrete solution that is free of this non-physical oscillations, and if a method has an M-matrix, then this ensures that the solution has a local DMP (EDWARDS; ZHENG, 2010). The standard TPFA method applied to the pressure equation has an M-matrix and therefore the resulting discrete solutions are free of spurious oscillations. However, the method is inconsistent if the grid is not k-orthogonal, which occurs when full tensor fields are present.

We note that both the more recent CVD-MPFA methods with full pressure support (FPS) e.g. (EDWARDS; ZHENG, 2010; GAO; WU, 2010) and the earlier methods with triangular pressure support (TPS) CVD-MPFA have a conditional M-matrix and local DMP. For some test cases with strongly anisotropic full tensors, both CVD-MPFA formulations (FPS and TPS) have no local DMP, yet only the earlier TPS methods induce severe spurious oscillations. This is because TPS has a limited quadrature range, shown to be decoupled when strong full-tensors are present.

This behaviour is shown to be due to decoupling of the domain. (EDWARDS; ZHENG, 2008; EDWARDS; ZHENG, 2010) analyse and explain this phenomenon. It is shown that the FPS formulations do not suffer from decoupling and can compute solutions free of severe unphysical oscillations at the lattice level, despite the lack of a formal local DMP in such cases.

The first work coupling MsFV with CVD-MPFA to create a consistent multiscale method applicable to non k-orthogonal and unstructured grids is presented in Parramore et al. (2016). However, this method requires that a MsFV fine-scale grid to be defined by refining an unstructured coarse grid. The work of Souza et al. (2020)

coupled the Multipoint Flux Approximation using a Diamond Stencil (MPFA-D) with the MsRSB, creating a consistent framework for Multiscale Control Volume (MsCV) on unstructured grids. Recently, Bosma et al. (2020) developed a filtering strategy to improve the MsRSB method by enforcing M-matrix properties.

1.1 Research Objectives

In this context, the general objective of this work is to investigate and develop conservative multiscale schemes for 2-D, extensible to 3-D, simulation of multiphase flows in heterogeneous and anisotropic porous media using non-k-orthogonal meshes.

Specific Objectives

1. To investigate and develop algorithms for the creation of multiscale geometric entities in 2-D, extensible to 3-D.
2. To implement linear and non-linear flux approximation schemes for the discretisation of the pressure equation.
3. To investigate and develop a multiscale scheme for the simulation of multi-phase flows in highly heterogeneous and anisotropic petroleum reservoirs consistent in general unstructured grids, at all scales.

1.2 Articles published in journals, conferences and congresses

As a direct result of our research, we have written the following articles that have been published in international journals, congresses and conferences:

Articles published in peer reviewed scientific journals

- SOUZA, A. C. R. de; BARBOSA, L. M. C.; CONTRERAS, F. R. L.; LYRA, P. R. M.; CARVALHO, D. K. E. de. A Multiscale Control Volume framework using the Multiscale Restriction Smooth Basis and a non-orthodox Multi-Point Flux Approximation for the simulation of two-phase flows on truly unstructured grids. *Journal of Petroleum Science and Engineering*, Elsevier BV, v. 188, p. 106851, may 2020. Available on: <https://doi.org/10.1016/j.petrol.2019.106851>.
- SOUZA, A. C. R. de; CARVALHO, D. K. E. de; SANTOS, J. C. A. dos; WILLMERSDORF, R. B.; LYRA, P. R. M.; EDWARDS, M. G. An algebraic multiscale solver for the simulation of two-phase flow in heterogeneous and anisotropic porous media using general unstructured grids (AMS-U). *Applied Mathematical Modelling*,

Elsevier BV, v. 103, p. 792–823, mar 2022. Available on: <https://doi.org/10.1016/j.apm.2021.11.017>.

- SANTOS, J. C. A. dos; LYRA, P. R. M.; ANDRADE, J. P. R. de; SOUZA, A. C. R. de; FILHO, R. J. M. de L.; CARVALHO, D. K. E. de. An Algebraic Dynamic Multilevel and Multiscale Method with Non-Uniform Mesh Resolution and Adaptive Algebraic Multiscale Solver operator for the simulation of two-phase flows in highly heterogeneous petroleum reservoirs. *Journal of Computational Physics*, p. 111174, 2022.

Articles published in congresses and conferences

- SOUZA, A. C. R. de; CAVALCANTE de T. M.; CARVALHO, D. K. E. de; EDWARDS, M. G.; LYRA, P. R. M. Numerical simulation of the diffusion equation via a Nonlinear Flux Splitting technique with the Multi-Point Flux Approximation method with a Diamond stencil satisfying the Discrete Maximum Principle using 2-D unstructured meshes. *Proceedings of the 26th International Congress of Mechanical Engineering*, 2021.
- SILVA, R. N. T.; MATOS, G. M.; SOUZA, A. C. R. de; FILHO, R. J. M. L.; CARVALHO, D. K. E. de; LYRA, P. R. M. Some results on the accuracy of a classical upscaling technique using an Intuitive Multilevel Preprocessor for Smart Simulation. *Proceedings of Ibero-Latin American Congress on Computational Methods in Engineering (CILAMCE 2020)*, 2020.
- JUVITO, L.; RAMIREZ, G. G.; SOUZA, A. C. R. de; CARVALHO, D. K. E. de; LYRA, P. R. M. An iterative MsCV method coupled to the high-resolution CPR approach via different solution smoothers for the simulation of oil-water flows in 2-D petroleum reservoirs on unstructured grids. *Proceedings of Ibero-Latin American Congress on Computational Methods in Engineering (CILAMCE 2020)*, 2020.
- SANTOS, J. C. A.; ANDRADE, J. P. R.; SOUZA, A. C. R.; FILHO, R. J. M. L.; CARVALHO, D. K. E.; LYRA, P. R. M. An Adaptive Algebraic Dynamic Multilevel (A-ADM) and Multiscale Method with Enriched Basis Functions for the simulation of two-phase flows in highly heterogeneous petroleum reservoirs. *Proceedings of Ibero-Latin American Congress on Computational Methods in Engineering (CILAMCE 2020)*, 2020.

1.3 Thesis Organisation

This thesis has been divided into 5 different chapters dealing with different topics. The first chapter consists of the introduction, which gives a brief overview of the topics covered in this thesis. The second chapter deals with the mathematical model describing the physical phenomena governing the single-phase and two-phase flow in porous media. The third chapter is a description of the fine-scale flux approximation and includes a subsection on the MultiPoint Flux Approximation with a Diamond Stencil and where we introduce the Flux Limited Splitting technique to recover a solution that complies with DMP. In the fourth chapter we give a brief overview of multiscale finite volume methods, including a section on the standard Multiscale Finite Volume and Algebraic Multiscale Solver methods, and introduce the Algebraic Multiscale Solver for Unstructured Grids. The fifth chapter of this thesis is devoted to the results, where we test our formulations on some benchmark cases. Finally, the last chapter consists of the conclusions and suggestions for future work. Moreover, we dedicated the appendix of the thesis to the background grid strategy and the preprocessing algorithms used to create the multiscale entities for unstructured grids.

2 GOVERNING EQUATIONS

The main idea of this chapter is to briefly discuss the mathematical model that governs the two-phase flow of water-oil in porous media. Since this topic has already been the subject of extensive studies by our research group and other authors (SOUZA, 2018; CARVALHO, 2005; SOUZA, 2015; CONTRERAS, 2017; AZIZ; SETTARI, 1979), the focus here is solely on explaining the models and the partial differential equation (PDE) describing the model. To find the following equations, we manipulate the mass conservation law along with Darcy's law for fluid flow in porous media fully saturated porous media assuming an immiscible, incompressible, isothermal Newtonian fluid through a fully saturated medium with negligible compressibility. Furthermore, thermal capillarity effects and chemical reactions between phases are not taken into account. Finally, we neglect dispersion and adsorption effects. The resulting mathematical model describes a two-phase flow, water-oil, using two different PDE, an elliptic (pressure) and a hyperbolic (saturation) equation.

2.1 Mass Conservation Equation and Darcy's Law

The mass conservation law on porous media for two-phase flow, water (w) - oil (o), defined over a physical domain $\Omega \times [0,t]$ is given by (CHEN; HUAN; MA, 2006):

$$\frac{\partial(\phi \rho_i S_i)}{\partial t} = -\nabla \cdot (\rho_i \vec{v_i}) + q_i \quad \text{in} \quad \Omega \times [0,t] \quad \text{where} \quad i = \text{water (w), oil (o)} \tag{2.1}$$

where ϕ represents the porosity of the medium, t the time, q_i the source/sink term of the phase that in this context may represent the injection and production wells, S_i is the phase i saturation, $\vec{v_i}$ phase velocity and ρ_i the density of the phase. The assumption of a fully saturated media gives the following closing equation:

$$S_o + S_w = 1 \tag{2.2}$$

Darcy's law, originally discovered by Henry Darcy, is a volume averaging experimental equation that later turned out to be an approximation to the Navier-Stokes equation, (EWING, 1983)using the smallest possible scale but large enough to capture the heterogeneity of a porous medium as given by:

$$\vec{v_i} = -\lambda_i \underline{K}(\vec{\nabla} p_i - \rho_i \vec{g}) \quad \text{with} \quad \lambda_i = k_{ri}/\mu_i \tag{2.3}$$

where λ_i , k_{ri}, μ_i, and p_i represent respectively mobility , relative permeability, viscosity, and pressure of the phase i, and where $\vec{g}$ represents the gravity.

The two-dimensional ($\mathbb{R}^2$) Cartesian absolute permeability tensor $\underline{K}$ is defined as:

$$\underline{K}(\vec{x}) = \begin{bmatrix} k_{xx} & k_{xy} \\ k_{yx} & k_{yy} \end{bmatrix} \quad \forall \vec{x} \in \mathbb{R}^2 \quad \text{where} \quad \vec{x} = (x, y) \tag{2.4}$$

The absolute permeability $\underline{K}$ is a rock property that measures the capacity of a medium to allow flow. The relative permeability k_{ri}, in turn, is a dimensionless measure of the effective permeability of a given phase.

It is also necessary to have an equation that describes the influence of one phase flow over the other phases. In this work, we employ the Brooks and Corey model, an experimental constitutive equation (HELMIG, 1997) defined as:

$$k_{rw} = \left(\frac{S_w - S_{wi}}{1 - S_{wi} - S_{or}} \right)^{n_w} \quad \text{and} \quad k_{ro} = \left(\frac{1 - S_w - S_{or}}{1 - S_{wi} - S_{or}} \right)^{n_o} \tag{2.5}$$

where S_i denotes the fraction of the pore volume occupied by a phase $i = o, w$, S_{wi} and S_{or} represents the residual saturation of the water and oil phases, and n_w and n_o assume different values (CHEN; HUAN; MA, 2006; AZIZ; SETTARI, 1979).

2.2 Elliptic Pressure Equation

By combining and manipulating equations (2.1) to (2.3), we derive the pressure equation (HELMIG, 1997; CARVALHO, 2005; CHEN; HUAN; MA, 2006; EWING, 1983, 1983) expressed as it follows:

$$\vec{\nabla} \cdot \vec{v} = Q \quad \text{with} \quad \vec{v} = -\lambda \underline{K} (\vec{\nabla} p - \rho_{\text{avg}} \vec{g}) \quad \text{in} \quad \Omega \tag{2.6}$$

where $\vec{v} = \vec{v}_w + \vec{v}_o$ denotes the total velocity of the fluid, ∇p represents the pressure gradient and $Q = Q_w + Q_o$ is the sum of the volumetric source and sink terms of each phase divided by the respective density, $Q_i = q_i / \rho_i$. We define the average density ρ_{avg} as mobility weighted average of the phases density (HURTADO, 2011) as:

$$\rho_{\text{avg}} = \frac{\lambda_o \rho_o + \lambda_w \rho_w}{\lambda} \quad \text{with} \quad \lambda = \lambda_o + \lambda_w \tag{2.7}$$

where λ_o , λ_i, λ represent respectively the mobility of the oil phase, the mobility of the water phase and the total mobility.

By neglecting the gravity term on the Darcy's velocity equation (2.6), we find a simpler form for the total velocity:

$$\vec{v} = -\lambda \underline{K} \vec{\nabla} p \tag{2.8}$$

By inserting this simplified velocity (2.8) inside (2.6), we obtain the global pressure equation for two-phase flow:

$$-\vec{\nabla} \cdot (\lambda \underline{K} \vec{\nabla} p) = Q \tag{2.9}$$

For single-phase flow, if we set $\lambda = 1$, we have:

$$-\vec{\nabla} \cdot (\underline{K}\vec{\nabla}p) = Q \tag{2.10}$$

2.3 Hyperbolic Saturation Equation

Another product of the manipulation of the mass conservation equation (2.1) is the saturation equation, a hyperbolic non-linear PDE that describes how one of the phases is transported across the porous medium. We define the resulting equations for water phase as:

$$\phi \frac{\partial S_w}{\partial t} = -\vec{\nabla} \cdot \vec{F}(S_w) + Q_w \quad \text{for} \quad \Omega \times [0, t] \tag{2.11}$$

where $\vec{F}(S_w)$ is defined as:

$$\vec{F}(S_w) = f_w(S_w)\vec{v} \quad \text{with} \quad f_w = \lambda_w/\lambda \tag{2.12}$$

The fractional flux $f_w(S_w)$ is an expression that describes the fraction of water transported with the total flow. Since the fractional flux depends on the saturation, it represents a non-linear term on the equation. Moreover, it is worth noting that the mobilities are a function of the saturation field, while Darcy's velocity is a function of the pressure field. Therefore, these terms couple the elliptic pressure and hyperbolic saturation equation.

2.4 Initial and Boundary Conditions

The mathematical model described by equations (2.6) and (2.11) requires a combination of initial and boundary conditions (BC). Apart from the classical Dirichlet and Neumann Boundary conditions, we define a special subset of these BC to represent the interaction between the wells and the porous medium (See Figure 1). Thus, we define the usual boundary conditions as:

Figure 1 – BC of a physical domain Ω: Dirichlet BC $\partial\Omega_D$, Neumann BC $\partial\Omega_N$, production $\partial\Omega_P$ and injection $\partial\Omega_I$ wells BC.

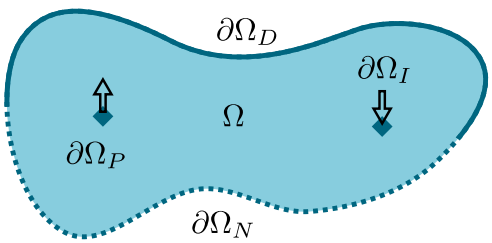

Source: Author.

$$\begin{aligned} p(\vec{x},t) &= g_D \quad \text{on} \quad \partial\Omega_D \times [0,t] \\ \vec{v}\cdot\vec{n} &= g_N \quad \text{on} \quad \partial\Omega_N \times [0,t] \\ p(\vec{x},t) &= Q_{\text{inj}} \quad \text{on} \quad \partial\Omega_I \times [0,t] \\ \vec{v}\cdot\vec{n} &= P_{\text{prod}} \quad \text{on} \quad \partial\Omega_P \times [0,t] \end{aligned} \tag{2.13}$$

where g_D and g_N stand for the prescribed pressure and prescribed flux; Q_{inj}, P_{prod} the prescribed pressure and flux,respectively, defined at the injection and production wells, and where $\vec{n}$ is unit normal vector.

We define the boundary conditions $\partial\Omega$ of the domain Ω as a disjoint set of the different conditions presented on the previous equation:

$$\partial\Omega = \partial\Omega_D \cup \partial\Omega_N \cup \partial\Omega_I \cup \partial\Omega_P \tag{2.14}$$

Finally, the boundary and initial conditions of the saturation equation are given by:

$$\begin{aligned} S_w(\vec{x},t) &= \bar{S}_I \quad \text{on} \quad \partial\Omega_I \times [0,t] \\ S_w(\vec{x},0) &= \bar{S}_w^o \quad \text{on} \quad \Omega \end{aligned} \tag{2.15}$$

where $\bar{S}_w^o$ is the initial saturation field, and $\bar{S}_I$ the water saturation of the injected fluid.

2.5 Continuous Maximum Principle

Let u be the solution of the second order diffusion equation subjected to Dirichlet or a combination of boundary conditions, such as the one found defined for equations (2.6):

$$\begin{cases} -\vec{\nabla}\cdot(\underline{D}\vec{\nabla}u) = b \quad \text{in} \quad \Omega \\ \qquad\qquad u = g_D \quad \text{on} \quad \partial\Omega \end{cases} \tag{2.16}$$

where $\underline{D}$ is the symmetric and uniformly positive diffusive tensor, and b a representation of the source and sink terms.

Theorem 2.5.1. *(KUZMIN; SHASHKOV; SVYATSKIY, 2009) The solution u attains its maxima or (minima) on the boundary of $\partial\Omega$ if b is non-positive (non-negative) in Ω.*

$$\begin{aligned} b \leq 0 &\longrightarrow \max_{x\in\Omega} u(x) = \max_{x\in\partial\Omega} g_D(x) \\ b \geq 0 &\longrightarrow \min_{x\in\Omega} u(x) = \min_{x\in\partial\Omega} g_D(x) \end{aligned} \tag{2.17}$$

Theorem 2.5.1 is often referred as the Maximum Principle or Continuous Maximum Principle (CMP) no matter the sign of b.

Corollary 2.5.1.1. *If $b = 0$, then the solution u is bounded by the Dirichlet boundary conditions.*

$$b = 0 \longrightarrow \min_{x\in\partial\Omega} g_D(x) \leq u(x) \leq \max_{x\in\partial\Omega} g_D(x) \tag{2.18}$$

Corollary 2.5.1.2. *The solution u preservers the sign of the boundary values, if b and g_D are non-positive (non-negative) in Ω.*

$$\begin{aligned} b \leq 0,\ g_D \leq 0 \longrightarrow u \leq 0 \quad in \quad \Omega \\ b \geq 0,\ g_D \geq 0 \longrightarrow u \geq 0 \quad in \quad \Omega \end{aligned} \tag{2.19}$$

The above corollary is often referred as the positive or negative preservation property. Please, check (KUZMIN; SHASHKOV; SVYATSKIY, 2009) for more details and the proof of Theorem 2.5.1.

3 FINITE VOLUME FORMULATION

The set of partial derivative equations described in the previous chapter govern the behaviour of fluid flow in the rock reservoir. As with most physical phenomena, the complexity of these equations either admits an analytical solution with some simplifying conditions, or they do not have known solutions at all. In this way, numerical schemes become a viable alternative as they allow us to obtain approximate solutions within a certain desired tolerance. Therefore, standard petroleum reservoir simulators are a key tool for the management of subsurface oil reservoirs. Techniques such as history matching, uncertainty quantification-propagation and optimization make extensive use of simulations.

At the heart of these simulators is the Finite Volume (FV), a locally conservative flux-continuous family of methods whose best-known member is the Two-Point Flux Approximation (TPFA) scheme. The main advantages that make TPFA so appealing over other flux approximation methods are its efficiency, simplicity, and the guarantee of solutions that are free of spurious oscillations because this scheme satisfies the Discrete Maximum Principle (DMP). This is the case because methods capable of generating an M-matrix, such as the TPFA, are guaranteed to yield solutions with local DMP (EDWARDS; ZHENG, 2010). However, this scheme fail to produce consistent solution for non-k-orthogonal grids and for media with full permeability tensors.

These difficulties were first overcome when two groups of authors (EDWARDS; ROGERS, 1998; AAVATSMARK et al., 1998) , separately, generalised the work of Crumpton, Shaw & Ware (1995) and created the modern Control Volume Distributed (CVD) family, also known as MultiPoint Flux Approximation (MPFA), to work on general unstructured grids. With the success of this new branch of the family of linear finite volume methods, several authors have dedicated to improving these classical CVD-MPFA formulations (EDWARDS; ZHENG, 2008; CHEN et al., 2008; GAO; WU, 2010; CONTRERAS et al., 2016; CONTRERAS; LYRA; CARVALHO, 2019). Nevertheless, any linear scheme that is more than first-order accurate may lead to local extrema according to Godunov's theorem, i.e., these methods cannot satisfy the DMP. In the subsurface petroleum reservoir simulation context, the spurious oscillations caused by the inability to comply the DMP may lead to the appearance of virtual gas pockets when the pressure drops below the bubble point and oil to flow from low to high pressure zones (QUEIROZ et al., 2013). It is worth noting that modern CVD-MPFA schemes with full pressure support (FPS) e.g. (EDWARDS; ZHENG, 2010; GAO; WU, 2010) and earlier triangular pressure support (TPS) have a conditional M-Matrix and thus a local DMP. Ergo, media with strong anisotropic full tensors with abrupt permeability variations

can cause these methods to lose the DMP. As a result for some test cases with strong anisotropic full tensors, both formulations of CVD-MPFA (FPS and TPS) have no local DMP, yet only the earlier TPS methods induce severe spurious oscillations for most of the cases.

In this chapter, we present the schemes of cell-centred finite volume employed on this work to approximate the solution of aforementioned PDEs.

3.1 Cell Centred Finite Volume Methods for the Pressure Equation

Two important features distinguish the cell-centred family of Finite Volume methods. The first is the partitioning of the physical domain into smaller volumes with an unknown associated with CVs of that grid, while the second is the integral or conservative form of the equations. (SHENG; YUAN, 2015; WU; GAO, 2014; CONTRERAS, 2017). Before moving on to the definitions of the flux approximation, it is important to formally define some terms that will be used extensively in this work.

Mesh or Grid (Ω^f or Ω): The mesh is a discretization of the physical domain Ω. See Figure 2. For the sake of simplicity Ω and $\partial\Omega$ is also used to denote computational domain, and its boundaries.

Volume (Ω_k): The computational domain is subdivided in a set of $\{\Omega_k\}_{k=1}^{n_v}$ of n_v volumes or control volumes.

Face or Surface (Γ_j): The set of non overlapping faces is defined such that $\{\Gamma_j\}_{j=1}^{n_f} = \partial\Omega_i \cap \partial\Omega_j \ \forall\Omega_i, \Omega_j \in \Omega$ with $i \neq j$ and $\Gamma_j \neq \emptyset$.

Volume Boundaries ($\partial\Omega_k$): The boundaries of a volume Ω_k is a set defined as $\partial\Omega_k = \{\Gamma_j \in \Omega_k\} \ \forall\Omega_i, \Omega_j \in \Omega$ with $i \neq j$ and $\Gamma_i \neq \emptyset$.

Figure 2 – Representation of a physical domain and its discretization.

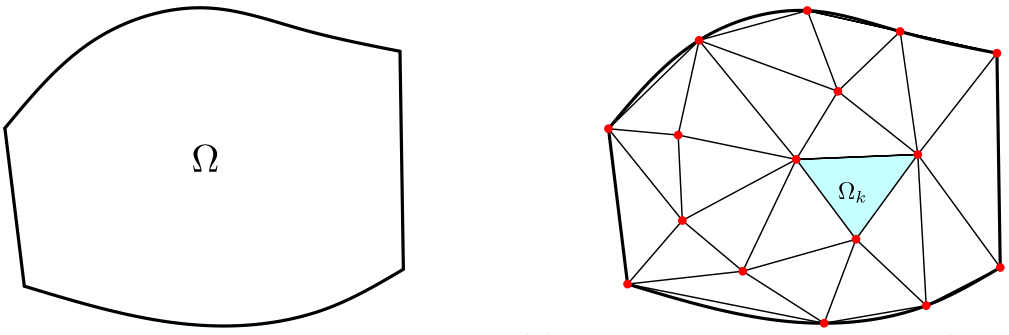

(a) Physical domain Ω.

(b) General Control Volume Ω_k (light blue) in discrete representation of th Ω .

Source: Author.

Let us start by integrating equation (2.6) over the domain Ω. This leaves us with:

$$\int_{\Omega} \vec{\nabla} \cdot \vec{v} dV = \int_{\Omega} Q dV \tag{3.1}$$

By definition, the domain Ω is discretized in n_v control volumes. This allow us to write equation (3.1) as:

$$\sum^{n_v} \int_{\Omega_k} \vec{\nabla} \cdot \vec{v} dV = \sum^{n_v} \int_{\Omega_k} Q dV \tag{3.2}$$

Therefore, the conservation form also holds for a single general control volume Ω_k :

$$\int_{\Omega_k} \vec{\nabla} \cdot \vec{v} dV = \int_{\Omega_k} Q dV \tag{3.3}$$

Note that equations (3.2) and (3.3) state that by definition Cell Centred Finite Volume methods are, respectively, globally and locally conservative. If we apply the Divergence Theorem to the LHS of equation (3.3), we obtain:

$$\int_{\partial\Omega_k} \vec{v} \cdot \vec{n} dA = \int_{\Omega_k} Q dV \tag{3.4}$$

If we apply the Mean Value Theorem to the LHS and RHS of equation (3.4), we obtain:

$$\int_{\partial\Omega_k} \vec{v} \cdot \vec{n} dA = \sum_{\Gamma_j \in \partial\Omega_k} (\vec{v} \cdot \vec{N})_{\Gamma_k} \tag{3.5}$$

where $\vec{v}_{\Gamma_k}$ stands for the mean velocity approximated on an arbitrary face Γ_k and the respective $\vec{N}_{\Gamma_k}$ the normal area vector in $\partial\Omega_k$, and:

$$\int_{\Omega_k} Q dV = \bar{Q}_k \Omega_k \tag{3.6}$$

where $\bar{Q}_k$ represent the mean value of the source/sink term.

By substituting equations (3.5) and (3.6), we rewrite equation (3.4) to formaly define the concept of mass conservation.

Definition 3.1.1. A numerical scheme is conservative if:

$$\sum_{\Gamma_j \in \partial\Omega_k} (\vec{v} \cdot \vec{N})_{\Gamma_j} = \hat{Q}_k \Omega_k \quad \forall \Omega_k \in \Omega \tag{3.7}$$

where the discrete Darcy's flux calculated for the control volumes to the left L and to the right R of Γ_j obey the following relation:

$$(\vec{v} \cdot \vec{N})^L_{\Gamma_j} + (\vec{v} \cdot \vec{N})^R_{\Gamma_j} = 0 \quad \forall \Gamma_j \in \Gamma \tag{3.8}$$

Note that, since the computational domain is discretized using a set of convex polygons equation (3.7) is an exact form of equation (3.4).

3.1.1 Mobility Approximation

The approximation of the relative permeability k_{rw} in equation (2.5) relies on the saturations, that in a cell centred finite volume scheme are calculated on the volumes of the discrete domain. Thus, the relative permeability k_{rw} and the mobility λ are also computed on the control volumes. However, both TPFA and MPFA-D flux expressions require the mobility to be projected on an arbitrary face Γ_j. Friis & Evje (2012) suggests the follow approximation to compute the face mobility λ_{Γ_j}.

$$\lambda_{\Gamma_j} = \frac{\lambda_I + \lambda_J}{2} \tag{3.9}$$

where the nodal mobilities λ_I and λ_J are approximated by the weighted average of the mobilities around a given node:

$$\lambda_i = \frac{\sum_{k=1}^{n_i} \lambda_k \Omega_k}{\sum_{k=1}^{n_i} \Omega_k} \tag{3.10}$$

where $i = I, J$ and n_i is number of control volumes around node i.

3.1.2 Matrix form of the Pressure Equation

Once a proper discrete flux approximation is defined, we can use equation (3.7) to assemble a linear system of equations that represents the discrete form of the mass balance equation, as it follows:

$$M_i p_i = Q_i \tag{3.11}$$

where M_i denotes the transmissiblity matrix, p_i the pressure vector, Q_i the source and sink term vector, and where the subscript i represents the flux approximation scheme used such i = TPFA, MPFA-D, etc.

3.1.3 Linear Two-Point Flux Approximation

The Two-Point Flux Approximation on its linear form is based on two hypotheses. The first is that fluxes across the faces are unique by definition. The second is that the fluxes in each control volume are piecewise linear. Let us consider a section of a k-orthogonal two-dimensional mesh as shown in Figure 3. Assuming that a control volume Ω_k is subjected to a pressure gradient along the x and y-axes, we can calculate the fluxes at its boundaries $\partial\Omega_k$ with no loss of generality. The flux across a face Γ_j shared by two adjacent control volumes on the left L and on the right R, with corresponding

Figure 3 – Geometric entities used to derive the TPFA across the boundaries $\partial\Omega_j$ (blue) of a an arbitrary control volume Ω_k (light blue) in a 2-D domain.

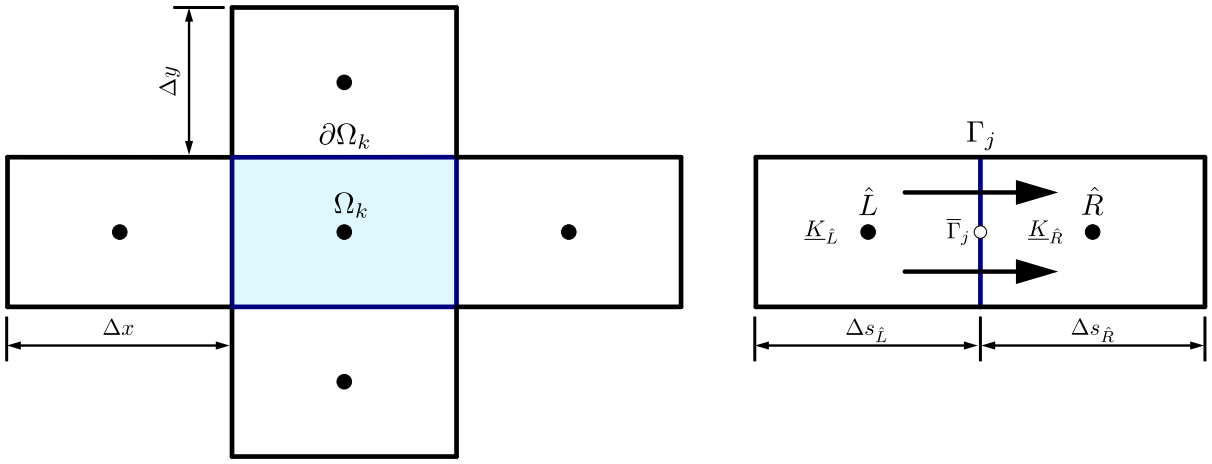

Source: Author

centroids represented by $\hat{L}$, and $\hat{R}$ is calculated using an auxiliary point, the centre of the face $\overline{\Gamma}_j$.

We can write the Darcy's flow expression, i.e., Darcy's velocity multiplied by the cross-sectional area, from the centre of left control volume $\hat{L}$ to centre of the shared face $\overline{\Gamma}_j$, and an expression from the centre of the shared face $\overline{\Gamma}_j$ to the centre of right control volume $\hat{R}$:

$$
\begin{aligned}
(\vec{v}\cdot\vec{N})^{L}_{\Gamma_j} &= -\lambda_{\Gamma_j} K_{L_{ss}} |\Gamma_j| \left(\frac{p_{\overline{\Gamma}_j} - p_{\hat{L}}}{\frac{\Delta s_{\hat{L}}}{2}} \right) \\
(\vec{v}\cdot\vec{N})^{R}_{\Gamma_j} &= -\lambda_{\Gamma_j} K_{R_{ss}} |\Gamma_j| \left(\frac{p_{\hat{L}} - p_{\overline{\Gamma}_j}}{\frac{\Delta s_{\hat{R}}}{2}} \right)
\end{aligned}
\tag{3.12}
$$

where p is the pressure, $|\Gamma_j|$ the cross-sectional area, $s = x$ or y depending on the orientation of the analysed face Γ_j, $K_{i_{ss}}$ represents the component of the permeability tensor $i = L, R$ of the left and right volumes aligned with the principal direction s, and Δs represents the length of the volume with respect to s.

The definition of continuity across the face Γ_j gives us the following equation:

$$
(\vec{v}\cdot\vec{N})^{L}_{\Gamma_j} + (\vec{v}\cdot\vec{N})^{R}_{\Gamma_j} = 0 \tag{3.13}
$$

By replacing equation (3.12) in (3.13), we obtain an expression for the pressure calculated on the centre of the shared face $p_{\overline{\Gamma}_j}$.

$$
p_{\overline{\Gamma}_j} = \frac{\frac{p_{\hat{L}} K_{L_{ss}}}{\Delta s_{\hat{L}}} + \frac{p_{\hat{R}} K_{R_{ss}}}{\Delta s_{\hat{R}}}}{\frac{K_{L_{ss}}}{\Delta s_{\hat{L}}} + \frac{K_{R_{ss}}}{\Delta s_{\hat{R}}}} \tag{3.14}
$$

We can finally define a unique flux expression by replacing equation (3.14) in either one of the equations (3.12).

$$(\vec{v}\cdot\vec{N})_{\Gamma_j} = -\frac{2\lambda_{\Gamma_j}K_{L_{ss}}K_{R_{ss}}}{K_{L_{ss}}\Delta s_{\hat{R}} + K_{R_{ss}}\Delta s_{\hat{L}}}|\Gamma_j|(p_{\hat{R}} - p_{\hat{L}}) \tag{3.15}$$

The Two-Point Flux Approximation scheme was named because the discrete flux expression in equation (3.12) relies exclusively on information of the two adjacent volumes sharing the face Γ_j. It should also be emphasised that this approximation is only consistent for k-orthogonal grids. This happens because the tangential components of the permeability tensor are neglected. Thus, if $\underline{K}$ is not aligned with the main axis, information is lost on the process. This may lead to first order errors $O(1)$ that do not disappear when the mesh is refined (EDWARDS; ZHENG, 2008).

3.1.4 Multi-Point Flux Approximation with a Diamond Stencil

The Multi-Point Flux Approximation with a Diamond stencil is a non-orthodox member of the family of CVD-MPFA schemes. It was first developed by Gao & Wu (2010) and brought to the multiphase flow context by Contreras et al. (2016). Like other methods in the MPFA family, the MPFA-D was devised to tackle limitations of the standard Two-Point Flux Approximation (TPFA). Similar to MPFA-FPS (FRIIS; EDWARDS, 2011), the diamond employs a full pressure support for each subcell of the discrete domain. Hence, this scheme does not suffer from decoupled solution modes and can produce well-behaved and consistent solutions with significantly less visible spurious oscillations compared to the earlier CVD-MPFA methods. Before proceeding, let us define a lemma to compute the pressure gradient within a given triangle using the information about its geometry and the pressure values defined on its vertices:

Lemma 3.1.1. *(GAO; WU, 2010) Let $\triangle OPQ$ be a triangle with vertices O, P, Q ordered counterclockwise. The pressure gradient $\vec{\nabla}p$ inside this triangle is defined as:*

$$\vec{\nabla}p \simeq \frac{p_q - p_p}{|PQ|^2}\overrightarrow{PQ} + \frac{\mathcal{R}\overrightarrow{PQ}}{|PQ|^2}[(p_p - p_o)\cot\angle PQO + (p_q - p_o)\cot\angle OPQ] \tag{3.16}$$

where $\mathcal{R}$ is a two-dimensional 90° clockwise rotation matrix.

The MPFA-D is also derived based on the same two hypotheses: Fluxes are continuous, and piecewise linear across different control volumes. Let us consider a fragment of a non k-orthogonal two-dimensional mesh as illustrated in Figure 4. The diamond region is formed by connecting the centroids of two adjacent control volumes to the nodes I and J that comprise a shared face Γ_j creating two triangles. If we apply Lemma 3.1.1 to the left triangle $\triangle IJ\hat{L}$, we obtain:

Figure 4 – Diamond stencil (light blue region) of the MPFA-D is created by connecting the centroids of two adjacent control volumes $\hat{L}$ and $\hat{R}$ with the nodes I and J that comprise a shared face Γ_j (dark blue).

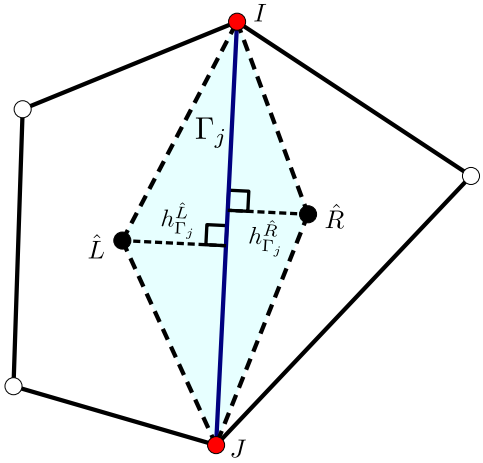

Source: Adapted from (SOUZA et al., 2022).

$$\vec{\nabla} p \simeq \frac{p_I - p_J}{|IJ|^2}\overrightarrow{IJ} + \frac{\mathcal{R}\overrightarrow{IJ}}{|IJ|^2}[(p_I - p_{\hat{L}})\cot\angle IJ\hat{L} + (p_J - p_{\hat{L}})\cot\angle \hat{L}IJ] \tag{3.17}$$

The permeability tensor $\underline{K}$ can be decomposed in terms of the tangential and normal permeabilities components, as it follows:

$$\underline{K}_{\Gamma_j(i)} = K^t_{\Gamma_j(i)}\frac{\vec{\Gamma}_i}{|\vec{\Gamma}_i|} + K^n_{\Gamma_j(i)}\frac{\vec{N}_{\Gamma_j}}{|\vec{\Gamma}_i|} \tag{3.18}$$

where $\vec{\Gamma}_i = \overrightarrow{IJ}$, the superscript t and n denote the tangential and normal components, the subscript $(i) = L, R$, and $\vec{N}_{\Gamma_j} = \mathcal{R}\vec{\Gamma}_i$.

We find an expression for the normal and tangential permeabilities by manipulating equation (3.18):

$$K^n_{\Gamma_j(i)} = \frac{\vec{N}^T_{\Gamma_j}\underline{K}_{\Gamma_{j(i)}}\vec{N}_{\Gamma_j}}{|\Gamma_j|^2} \tag{3.19}$$

$$K^t_{\Gamma_j(i)} = \frac{\vec{N}^T_{\Gamma_j}\underline{K}_{\Gamma_{j(i)}}\vec{\Gamma}_j}{|\Gamma_j|^2} \tag{3.20}$$

where the superscript T represent the transpose operation.

Based on the geometry of the diamond stencil illustrated in Figure 4, we can write the following expressions for the cotangent of the angles $\angle IJ\hat{L}$ and $\angle\hat{L}IJ$.

$$\cot\angle IJ\hat{L} = \frac{\overrightarrow{J\hat{L}}\cdot(-\vec{\Gamma}_j)}{|\Gamma_j|h^{\hat{L}}_{\Gamma_j}} \tag{3.21}$$

$$\cot \angle \hat{L}IJ = \frac{\overrightarrow{I\hat{L}} \cdot \vec{\Gamma}_j}{|\Gamma_j| h^{\hat{L}}_{\Gamma_j}} \tag{3.22}$$

If we substitute equations (3.19) and (3.20) in (3.18), and the resulting expression in (2.8), we find a discrete form of the Darcy's velocity for the left volume. If we multiply it by vector area $\vec{N}$ of Γ_j, we find the Darcy's flow :

$$(\vec{v} \cdot \vec{N})^L_{\Gamma_j} \simeq -\lambda_{\Gamma_j} [K^n_{\Gamma_{j(\hat{L})}} \left((p_I - p_{\hat{L}}) \cot \angle IJ\hat{L} + (p_J - p_{\hat{L}}) \cot \angle \hat{L}IJ \right) - K^t_{\Gamma_{j(\hat{L})}} (p_I - p_J)] \tag{3.23}$$

where λ_{Γ_j} is the face mobility calculated for the left triangle. In this work we use the approximation defined by equation (3.9).

If we substitute equations (3.19) to (3.22) in the previous equation and manipulate the resulting expression, we obtain:

$$\frac{h^{\hat{L}}_{\Gamma_j}}{\lambda_{\Gamma_j} K^n_{\Gamma_{j(\hat{L})}}} (\vec{v} \cdot \vec{N})^L_{\Gamma_j} \simeq -\frac{1}{|\Gamma_j|} \left((p_I - p_{\hat{L}}) \frac{\overrightarrow{J\hat{L}} \cdot (-\vec{\Gamma}_j)}{|\Gamma_j|} + (p_J - p_{\hat{L}}) \frac{\overrightarrow{I\hat{L}} \cdot \vec{\Gamma}_j}{|\Gamma_j|} \right) - (p_I - p_J) h^{\hat{L}}_{\Gamma_j} \frac{K^t_{\Gamma_{j(\hat{L})}}}{K^n_{\Gamma_{j(\hat{L})}}} \tag{3.24}$$

We can repeat this process and write a similar expression for the right triangle $\triangle I\hat{R}J$:

$$\frac{h^{\hat{R}}_{\Gamma_j}}{\lambda_{\Gamma_j} K^n_{\Gamma_{j(\hat{R})}}} (\vec{v} \cdot \vec{N})^R_{\Gamma_j} \simeq -\frac{1}{|\Gamma_j|} \left((p_J - p_{\hat{R}}) \frac{\overrightarrow{J\hat{R}} \cdot \overrightarrow{JI}}{|\Gamma_j|} + (p_I - p_{\hat{R}}) \frac{\overrightarrow{I\hat{R}} \cdot \overrightarrow{IJ}}{|\Gamma_j|} \right) - (p_I - p_J) h^{\hat{R}}_{\Gamma_j} \frac{K^t_{\Gamma_{j(R)}}}{K^n_{\Gamma_{j(R)}}} \tag{3.25}$$

By definition, a finite volume approximation is only consistent if the flux is unique and continuous across Γ_j. Therefore, we can write:

$$-(\vec{v} \cdot \vec{N})^L_{\Gamma_j} = (\vec{v} \cdot \vec{N})^R_{\Gamma_j} = (\vec{v} \cdot \vec{N})_{\Gamma_j} \tag{3.26}$$

If we subtract the equations (3.25) from (3.24) and use the resulting expression in (3.26), we can manipulate the outcome as follows to define the unique MPFA-D flux over any surface Γ_j:

$$(\vec{v} \cdot \vec{N})_{\Gamma_j} \simeq \tau_{\Gamma_j} [p_{\hat{R}} - p_{\hat{L}} - \nu_{\Gamma_j} (p_J - p_I)] \tag{3.27}$$

The scalar transmissibility coefficient τ_{Γ_j} and the non-dimensional tangential component ν_{Γ_j} of the flux in equation (3.27) are defined as:

$$\tau_{\Gamma_j} = -\lambda_{\Gamma_j} |\Gamma_j| \frac{K^n_{\Gamma_{j(L)}} K^n_{\Gamma_{j(R)}}}{K^n_{\Gamma_{j(L)}} h^{\hat{R}}_{\Gamma_j} + K^n_{\Gamma_{j(R)}} h^{\hat{L}}_{\Gamma_j}} \tag{3.28}$$

$$\nu_{\Gamma_j} = \frac{\vec{\Gamma}_j \cdot \overrightarrow{\hat{L}\hat{R}}}{|\Gamma_j|^2} - \frac{1}{|\Gamma_j|} \left(\frac{K^t_{\Gamma_{j(L)}}}{K^n_{\Gamma_{j(L)}}} h^{\hat{L}}_{\Gamma_j} + \frac{K^t_{\Gamma_{j(R)}}}{K^n_{\Gamma_{j(R)}}} h^{\hat{R}}_{\Gamma_j} \right) \tag{3.29}$$

Figure 5 – Diamond stencil (light blue region) of the MPFA-D on k-orthogonal grid, $\vec{\Gamma_j}$ and $\overrightarrow{\hat{L}\hat{R}}$ are perpendicular.

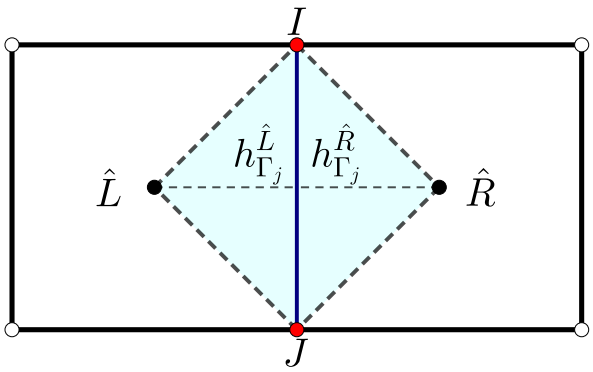

Source: Author.

It is worth noting that on a k-orthogonal grid, such as the one in Figure 5, the permeability tensor principle axes are aligned, $\Gamma_j \perp \overrightarrow{\hat{L}\hat{R}}$ leading to $\vec{\Gamma_j} \cdot \overrightarrow{\hat{L}\hat{R}} = 0$ in equations (3.21), (3.22). As a consequence the non-dimensional tangential v_{Γ_j} component in equation (3.29) is also zero, reducing the MPFA-D to the standard TPFA as defined by equation (3.15).

3.1.4.1 Multi-Point Flux Approximation Boundary Conditions

The MPFA-D flux for a control volume subjected to Dirichlet boundary conditions is a direct consequence of the flux expression given in equation (3.24):

$$(\vec{v}\cdot\vec{N})_{\Gamma_j} \simeq -\frac{\lambda_{\Gamma_j} K^n_{\Gamma_j}}{h^{\hat{L}}_{\Gamma_j}|\Gamma_j|}\left[(-\overrightarrow{J\hat{L}}\cdot\vec{\Gamma_j})g_D(I) + \overrightarrow{I\hat{L}}\cdot\vec{\Gamma_j}g_D(J) - p_{\hat{L}}|IL|^2\right] - K^t_{\Gamma_j}(g_D(J) - g_D(I)) \tag{3.30}$$

where $g_D(I)$ and $g_D(J)$ are prescribed pressures on node I and J, respectively.

The flux expression for control volumes subjected to Neumann boundary conditions is defined as:

$$(\vec{v}\cdot\vec{N})_{\Gamma_j} = g_D|\Gamma_j| \tag{3.31}$$

where g_D represents the prescribed flux over Γ_j.

3.1.4.2 Interpolation of the Pressure Computed on Auxiliary Nodes

To obtain a consistent cell-centred finite volume approximation, the pressure must be calculated at the centres of the control volumes, which in most cases is the centre of mass of the CV. However, the MPFA-D discretisation of the Darcy flow in equation (3.27) relies on pressure values calculated at the auxiliary nodes I and J that

comprise the analysed face Γ_j. To overcome this problem, we define the pressure at these nodes as a linear combination of the pressure at the control volumes around these nodes. It follows:

$$p_I = \sum_{k=1}^{n_I} w_k p_k \tag{3.32}$$

where n_I is the number of volumes around I and w_k is the weight attributed to pressure p_k.

In this work we employ the Linearity-Preserving Explicit Weighted interpolation, which has been shown to be robust for simulations in anisotropic and heterogeneous media (CONTRERAS et al., 2016). The details of the derivation of these weights can be found in the appendix of this thesis.

3.1.5 Discrete Maximum Principle

Let us consider $Mp = Q$ a linear system of equations obtained from an arbitrary flux discretization. It is possible to number the elements of this system, such that the the Dirichlet boundary $\partial\Omega_D$ and internal volumes Ω are combined together as:

$$\begin{bmatrix} M_{\Omega\Omega} & M_{\Omega\partial\Omega_D} \\ M_{\partial\Omega_D\Omega} & M_{\partial\Omega_D\partial\Omega_D} \end{bmatrix} \begin{bmatrix} p_\Omega \\ p_{\partial\Omega_D} \end{bmatrix} = \begin{bmatrix} Q_\Omega \\ Q_{\partial\Omega_D} \end{bmatrix} \tag{3.33}$$

The solution for internal control volumes p_Ω of the resulting block matrix system of equations (3.33) is defined as:

$$p_\Omega = M_{\Omega\Omega}^{-1}(Q_\Omega - M_{\Omega\partial\Omega_D} p_{\partial\Omega_D}) \tag{3.34}$$

It is often convenient to highlight in the system of equations the Dirichlet boundaries. With no loss of generalization we can represent the new system $Mp = Q$, as:

$$\begin{bmatrix} M_{\Omega\Omega} & M_{\Omega\partial\Omega_D} \\ 0 & I \end{bmatrix} \begin{bmatrix} p_\Omega \\ p_{\partial\Omega_D} \end{bmatrix} = \begin{bmatrix} Q_\Omega \\ g_D \end{bmatrix} \tag{3.35}$$

The inverse of M in equation (3.35) can be written as:

$$M^{-1} = \begin{bmatrix} M_{\Omega\Omega}^{-1} & -M_{\Omega\Omega}^{-1} M_{\Omega\partial\Omega_D} \\ 0 & I \end{bmatrix} \tag{3.36}$$

Before introducing the definition of the Discrete Maximum Principle (DMP) henceforth, a matrix inequality refers to an element-wise operation where all matrix entries hold the inequality unless explicitly stated otherwise.

Definition 3.1.2. (PRICE, 1968) A non-singular square matrix M is said to be monotone if for any vector x, $Mx \geq 0$ implies in $x \geq 0$. In other words, a matrix is monotone if $M^{-1} \geq 0$.

From equation (3.36), we can infer that if M^{-1} is monotone, $M^{-1}_{\Omega\Omega} > 0$, and $M_{\Omega\partial\Omega_D} < 0$.

Definition 3.1.3. (EDWARDS; ZHENG, 2008; KUZMIN; SHASHKOV; SVYATSKIY, 2009) A monotone matrix M is called an M-matrix, if it obeys the following relations:

$$\begin{aligned} m_{i,i} &> 0 \qquad \forall i \\ m_{i,j} &\leq 0 \qquad \forall i,j \quad i \neq j \\ \sum_j m_{i,j} &> 0 \qquad \forall i \end{aligned} \tag{3.37}$$

Definition 3.1.4. A matrix M is irreducible, if there are no permutation matrix P such that:

$$P^T M P = \begin{bmatrix} M_{1,1} & M_{1,2} \\ 0 & M_{2,2} \end{bmatrix} \tag{3.38}$$

where $M_{1,1}, M_{1,2}$ and $M_{2,2}$ are square matrices.

Theorem 3.1.2. *(VARGA, 2009; KUZMIN; SHASHKOV; SVYATSKIY, 2009) If M is an irreducible diagonally dominant matrix then $M > 0$.*

$$\begin{aligned} m_{i,i} &> 0 \qquad \forall i \\ m_{i,j} &\leq 0 \qquad \forall i,j \quad i \neq j \end{aligned} \tag{3.39}$$

A consequence of the definition (3.1.3) is that if M is a M-Matrix, by definition is monotone as well. The M-matrix is a desirable property because it ensures fast convergence of iterative solvers (EDWARDS, 2000; KUZMIN; SHASHKOV; SVYATSKIY, 2009; VARGA, 2009).

The Discrete Maximum Principle refers to any analogous definition of the continuous maximum principle for a discrete system.

Definition 3.1.5. (KUZMIN; SHASHKOV; SVYATSKIY, 2009) The linear system of equations (3.35) holds the DMP if:

$$Q \geq 0 \longrightarrow p \geq 0 \tag{3.40}$$

while a positive maxima is attained on the boundaries for $Q_\Omega \leq 0$:

$$\max_k p_k \leq \max_j \{0, g_{Dj}\} \tag{3.41}$$

or a positive minima is attained on the boundaries for $Q_\Omega \geq 0$:

$$\min_k p_k \geq \min_j \{0, g_{Dj}\} \tag{3.42}$$

and if there are not source and sink terms $Q_\Omega = 0$, i.e.

$$\min_j \{0, g_{Dj}\} \leq \min_k p_k \leq \max_j \{0, g_{Dj}\} \tag{3.43}$$

The Discrete Maximum Principle is also interchangeably used to refer to the discrete maximum and minimum principles. More details on the definition and the proofs of the theorems above are found in (KUZMIN; SHASHKOV; SVYATSKIY, 2009; VARGA, 2009). It should be noted that DMP conditions are defined globally, i.e. where the maximum/minimum values are at the boundary. However, in (EDWARDS; ZHENG, 2008; EDWARDS; ZHENG, 2010) it is shown that the M-matrix conditions ensure that each solution value is a convex average of its neighbours, which is consistent with the solution having no local spurious extrema. This property became known as local DMP (LDMP) because it ensures that each solution value is a convex average of its neighbours consistent with the solution having no local spurious extrema. Note that LDMP does not follow from global DMP.

3.1.6 M-Matrix Flux Splitting

The M-Matrix Flux Splitting is a technique proposed by (EDWARDS, 2000) for CVD-MPFA formulations that splits the CVD-MPFA matrix in terms of TPFA and cross-diffusion terms (CDT) flux producing an iterative semi-implicit scheme driven by the TPFA matrix and ensuring mass conservation at each iteration level. In the Finite Volume context, diagonally dominant M-matrices are obtained with the most common and basic discrete operator, the TPFA. Nevertheless, most problems related to petroleum reservoirs require a flux approximation that is consistent for anisotropic media that are not aligned with the principal axes of the mesh (EDWARDS; ZHENG, 2010). The main idea of the M-Matrix Flux Splitting method is to create a semi-implicit scheme that exploits the fast convergence feature of the M-Matrix property of TPFA, where the only matrix to be inverted is a symmetric positive definite M-matrix, even on unstructured grids. In addition a key motivation is to enable standard simulators to include full-tensor problems with the standard TPFA method solver. The resulting framework produced results comparable to those of full matrix inversion, and eliminated $O(1)$ errors in the flow caused by the standard diagonal tensor formulation commonly employed at that time in many existing simulators at the time (EDWARDS, 2000). To summarise this technique, let us define a linear system of equations obtained with an arbitrary CVD-MPFA.

$$M_{\mathrm{MPFA}} p = Q_{\mathrm{MPFA}} \tag{3.44}$$

With no loss of generality, we can split M_{MPFA} in equation (3.44) in terms of M_{TPFA} and M_{CDT}:

$$M_{\mathrm{TPFA}} p + M_{\mathrm{CDT}} p = Q_{\mathrm{TPFA}} + Q_{\mathrm{CDT}} \quad \text{where} \quad M_{\mathrm{CDT}} = M_{\mathrm{MPFA}} - M_{\mathrm{TPFA}}, \quad Q_{\mathrm{CDT}} = Q_{\mathrm{MPFA}} - Q_{\mathrm{TPFA}} \tag{3.45}$$

To derive the semi-implicit scheme, the pressure associate with M_{MPFA} and M_{CDT}

are put at different iteration level, resulting on the following reoccurrence law:

$$M_{\text{TPFA}} p^{n+1} = Q_{\text{CDT}} + Q_{\text{TPFA}} - M_{\text{CDT}} p^{n} \tag{3.46}$$

The convergence of the method is discussed (EDWARDS, 2000), and the method is stable if:

$$\| I - M_{\text{TPFA}}^{-1} M_{\text{MPFA}} \|_{\infty} \leq 1 \tag{3.47}$$

where I stands for the identity matrix and the subscript ∞ represents the infinity norm.

Note that the algebraic nature of the equation allows this method to be employed in 3-D as in 2-D. The only requirement for the recurrence law is to provide a transmissibility matrix M_{MPFA} assembled using a consistent flux approximation. Another major advantage of this technique is the ability to generate conservative solutions at each iteration level. In other words, it is possible to obtain approximate solutions within a given tolerance in a few steps, capturing off-diagonal effects while ensuring conservation of mass. Later, Pal & Edwards (2006), Pal & Edwards (2011) developed a non-linear version of this scheme by developing a pressure limiter that modifies the pressure solution to mitigate the loss of monotonicity of the original method.

3.1.7 Non-Linear Flux Limited Splitting

The Flux Limited Splitting (FLS) is a non-linear generalization of the work of (EDWARDS; ZHENG, 2010; PAL; EDWARDS, 2006; PAL; EDWARDS, 2011). The idea was to devise a general repair technique for linear CVD-MPFA based on the M-Matrix Flux Splitting but limiting the amount of cross-diffusion of the original CVD technique to improve or restore the DMP whilst maintaining mass conservation.

3.1.7.1 Divergence Operator and the Face Transmissibility Matrix

The motivation to design the Divergent Operator comes from the need to find a matrix form of the mass conservation equation as a function of a matrix expression of the fluxes. This allows the standard transmissibility matrix in equation (3.11) to be written in terms of multiplication of the divergent operator by a face transmissibility matrix.

We start by applying the Divergence theorem to a discrete control volume Ω_j in Ω. By definition, we have:

$$\sum_{\Gamma_j \in \partial\Omega_k} \vec{N}_j = \vec{0} \quad \forall \Omega_k \in \Omega \tag{3.48}$$

To generalise this idea, we define $\mathbf{N}$ as a vector containing the n_f area normal vectors associated with every face in $\Gamma_j \in \Omega$, as:

$$\mathbf{N} = [\vec{N}_j]_{n_f \times 1} = \begin{bmatrix} \vec{N}_1 \\ \vec{N}_2 \\ \cdots \\ \vec{N}_{n_f} \end{bmatrix} \tag{3.49}$$

Note that $\vec{N}_j$ has no particular orientation in regard to any specific control volumes.

The idea is to define a discrete operator $\mathbb{D}$ that performs the divergence theorem in all control volumes of Ω. Since no orientation is established in $\mathbf{N}$, $\mathbb{D}$ needs to be defined taking into consideration this information, such that:

$$\mathbb{D}\mathbf{N} = \vec{0} \tag{3.50}$$

Thus, we define the Discrete Divergence Operator $\mathbb{D}$ as:

$$\mathbb{D} = (d_{kj})_{n_v \times n_f} \quad \text{such as} \quad d_{kj} = \begin{cases} 0 & \Gamma_j \notin \Omega_k \\ \gamma(k,j) & \Gamma_j \in \Omega_k \end{cases} \quad \text{where} \quad \gamma(k,j) = \begin{cases} 1 & \vec{N}_j \cdot \overrightarrow{\hat{L}\hat{R}} > 0 \\ -1 & \text{otherwise} \end{cases} \tag{3.51}$$

where $\overrightarrow{\hat{L}\hat{R}}$ is a vector that connects the centroids of the control volumes to the left and to the right of the face Γ_j.

Using a similar notation, we can define an array containing any vector property $\vec{X}$ interpolated on a face and oriented in accordance with the orientation of the area vectors in $\mathbf{N}$ as:

$$\mathbf{X} = [\vec{X}_i]_{n_f \times 1} = \begin{bmatrix} \vec{X}_1 \\ \vec{X}_2 \\ \cdots \\ \vec{X}_{n_f} \end{bmatrix} \tag{3.52}$$

We define the operation $\odot$ as the element-wise inner product between two vector arrays $\mathbf{X}$ and $\mathbf{Y}$, such that:

$$\mathbf{X} \odot \mathbf{Y} = [\vec{X}_j \cdot \vec{Y}_j] \tag{3.53}$$

We can use these definitions to write a matrix form of the flux expression:

$$\mathbf{V} \odot \mathbf{N} = [(\vec{v} \cdot \vec{N})_j] \tag{3.54}$$

We can interpret the previous flux expression, as the following matrix operation:

$$(\mathbf{V} \odot \mathbf{N})_{\text{FA}} = T_{\text{FA}} p - F_{\text{FA}} \tag{3.55}$$

where T represents the face transmissibility matrix, a $n_f \times n_v$ sparse matrix that stores the coefficients of a flux approximation giving by the subscript (FA = TPFA, MPFA), and where F_{FA} represents boundary conditions terms that are later added to the RHS.

By applying the Discrete Divergence Operator on equation (3.54), and by expanding, we can write a generalization for the mass conservation equation, as:

$$\mathbb{D}(\mathbf{V} \odot \mathbf{N}) = \left[\sum_{\Gamma_j \in \partial\Omega_k} (\vec{v} \cdot \vec{N})_j \right]_{n_v} = [Q_k]_{n_v} = Q_s \tag{3.56}$$

where Q_s represents the wells source and sink term.

Using the previous definitions we can write the discrete form of the mass conservation equation as it follows:

$$M_{\text{FA}} p = Q_{\text{FA}} \quad \text{with} \quad M_{\text{FA}} = \mathbb{D} T_{\text{FA}} \quad Q_{\text{FA}} = Q_s + \mathbb{D} F_{\text{FA}} \tag{3.57}$$

Therefore, the linear system of equations can be written as:

$$\mathbb{D} T_{\text{FA}} p = Q_s + \mathbb{D} F_{\text{FA}} = Q_{\text{FA}} \tag{3.58}$$

3.1.7.2 Flux Limited Splitting Formulation

Let us define the flux array expression of a MPFA in terms of the TPFA and the CDT components, similar to the M-Matrix Flux Splitting (EDWARDS, 2000) :

$$(\mathbf{V} \odot \mathbf{N})_{\text{MPFA}} = (\mathbf{V} \odot \mathbf{N})_{\text{TPFA}} + (\mathbf{V} \odot \mathbf{N})_{\text{CDT}} \tag{3.59}$$

By replacing Equations (3.55) written for the TPFA and MPFA in (3.59), we can define the flux of CDT as:

$$(\mathbf{V} \odot \mathbf{N})_{\text{CDT}} = T_{\text{CDT}} p - F_{\text{CDT}} \quad \text{with} \quad T_{\text{CDT}} = T_{\text{MPFA}} - T_{\text{TPFA}}, \; F_{\text{CDT}} = F_{\text{MPFA}} - F_{\text{TPFA}} \tag{3.60}$$

As the TPFA is known for respecting the DMP, the idea behind our technique is to create a parameter that limits the cross diffusion terms. Therefore, a Flux Limited Splitting (FLS) expression is written as:

$$(\mathbf{V} \odot \mathbf{N})_{\text{FLS}} = (\mathbf{V} \odot \mathbf{N})_{\text{TPFA}} + B(\mathbf{V} \odot \mathbf{N})_{\text{CDT}} \quad \text{with} \quad B = \begin{bmatrix} \beta_1 & \dots & \beta_{n_f} \end{bmatrix}^T I \tag{3.61}$$

To ensure that $(\mathbf{V} \odot \mathbf{N})_{\text{FLS}}$ is the convex combination of the TPFA and MPFA solutions, β_j needs to be bounded as:

$$0 \leq \beta_j \leq 1 \tag{3.62}$$

If we apply the Discrete Divergence Operator on equation (3.61) and add the source and sink terms, we obtain the discrete mass conservation equation as:

$$\mathbb{D}(\mathbf{V} \odot \mathbf{N})_{\text{FLS}} = \mathbb{D}(\mathbf{V} \odot \mathbf{N})_{\text{TPFA}} + \mathbb{D}B(\mathbf{V} \odot \mathbf{N})_{\text{CDT}} = Q_s \tag{3.63}$$

Using flux definitions of the TPFA and CDT face transmissibility, we have:

$$\mathbb{D}T_{\text{FLS}}p = \mathbb{D}T_{\text{TPFA}}p + \mathbb{D}BT_{\text{CDT}}p - \mathbb{D}F_{\text{TPFA}} - \mathbb{D}BF_{\text{CDT}} = Q_s \tag{3.64}$$

We can finally derive the Flux Limited Splitting recurrence law:

$$\mathbb{D}T_{\text{TPFA}}p^{n+1} = Q_s + \mathbb{D}F_{\text{TPFA}} + \mathbb{D}B^nF_{\text{CDT}} - \mathbb{D}B^nT_{\text{CDT}}p^n \tag{3.65}$$

It is also possible to write equation (3.65) as:

$$M_{\text{TPFA}}p^{n+1} = Q_{\text{TPFA}} + Q^n_{\text{LCDT}} - M^n_{\text{LCDT}}p^n \tag{3.66}$$

where subscript LCDT stands for limited cross diffusion terms, and where:

$$Q_{\text{TPFA}} = Q_s + \mathbb{D}F_{\text{TPFA}}, \quad Q^n_{\text{LCDT}} = \mathbb{D}B^nF_{\text{CDT}} \quad \text{and} \quad M^n_{\text{LCDT}} = \mathbb{D}B^nT_{\text{CDT}} \tag{3.67}$$

3.1.7.3 Relaxation of the Cross Diffusion Terms

At this point, we still need to define an algorithm to compute a relaxation of the cross diffusion terms.The best scenario is to find a B^n for each iteration n level that maximizes the amount of cross diffusion and mitigates the spurious oscillations of the MPFA solution. By premultiplying equation (3.66) by M^{-1}_{TPFA}, we can isolate p^{n+1}:

$$p^{n+1} = p_{\text{TPFA}} + AM^{-1}_{\text{TPFA}}(Q^n_{\text{CDT}} - M^n_{\text{LCDT}}p^n) \quad \text{where} \quad p_{\text{TPFA}} = M^{-1}_{\text{TPFA}}Q_{\text{TPFA}} \tag{3.68}$$

To do so, let us suppose that instead of limiting the flux, the limitation was imposed at the volume level, on the balance cross diffusion terms. Therefore, we could write equation (3.68) as:

$$p^{n+1} = p_{\text{TPFA}} + M^{-1}_{\text{TPFA}}(Q^n_{\text{CDT}} - M^n_{\text{LCDT}}p^n) \quad \text{where} \quad A = \begin{bmatrix}\alpha_1 & \dots & \alpha_{n_v}\end{bmatrix}^T I \quad \text{where} \quad 0 \leq \alpha_n \leq 1 \tag{3.69}$$

As a result of the the Local Discrete Maximum Principle (EDWARDS; ZHENG, 2008; EDWARDS; ZHENG, 2010) between two distinct iteration levels n and $n+1$, the following inequality must also hold:

$$\min(p^n_k) \leq p^{n+1}_k \leq \max(p^n_k) \tag{3.70}$$

where $\min(p^n_k)$ and $\max(p^n_k)$ represent, respectively, the minimum and the maximum pressure values of any volume that shares a node with an element k.

We can expand p^{n+1} using the definition given in equation (3.68):

$$\min(p_k^n) \leq p_{\text{TPFA}\,k} + \alpha_k W_k \leq \max(p_k^n) \quad \text{with} \quad W_k = [M_{\text{TPFA}}^{-1}(Q_{\text{LCDT}}^n - M_{\text{LCDT}}^n p^n)]|_k \tag{3.71}$$

After some algebraic manipulation, we obtain the following interval in which α_k ensures that p_k^n satisfies the DMP:

$$L_k : \begin{cases} \left[\min(p_k^n) - p_{\text{TPFA}\,k}\right] \Big/ W_k \leq \alpha_k \leq \left[\max(p_k^n) - p_{\text{TPFA}\,k}\right] \Big/ W_k & W_k > 0 \\ \left[\max(p_k^n) - p_{\text{TPFA}\,k}\right] \Big/ W_k \leq \alpha_k \leq \left[\min(p_k^n) - p_{\text{TPFA}\,k}\right] \Big/ W_k & W_k < 0 \end{cases} \tag{3.72}$$

To avoid extrapolation, we limit each interval with:

$$K_k : L_k \cap [0,1] \tag{3.73}$$

We define the relaxation parameter associated with the balance of the cross diffusion terms as:

$$\alpha_k = \begin{cases} \max(N_k) & K_k \neq \varnothing \\ 1 & K_k = \varnothing \end{cases} \tag{3.74}$$

At this point, the limitation factor is computed for each control volume. To obtain a relaxation parameter for a face Γ_j, we use the following relation:

$$\beta_j = \min(\alpha_L, \alpha_R) \tag{3.75}$$

where L and R represent respectively, the control volumes neighbours to the left and right of the face j.

Note that solving $B^n = B(p^n)$, and $p^n(B^n)$ is a non-linear optimization procedure that maximises B within a fixed interval while ensuring that p is constrained by the DMP.

3.1.7.4 Stability

Unlike the work of (EDWARDS, 2000) that computes the solution of the MPFA system of equations using the semi-implicit relation in equation (3.46), the FLS system of equation is modified at every iteration according to equation (3.64). Therefore, it is natural to study the stability of each iteration n.

Let p_H be the exact solution of the implicit FLS system of equations, such that:

$$\mathbb{D}T_{\text{FLS}}^n p_H = \mathbb{D}T_{\text{TPFA}} p_H + \mathbb{D}B^n T_{\text{CDT}} p_H - \mathbb{D}F_{\text{TPFA}} - \mathbb{D}B^n F_{\text{CDT}} = Q_{\text{s}} \tag{3.76}$$

If we subtract equation (3.76) from the semi-implicit law of recurrence of the FLS in Equation (3.65), we have:

$$\mathbb{D}T_{\text{TPFA}} e^{n+1} + \mathbb{D}B^k T_{\text{CDT}} e^n = 0 \tag{3.77}$$

with the relative discrete solution error $e^{n+1} = p^{n+1} - p_H$ and $e^n = p^n - p_H$.

If we solve equation (3.77) row-wise affter some algebraic manipulation, we have:

$$e^{n+1} = M_{\text{TPFA}}^{-1} M_{\text{CDT}}^n e^n \quad \text{with} \quad M_{\text{CDT}}^n = \mathbb{D} B^n T_{\text{CDT}} \tag{3.78}$$

A method is known to be stable if its spectral radius is bounded by unity (HIRSCH, 2002; EDWARDS, 2000), which follows:

$$\|M_{\text{TPFA}}^{-1} M_{\text{CDT}}^n\|_\gamma = \|I - M_{\text{TPFA}}^{-1} M_{\text{FLS}}^n\|_\gamma \leq 1 \quad \text{with} \quad M_{\text{CDT}}^n = M_{\text{FLS}}^n - M_{\text{TPFA}} \tag{3.79}$$

calculated using a γ norm.

The constrains imposed on β ensure that M_{FLS}^n is always bounded by M_{MPFA}^n and M_{TPFA}^n. This way, as we update B, the restrictions on the cross diffusion terms increase the overall stability of FLS as M_{FLS}^n becomes closer to M_{TPFA}^n. This increases the stability of the M-Matrix Flux Splitting, allowing our formulation to converge even in cases the original flux splitting did not.

3.1.7.5 Flux Limited Splitting Algorithm

After extensively testing the formulation presented in the previous subsections, we developed the following algorithm, which is shown in three flowcharts. The main algorithm, depicted in Flowchart 1, consists of three fundamental steps. The first is the preprocessing stage, where the divergent operator, face transmissibility, and other auxiliary entities are calculated. The second step is the heart of the FLS method, the Flux Limitation algorithm, a set of routines described by the flowchart in Figure 2 that limit the cross-diffusion terms to mitigate the unphysical oscillations. It is worth noting that in this step the pressure solution is calculated within a tolerance large enough to capture the violations of the DMP, but not too small to allow p to converge. The third and final step is the solver itself. In this step, an arbitrary solver is used. For iterative solvers, it is good practise to use the unconverged pressure solution as the initial estimate. In this work, the standard M-Matrix Flux splitting is used as the iterative solver in all the cases tested. The Flux Limitation, described in Flowchart 2, again consists of several different subroutines. In particular, the functions *FindAlpha* and *FindBeta* are an implementation of the cross-diffusion relaxation algorithm described in subsection 3.1.7.3. The function *p_init*, depicted on its own Flowchart 3, describes the warm start procedure we developed, which gave the best results in all cases studied. Roughly speaking, within the first lim_{WS} the flux limitation allows the solution to iterate freely to bring p_{TPFA} closer to p_{MPFA}. After that, the flux limitation starts and if the oscillations keep the algorithm in a loop or if the tolerance is not reached after a certain number of iterations the tolerance is not reached, another cycle starts using B^k and the initial

pressure solution defined by *p_init*. Note that tol_1 and tol_2 represent the tolerances of the iterative procedure and the tolerance of the DMP test.

Flowchart 1 – Flux Limiting Splitting main algorithm.

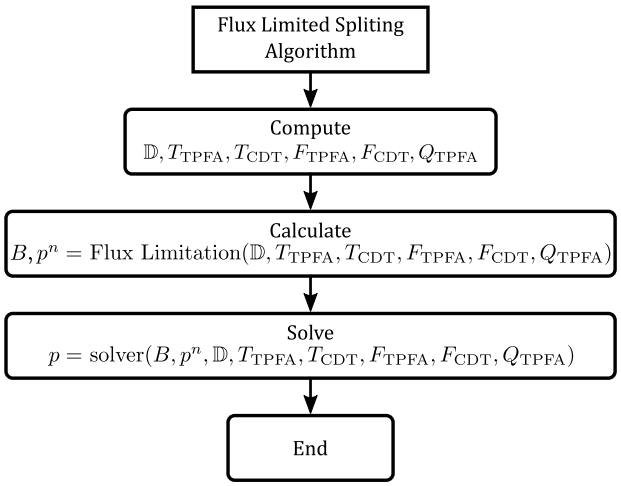

Source: Author.

Flowchart 2 – Flux Limitation algorithm: *Flux Limitation*

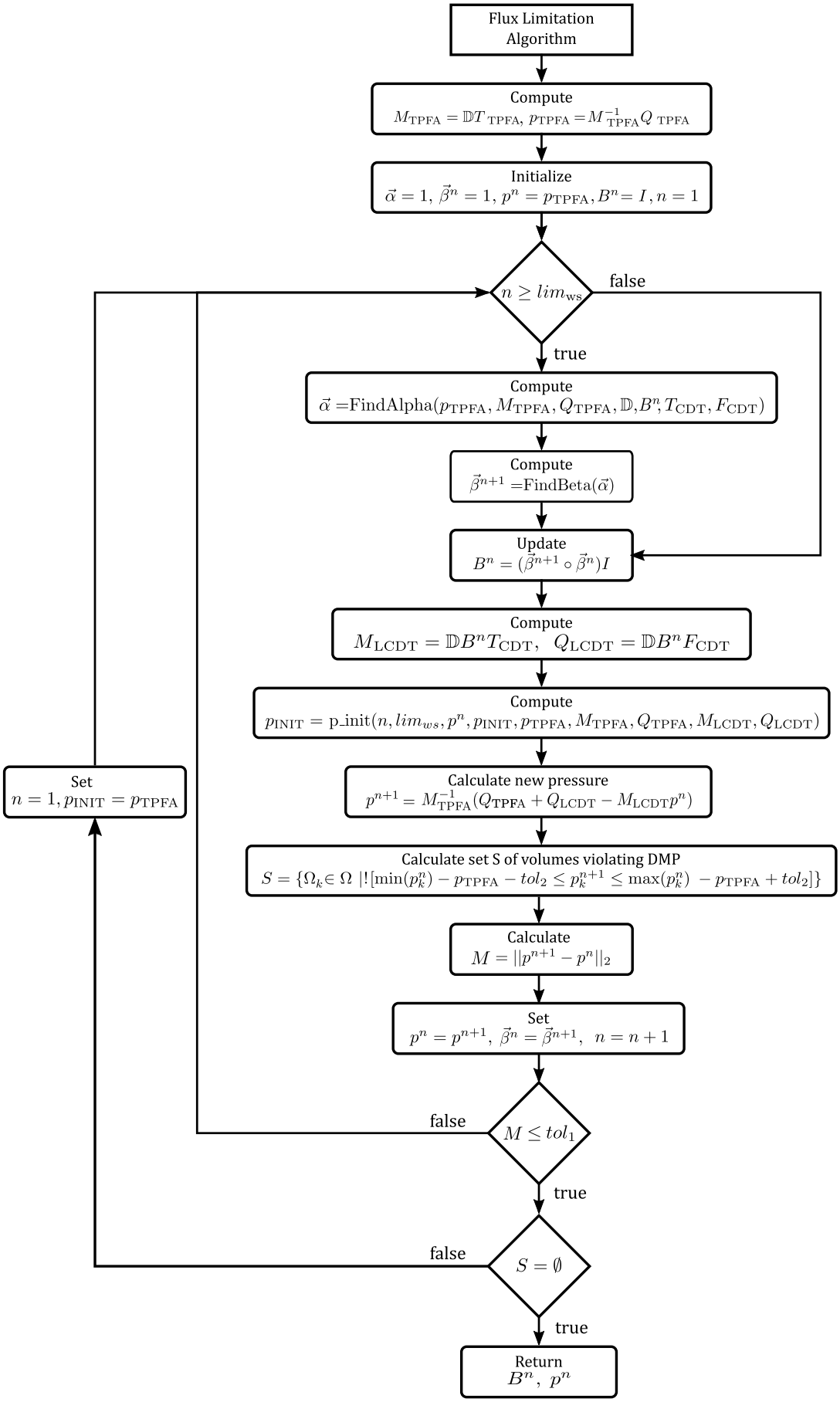

Source: Author.

Flowchart 3 – Pressure initialization algorithm: *p_int*.

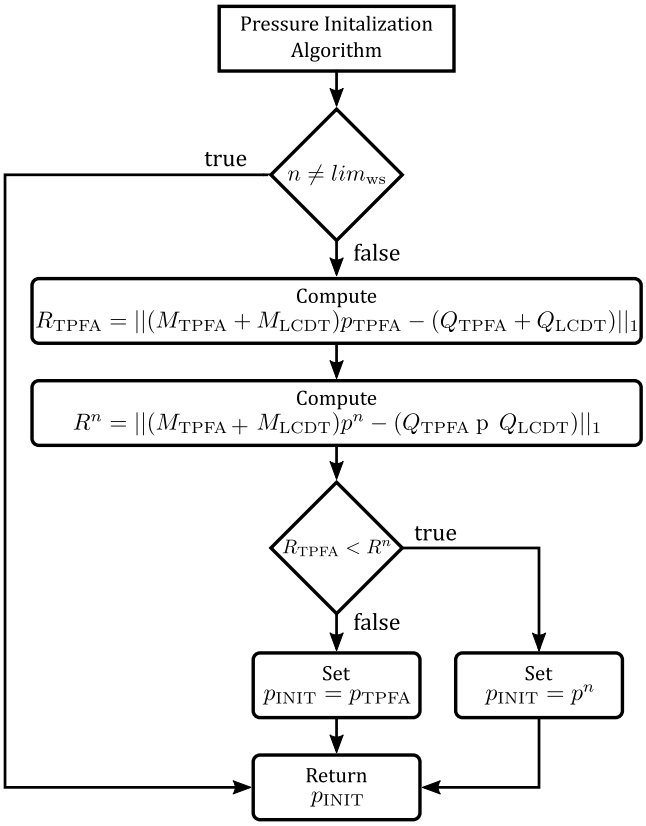

Source: Author.

3.2 Cell Centred Finite Volume Discretization of the Saturation Equation

To derive a discrete form of the saturation equation, the same assumptions used to obtain (3.7) are employed. We integrate equation (2.11) over the time interval t_o to t and over the physical domain Ω. It follows:

$$\int_{t_o}^{t}\int_{\Omega}\frac{\partial S_w}{\partial t}d\Omega dt = -\int_{t_o}^{t}\int_{\Omega}\frac{1}{\phi}\vec{\nabla}\cdot\vec{F}(S_w)d\Omega dt + \int_{t_o}^{t}\int_{\Omega}\frac{1}{\phi}Q_w d\Omega dt \tag{3.80}$$

By definition, the discrete domain is an approximation of the physical domain. Therefore, the space integral represents the summation of integrals over all control volumes Ω_k in Ω. If we apply the Gauss Theorem in the first integral on the RHS equation (3.80), we obtain:

$$\int_{t_o}^{t}\sum_{\Omega_k\in\Omega}\int_{\Omega_k}\frac{\partial S_w}{\partial t}d\Omega dt = -\int_{t_o}^{t}\sum_{\Omega_k\in\Omega}\int_{\partial\Omega_k}\frac{1}{\phi_k}\vec{F}(S_w)\cdot\vec{n}\,\partial\Omega dt + \int_{t_o}^{t}\sum_{\Omega_k\in\Omega}\int_{\Omega_k}\frac{1}{\phi_k}Q_w d\Omega dt \tag{3.81}$$

where ϕ_k represents the porosity of Ω_k.

Since Finite Volume methods are locally conservative by construction, equation

(3.81) is valid for a single control volume Ω_k, i.e.:

$$\int_{t_o}^{t}\int_{\Omega_k}\frac{\partial S_w}{\partial t}d\Omega dt = -\frac{1}{\phi_k}\int_{t_o}^{t}\int_{\partial\Omega_k}\vec{F}(S_w)\cdot\vec{n}\,d\partial\Omega dt + \frac{1}{\phi_k}\int_{t_o}^{t}\int_{\Omega_k}Q_w d\Omega dt \tag{3.82}$$

We can use the mean value theorem to approximate the following integrals:

$$\frac{1}{\phi_k}\int_{\partial\Omega_k}\vec{F}(S_w)\cdot\vec{n}\,d\partial\Omega dt \simeq \frac{1}{\phi_k}\sum_{\Gamma_j\in\partial\Omega_k}\left[\vec{F}(S_w)\cdot\vec{N}\right]_{\Gamma_j} \tag{3.83}$$

$$\frac{1}{\phi_k}\int_{t_o}^{t}\int_{\Omega_k}Q_w d\Omega \simeq \frac{1}{\phi_k}\bar{Q}_w \tag{3.84}$$

and

$$\int_{\Omega_k}\frac{\partial S_w}{\partial t}d\Omega \simeq \frac{\partial \bar{S}_w}{\partial t}\Omega_k \tag{3.85}$$

where $\bar{Q}_w$ denotes the average water source or sink term integrated over time and space.

By substituting (3.83) to (3.85) in (3.82), we have the semi-discrete form of the saturation equation:

$$\int_{t_o}^{t}\frac{\partial S_w}{\partial t}dt = -\frac{1}{\phi_{\Omega_k}\Omega_k}\int_{t_o}^{t}\sum_{\Gamma_j\in\partial\Omega_k}\left[\vec{F}(S_w)\cdot\vec{N}\right]_{\Gamma_j}dt + \frac{Q_w}{\phi_k\Omega_k} \tag{3.86}$$

For the sake of simplicity, the overbar notation is dropped henceforward.

3.2.1 Space Discretization

The space component of the saturation equation is discretized using the standard First Order Upwind (FOU). It follows:

$$\left[\vec{F}(S_w)\cdot\vec{N}\right]_{\Gamma_j} = f_w\left(\vec{v}\cdot\vec{N}\right)_{\Gamma_j} = \begin{cases} f_w^L\left(\vec{v}\cdot\vec{N}\right)_{\Gamma_j} & \chi_{\Gamma_j}\geq 0 \\ f_w^R\left(\vec{v}\cdot\vec{N}\right)_{\Gamma_j} & \text{otherwise} \end{cases} \tag{3.87}$$

where f_w^L, and f_w^R represent the fractional flows of the CV to the left and to the right of Γ_j, and χ_{Γ_j} is defined as:

$$\chi_{\Gamma_j} = \left(\vec{v}\cdot\vec{N}\right)_{\Gamma_j}\left.\frac{\partial f_w}{\partial S_w}\right|_{\Gamma_j} \tag{3.88}$$

3.2.2 Temporal Discretization

The discretization of time component term in the saturation equation is done using Backward Euler Method. It follows:

$$\int_{t_o}^{t}\frac{\partial S_w}{\partial t}dt = S_{w,k}^{n+1} - S_{w,k}^{n} \tag{3.89}$$

where $S_{w,k}^{n+1}$ and $S_{w,k}^{n}$ are, respectively, the water saturation on Ω_k at the time level n, and $n+1$.

By replacing (3.89) in (3.86), manipulating and integrating over time, we obtain the discrete saturation equation:

$$S_{w,k}^{n+1} = S_{w,k}^{n} - \left\{ \frac{\Delta t}{\phi_k \Omega_k} \sum_{\Gamma_j \in \partial\Omega_k} \left[\vec{F}(S_w) \cdot \vec{N} \right]_{\Gamma_j} + \frac{\Delta t Q_w}{\phi_k \Omega_k} \right\}^{n+1} \tag{3.90}$$

where the time step $\Delta t = t^{n+1} - t^n$ represents the time integration.

3.2.3 Implicit Saturation Equation

The discretization of the saturation equation using the Euler Forward introduced a non-linear term in equation (3.90) that needs a proper treatment. Therefore, we employ the Newton-Raphson method (BURDEN; FAIRES, 2011) to solve the non-linear system of equations to handle the fractional flow $f_w^{n+1} = f_w(S_w^{n+1})$. Hence, it is convenient to write the saturation equation in a matrix function form, highlighting the non-linear term f_w^{n+1}:

$$\mathbf{H}(\mathbf{S_w^{n+1}}) = \mathbf{S_w^n} + \Delta t \underline{G}^n \mathbf{f_w^{n+1}} - \mathbf{S_w^{n+1}} \tag{3.91}$$

where $\mathbf{H}(\mathbf{S_w^{n+1}})$ is a multi-variable function written in terms of $\mathbf{S_w^{n+1}}$, an array containing the saturation $S_{w,k}^{n+1}$ of all control volumes; $\mathbf{S_w^n}$ and $\mathbf{f_w^{n+1}}$ are similarly defined arrays for respectively $S_{w,k}^{n}$, and $f_{w,k}^{n+1}$; and where $\underline{G}^n$ is defined as:

$$\underline{G}^n = (g_{kl})_{n_v \times n_v} \quad \text{with} \quad g_{kl}^n = \begin{cases} \frac{1}{\phi_k \Omega_k} \left[Q_k - \sum_{\Gamma_j \in \partial\Omega_k} \eta_{k,j} (\vec{v} \cdot \vec{N})_{\Gamma_j}^n \right] & k = l \\ (1 - \eta_{l,j}) \frac{(\vec{v} \cdot \vec{N})_{\Gamma_j}^n}{\phi_k \Omega_k} & k \neq l, \quad \Gamma_j = \partial\Omega_k \cap \partial\Omega_l \\ 0 & k \neq l, \quad \Gamma_j = \emptyset \end{cases} \tag{3.92}$$

where $\eta_{k,j}$ is defined as:

$$\eta_{i,j} = \begin{cases} 1 & \text{if } \Omega_i \text{ is upwind to } (\vec{v} \cdot \vec{N})_{\Gamma_j}^n \\ 0 & \text{otherwise} \end{cases} \tag{3.93}$$

The goal of the Newtown-Raphson method is to find $\mathbf{H}(\mathbf{S_w^{n+1}}) = 0$. To do so, we use the Taylor series to expand $\mathbf{H}(\mathbf{S_w^{n+1}})$, up to the first order, around an approximation of its roots $\tilde{\mathbf{S}}_\mathbf{w}^{\mathbf{n+1}}$:

$$\mathbf{H}(\mathbf{S_w^{n+1}}) = 0 \approx \mathbf{H}(\tilde{\mathbf{S}}_\mathbf{w}^{\mathbf{n+1}}) + \left. \frac{\partial \mathbf{H}}{\partial \mathbf{S_w^{n+1}}} \right|_{\tilde{\mathbf{S}}_\mathbf{w}^{\mathbf{n+1}}} (\mathbf{S_w^{n+1}} - \tilde{\mathbf{S}}_\mathbf{w}^{\mathbf{n+1}}) \tag{3.94}$$

By definition, the derivative of $\mathbf{H}(\mathbf{S_w^{n+1}})$ is the Jacobian matrix, defined as:

$$\left.\frac{\partial \mathbf{H}}{\partial \mathbf{S_w^{n+1}}}\right|_{\tilde{\mathbf{S}}_\mathbf{w}^{\mathbf{n+1}}} = \underline{J}(\tilde{\mathbf{S}}_\mathbf{w}^{\mathbf{n+1}}) = \Delta t \underline{G}^n \left.\frac{\partial \mathbf{f_w^{n+1}}}{\partial \mathbf{S_w^{n+1}}}\right|_{\mathbf{S_w^{n+1}}} - I \tag{3.95}$$

where I is the identity matrix with the same size as $\underline{G}^n$.

By setting the saturations $\tilde{\mathbf{S}}_\mathbf{w}^{\mathbf{n+1}} = \mathbf{S_w^{n+1,\gamma}}$ and $\mathbf{S_w^{n+1}} = \mathbf{S_w^{n+1,\gamma+1}}$ in equation (3.94), computed in reference to the γ iteration level of the Newton-Raphson method, we obtain :

$$\mathbf{H}(\mathbf{S_w^{n+1,\gamma}}) + \underline{J}(\mathbf{S_w^{n+1,\gamma}})(\mathbf{S_w^{n+1,\gamma+1}} - \mathbf{S_w^{n+1,\gamma}}) \approx 0 \tag{3.96}$$

We find the Newton-Raphson recurrence law (BURDEN; FAIRES, 2011) by rearranging, and premultiplying by $\underline{J}^{-1}(\mathbf{S_w^{n+1,\gamma}})$ the previous equation:

$$\mathbf{S_w^{n+1,\gamma+1}} = \mathbf{S_w^{n+1,\gamma}} + \underline{J}^{-1}(\mathbf{S_w^{n+1,\gamma}})\mathbf{r}^\gamma \tag{3.97}$$

where the residue $\mathbf{r}^\gamma$ is defined as:

$$\mathbf{r}^\gamma = \mathbf{H}(\mathbf{S_w^{n+1,\gamma}}) = \mathbf{S_w^n} + \Delta t \underline{G}^n \mathbf{f_w^{n+1,\gamma}} - \mathbf{S_w^{n+1,\gamma}} \tag{3.98}$$

and where:

$$\underline{J}(\mathbf{S_w^{n+1,\gamma}}) = \Delta t \underline{G}^n \left.\frac{\partial \mathbf{f_w^{n+1,\gamma}}}{\partial \mathbf{S_w^{n+1}}}\right|_{\mathbf{S_w^{n+1,\gamma}}} - I \tag{3.99}$$

with the convergence criterion for a given tolerance tol defined as:

$$\max(\mathbf{r}^\gamma) \leq tol \tag{3.100}$$

3.3 Coupling Strategy

Once the discretisations of the pressure and saturation equations are defined, it is essential to define the coupling strategy for the simulation of two-phase flows, which determines how these equations are connected. We use a segregated formulation in which the saturation equations are solved implicitly. While the pressure equation is solved using one of the schemes defined on subsection 3.1, the saturation equation always uses the strategy on subsection 3.2. Figure 6 is a flowchart describing the coupling strategy. First, the initial saturation field is used to calculate the total mobility, solve the numerical pressure equation and calculate the Darcy's flow. We use this velocity field as input to solve the transport equation to update the saturation field. If a time-dependent condition is met, the simulation comes to an end. Otherwise, the process is restarted using the new saturation as the initial condition. The coupling strategy for the simulation of two-phase flows with the multiscale methods described in the next chapter is defined similarly. The only difference is that in these methods the

pressure field and the Darcy's flows are computed with an approximate multiscale field obtained after a step to reimpose mass conservation.

Figure 6 – Diagram depicting the coupling between the pressure equation and saturation equation solvers.

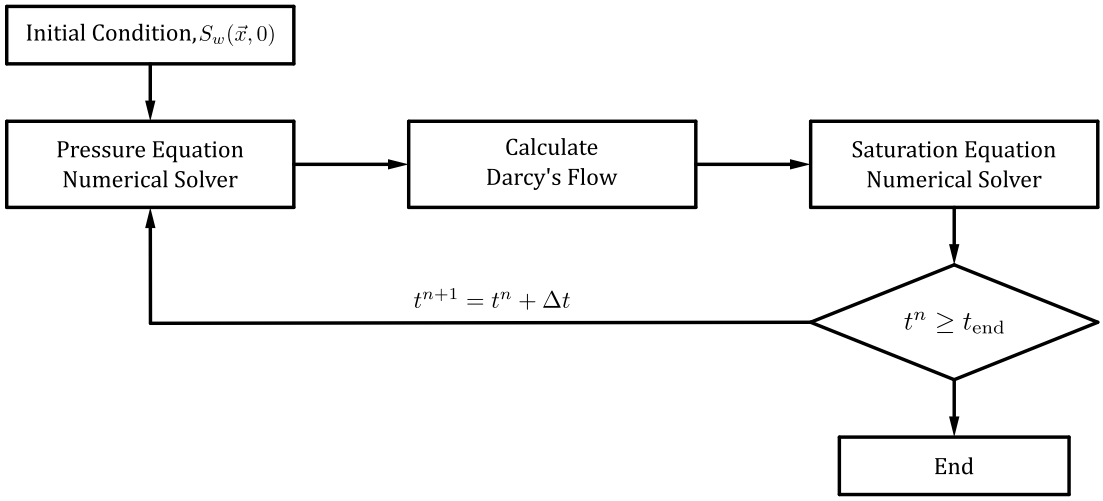

Source: Adapted from (SOUZA, 2018).

3.4 Approximation Errors

In order to assess the robustness and quality of the solution of the numerical schemes developed in this section, we need to define the associated approximation errors. For this purpose, we calculate the errors with respect to the reference solution. We use the analytical solution of the same problem unless explicitly stated otherwise. We define the (L_2) and (L_∞) norms of the error of a variable $\vec{X}$ as:

$$\|\vec{X}^{ref} - \vec{X}\|_2 = \sqrt{\frac{\sum_{\Omega_i \in \Omega} \Omega_i |x_i^{ref} - x_i|^2}{\sum_{\Omega_i \in \Omega} |x_i^{ref}|^2}} \quad \text{and} \quad \|\vec{X}^{ref} - \vec{X}\|_\infty = \max_{\Omega_i \in \Omega} \Omega_i |x_i^{ref} - x_i| \quad (3.101)$$

where $\vec{X}^{ref}$ and $\vec{X}$ represent an array containing the reference and the numerical solutions, respectively; where x_i^{ref} represents the reference solution calculated at the centre of the CV Ω_i, and x_i represents its numerical counterpart.

4 MULTISCALE FINITE VOLUME FORMULATION

Multiscale methods are a family of approximate scale-transferring solvers that allow the use of high-resolution geological grids in standard reservoir simulations. Unlike upscaling techniques, where information is transferred from a high-resolution scale and remains in the low-resolution scale, multiscale methods create a set of operators to project the fine-scale system of equations onto the space of a coarse-scale grid. The new system is then solved and later projected back onto the space of the high resolution mesh to compute a reasonably accurate conservative solution (ZHOU; TCHELEPI, 2008). The idea behind this and other related multiscale methods is that solving a set of localised high-resolution systems together with a global problem at the coarse scale (LUNATI; TYAGI; LEE, 2011) is cheaper than a direct simulation at the high-resolution scale. The Multiscale Finite Volume (MsFV) methods are a subset of the multiscale family, capable of generating mass-conservative solutions at any simulation scale(LUNATI; JENNY, 2006; ZHOU; TCHELEPI, 2008; JENNY; LUNATI, 2009; LUNATI; JENNY, 2008; LEE; WOLFSTEINER; TCHELEPI, 2008). Moreover, the iterative multiscale family is able to converge the multiscale solution to the fine scale solution(HAJIBEYGI et al., 2008; HAJIBEYGI; JENNY, 2011a; LUNATI; TYAGI; LEE, 2011). In this way, multiscale methods can be applied in three different ways: i) as a robust upscaling technique, ii) as an approximate fine-scale solver that produces conservative solutions, and iii) as an initial guess in an iterative procedure that ensures that the multiscale solution converges within a certain tolerance to the fine-scale simulation results (ZHOU; TCHELEPI, 2008; SOUZA et al., 2020). This chapter presents the formulation and associated methods used to develop the multiscale formulation devised in this thesis. The multiscale preprocessing algorithms have a chapter apart in the appendix A where the Background grid strategy is introduced.

4.1 Multiscale Finite Volume Method

Before presenting the multiscale formulation developed in this thesis, it is necessary to define the notation and discuss common aspects inherent in the Multiscale Finite Volume family. To this end, we will review the original Multiscale Finite Volume method (JENNY; LEE; TCHELEPI, 2003; JENNY; LEE; TCHELEPI, 2006) using the matrix notation developed by Zhou & Tchelepi (2008), which has become the standard for representing multiscale methods. We begin with an introduction to the basic concepts of the multiscale finite volume formulation.

Figure 7 – Illustration of the multiscale entities for methods in the MsFV family on structured and unstructured grids: Fine-scale Mesh Ω (light grey), Primal Coarse Grid Ω^p(solid black lines), Dual Coarse Grid Ω^d elements and their wirebasket hierarchical classification: Primal Coarse Volumes Centres x^p or Nodes (yellow) , Dual Coarse Boundaries or Edges (red), Dual Coarse Volumes or Internals (white).

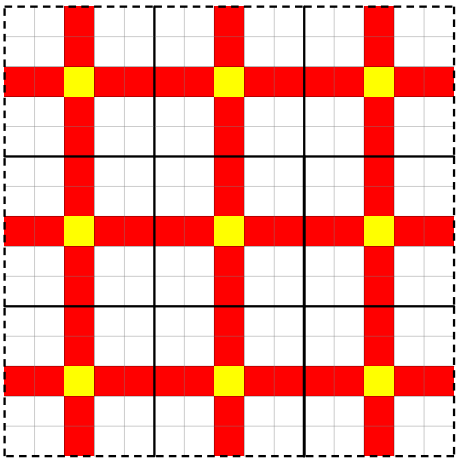

(a) Structured grid with quadrilateral fine-scale volumes.

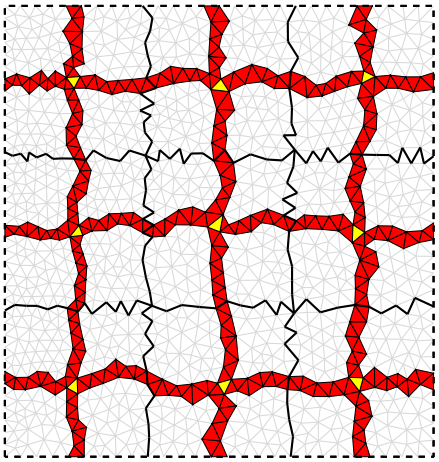

(b) Unstructured grid with triangular fine-scale volumes.

Source: (SOUZA et al., 2022)

Fine-scale Mesh (Ω^f or Ω): The fine-scale mesh is simply a mesh that represents the higher resolution grid used in a simulation. For this reason, the fine-scale mesh is also represented by the mesh notation given in section 3.1. It is often the same grid in which the petrophysical properties are estimated. In Figure 7a this grid is shown in light grey.

Primal Coarse Mesh (Ω^p): The primal coarse mesh is a low-resolution grid generated by the agglomeration of all fine-scale volumes into primal coarse volumes. It is represented by the solid black lines in the Figures 7a and 7b.

Primal Coarse Volume (Ω_k^p): A primal coarse volume or simply coarse volume is a set of face-connected fine-scale volumes such that no coarse volume shares the same fine-scale volume. In other words, it consists in another subdivision of Ω in a set of $\{\Omega_k^p\}_{k=1}^{n_v^p}$ of n_v^c volumes such that $\left\{\Omega_i \in \Omega_k^p | \Omega_i \cap \Omega_k^p - \Omega_i = S\right\}$ where $S = \left\{\Omega_p\right\}_{p=1}^{n_p}$ with $n(S) > 0$.

Primal Coarse Volume Boundaries ($\partial\Omega_k^p$): The boundaries of a coarse volume Ω_k is a set defined as $\partial\Omega_k^p = \{\Gamma_j^p \in \Omega_k^p\}$

Primal Coarse Volume Face or Surface (Γ_j^p): A coarse volume face or surface is a set fine-scale faces such that $\{\Gamma_j^p\}_{j=1}^{n_f^p} = \partial\Omega_i^p \cap \partial\Omega_j^p \ \forall \Omega_i^p, \Omega_j^p \in \Omega^p$ with $i \neq j$ and $\Gamma_j \neq \emptyset$.

Figure 8 – Illustration of a primal coarse mesh Ω^p with 9 primal coarse volumes ($n_v^p = 9$) and 24 primal coarse faces ($n_f^p = 24$). The boundary of the central primal coarse volume $\partial\Omega_5^p$ (dark blue) whose centre x_5^p (yellow fine-scale volume) is comprised by the primal coarse faces $\{\Gamma_{15}^p, \Gamma_{19}^p, \Gamma_{21}^p, \Gamma_{21}^p\}$ whose primal coarse faces centres are $\{y_{15}^p, y_{19}^p, y_{21}^p, yp_{21}\}$ (fine-scale face in red) respectively.

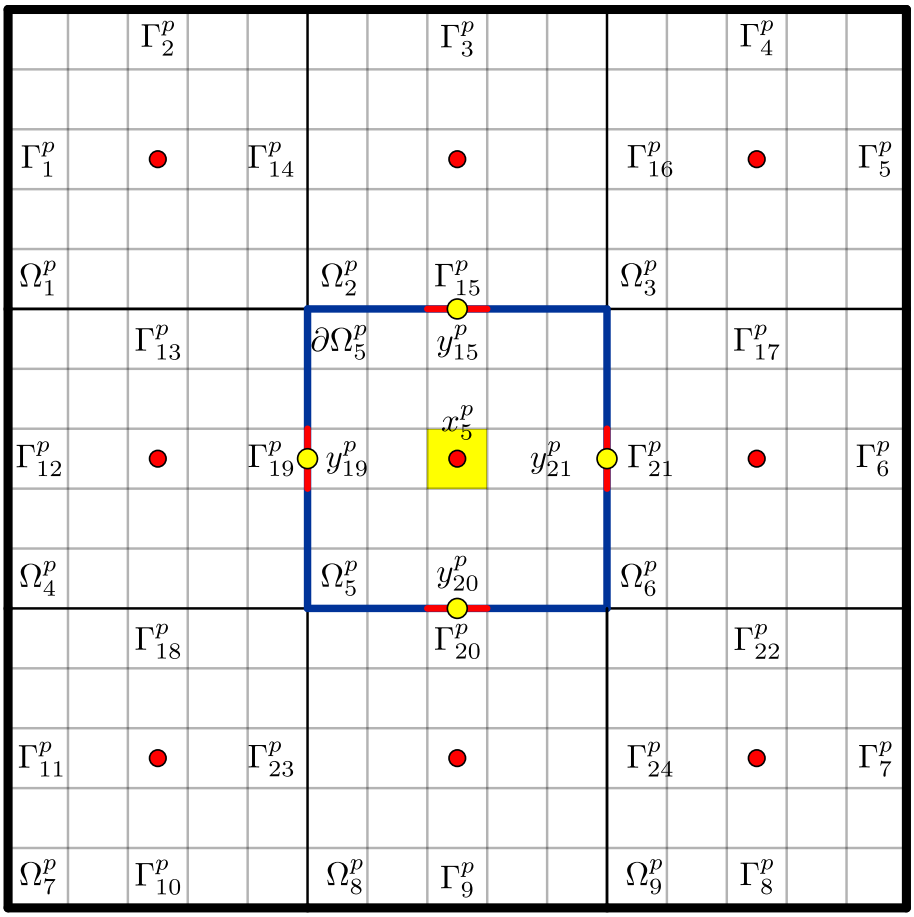

Source: Author

Primal Coarse Centre (x_k^p): The primal coarse centre of a coarse volume Ω_k^p is a fine-scale volume that represent the centre and eventually the primal coarse volume itself. Standard multiscale methods often rely on using the fine-scale volume closest to centroid of a coarse volume, while multiscale schemes that work with general unstructured grids employ special routines to determine the coarse volume centres as the coarse cells are not necessarily convex (MOYNER; LIE, 2015; SOUZA et al., 2020). The centres are illustrated by the yellow fine-scale volumes in Figure 7. In the wirebasket ordering of the dual-coarse mesh, the primal coarse centres are also referred as the nodes or node group. Check Section 4.2 for an explanation of the wirebasket classification.

Primal Coarse Face Centre (y_j^p): The primal face centre of a primal coarse face Γ_j^p a fine-scale face that represent the centre of the primal coarse face itself.

Dual Coarse Mesh (Ω_c^d or Ω^d): The dual coarse mesh is a low-resolution auxiliary mesh used to ensure mass conservation at the boundaries of the primal coarse volumes and later used by the flux reconstruction algorithm to retrieve local conservative fluxes. In the standard Muiltiscale Finite Volume method that uses structured grids, the centres of the coarse volumes are connected to other coarse volumes that share a common primal coarse face. This creates a set of face-connected fine-scale volumes that form the boundaries of the dual coarse volume. Note that primal coarse volumes are excluded from this group. The fine-scale volumes inside this boundaries are referred as dual coarse volume internal cells.

Prolongation Operator ($\underline{P}_{op}$) and Restriction Operators ($\underline{R}_{op}$): The Prolongation and Restriction operators are at the core of all multiscale schemes in general. These operators were developed to project the fine-scale system of equations onto the coarse-scale space, where a solution is obtained, which is then projected back onto the high-resolution space (ZHOU; TCHELEPI, 2008; SOUZA et al., 2020). The multiscale solution at the fine scale is written as a convex combination of the pressures in the coarse-scale space weighted by sets of basis functions. These sets of basis functions, arranged in a matrix form, are called the Prolongation operator. Therefore, by definition, the Prolongation operator projects the coarse solution onto the fine-scale mesh. The restriction operator, in turn, maps the influence of the fine-scale source and sink terms to the coarse scale.

Support Region of a Primal Coarse Volume (I_k): The Support Region of a Primal Coarse Volume I_k represents a set of fine-scale volumes that form the area of influence of a primal coarse volume Ω_k^p. In standard multiscale methods, I_k consists of all dual coarse volumes that share x_k^P. By definition, the support area of a primal coarse volume Ω_k^p is the influence area of x_k^p, where:

$$(\underline{P}_{op})_{k,i} \neq 0 \;\; \forall \Omega_i \in I_i \tag{4.1}$$

Boundaries of a Support Region of a Primal Coarse Volume (∂I_k): The Boundaries of a Support Region of a Primal Coarse Volume ∂I_k represents a set of fine-scale volumes that share at least one node with a control volume in I_k. By definition, they are outside the I_k.

Multiscale Errors: Multiscale methods can be used to efficiently approximate the numerical solution at the fine-scale. Therefore, the reference solution used to evaluate the multiscale errors is obtained by direct simulation at the fine scale. Thus, the

Euclidean norm (L_2) and the infinity norm (L_∞) of a variable $\vec{X}$ are defined as:

$$\|\vec{X}^{ref} - \vec{X}^{ms}\|_2 = \sqrt{\frac{\sum_{\Omega_i \in \Omega^f} |x_i^{ref} - x_i^{ms}|^2}{\sum_{\Omega_i \in \Omega^f} |x_i^{ref}|^2}} \quad \text{and} \quad \|\vec{X}^{ref} - \vec{X}^{ms}\|_\infty = \max_{\Omega_i \in \Omega^f} |x_i^{ref} - x_i^{ms}| \tag{4.2}$$

where the superscripts ms and ref represent the multiscale and reference approximations, respectively; and where x_i represents the x values associated with Ω_i.

4.1.1 Multiscale Finite Volume Algebraic Notation

As we mentioned earlier, the following notation developed by Zhou & Tchelepi (2008) allows us to interpret the Multiscale Finite Volume Method as a series of simple matrix multiplications. Let us start by defining the fine-scale system of equation similarly to (3.11).

$$M_f p_f = Q_f \tag{4.3}$$

where M_f is the transmissibility matrix of the fine-scale system, Q_f is the corresponding volumetric source and sink terms, and p_f is the fine-scale pressure solution. M_f represents the TPFA matrix for most methods in the MsFV family.

By definition, the prolongation operator projects the coarse-scale pressure solution onto the fine-scale space. For this purpose, the prolongation operator $\underline{P}_{op}$ is then defined as follows:

$$p_f \simeq p_{ms} = \underline{P}_{op} p_c \tag{4.4}$$

where p_f is the fine-scale pressure solution, p_{ms} is the fine-scale multiscale pressure solution and p_c is the coarse-scale multiscale pressure solution.

The restriction operator, in turn, is an operator that transfer the influence of the of source and sink terms to the coarse volumes. As a result, we define the source and sink terms on the coarse scale Q_c as:

$$Q_c = \underline{R}_{op} Q_f \tag{4.5}$$

If we premultiply equation (4.15) by $\underline{R}_{op}$ and approximate p_f with the definition of p_{ms} in equation (4.4), we find:

$$\underline{R}_{op} M_f \underline{P}_{op} p_c = \underline{R}_{op} Q_f \tag{4.6}$$

We can thus interpret the equation (4.6) as a projection of the fine-scale system of equations onto the coarse-scale space. It follows that:

$$M_c p_c = Q_c \tag{4.7}$$

where Q_c is defined by equation (4.5) and M_c is:

$$M_c = \underline{R}_{op} M_f \underline{P}_{op} \tag{4.8}$$

By solving equation (4.7), we find:

$$p_c = M_c^{-1} Q_c \tag{4.9}$$

With $\underline{P}_{op}$ we can project p_c back to the fine scale and obtain the multiscale solution p_{ms}:

$$p_{ms} = \underline{P}_{op} p_c = \underline{P}_{op} M_c^{-1} Q_c = \underline{P}_{op} (\underline{R}_{op} M_f \underline{P}_{op})^{-1} \underline{R}_{op} Q_f \tag{4.10}$$

4.1.2 Definition of the Multisale Operator

Having defined the algebraic notation, we still lack a definition for $\underline{P}_{op}$ and $\underline{R}_{op}$ to formally define the MsFV method. On this method, the basis functions ϕ^i associated with each coarse volume Ω_i^c are computed by solving a normalized version of the pressure equation (2.9) subjected to specific Dirichlet boundary conditions (HAJIBEYGI et al., 2008) designed to decouple the associated support region I_i from the rest of the computational domain.

$$\begin{cases} -\vec{\nabla} \cdot (-\lambda \underline{K} \vec{\nabla} \phi^i) = 0 & G_1 : \Omega_k \in I_i \cap \partial I_t \quad \forall \Omega_t^p \in \Omega^c \\ \phi^i = 1 & G_2 : \Omega_k^f = x_i^p \\ \phi^i = 0 & G_3 : \Omega_k^f \notin I_i \end{cases}$$

After solving ϕ in $G_1 \cup G_2 \cup G_3$, we still need to compute the basis function on the rest of the support region. To do so, we solve the following problem:

$$\begin{cases} -\vec{\nabla} \cdot (-\lambda \underline{K} \vec{\nabla} \phi^i) = 0 & I_i - G_1 \cup G_2 \cup G_3 \\ \phi^i = \phi_{\Omega_k} & \Omega_k \in G_1 \cup G_2 \cup G_3 \end{cases}$$

The basis function ϕ_k^i which represents the influence of the coarse volume Ω_i^p on the fine-scale volume Ω_k^f is stored on the prolongation operator as follows:

$$\underline{P}_{op_{k,i}} = \phi_k^i \tag{4.11}$$

The MsFV restriction operator $\underline{R}_{op}$ (JENNY; LEE; TCHELEPI, 2003; JENNY; LEE; TCHELEPI, 2006; ZHOU; TCHELEPI, 2008) is simply a switch that maps the fine-scale source and sink terms on the primal to coarse volume as follows:

$$\underline{R}_{op}(k,i) = \begin{cases} 1 & \text{se } \Omega_k^f \subset \Omega_i^c \\ 0 & \text{otherwise} \end{cases} \tag{4.12}$$

4.1.3 Flux Reconstruction Algorithm

By definition, for a method to belong to the Finite Volume family it needs to be mass conservative at all scales. However, the velocity field obtained using the pressure field of the Multiscale Finite Volume family (JENNY; LEE; TCHELEPI, 2003; JENNY; LEE; TCHELEPI, 2006; ZHOU; TCHELEPI, 2008) is mass conservative at the coarse-scale level only. This is due to the boundary conditions used to constrain the influence of the basis functions that destroy the mass conservation outside the support region at the fine-scale level, as they neglect the influence of the external control volumes. Nevertheless, the dual coarse mesh ensures that the solution is mass conservative at the coarse scale. We can take advantage of this property to reimpose mass conservation at all scales. In the following, we describe the flux reconstruction procedure (JENNY; LEE; TCHELEPI, 2003; JENNY; LEE; TCHELEPI, 2006) used in this work. First, we use the multiscale pressure solution to calculate a mass-conservative flux field at the coarse scale. These fluxes become Neumann boundary conditions to solve the pressure equation over the uncoupled primal coarse volumes. To make the problem well posed, we use the multiscale pressure solution in x^P as a Dirichlet boundary for the primal coarse volumes that do not contain other Dirichlet boundary conditions (SOUZA et al., 2020). See Figure 9. In mathematical terms, this means solving the following problem:

$$\begin{cases} -\vec{\nabla}\cdot(-\lambda\underline{K}\vec{\nabla}p_n) = q_f \quad \text{inside} \quad \Omega_i^p \\ -\frac{\partial}{\partial x_n}\left(-\lambda\underline{K}\frac{\partial}{\partial x_n}p_n\right) = (\vec{v}\cdot\vec{N})_{ms} \quad \text{on} \quad \partial\Omega_i^p \\ p_n = p_{ms} \quad \text{in} \quad x_i^p \quad \text{if} \quad \Omega_i^p \quad \text{does not contain Dirichlet BC} \end{cases} \tag{4.13}$$

where x_n is the normal direction to the boundary of the primal coarse volumes, p_{ms} is the multiscale pressure field calculated using equation (4.31), and $(\vec{v}\cdot\vec{N})_{ms}$ is the flux field calculated using p_{ms}, and where p_n is the pressure solution of the Neumman problem.

The reconstructed flux is composed of the fluxes used as Neumann boundary condition on the surfaces of each primal coarse volume and the fluxes obtained after solving the uncoupled pressure equation problem given in equation (4.13), as it follows:

$$(\vec{v}\cdot\vec{N})_{\text{conservative}} = \begin{cases} -\lambda\underline{K}\vec{\nabla}p_n \quad \text{inside} \quad \Omega_i^p \\ -\lambda\underline{K}\vec{\nabla}p_{ms} \quad \text{on} \quad \partial\Omega_i^p \end{cases} \quad \forall\Omega_i^p \in \Omega^p \tag{4.14}$$

Figure 9 – Illustration of flux reconstruction algorithm. The dual coarse mesh ensures that the solution is mass conservative at the boundaries of the coarse-scale volume.

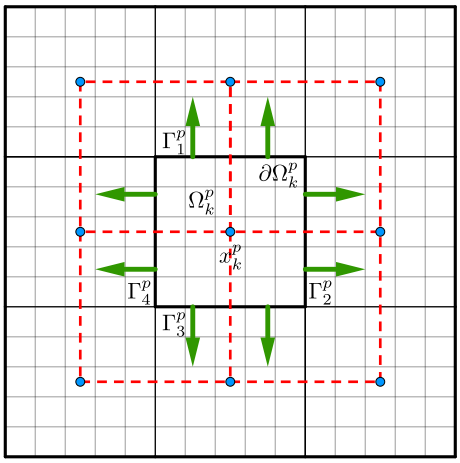

Source: Adapted from (SOUZA et al., 2020)

4.2 Algebraic Multiscale Solver

The Algebraic Multiscale Solver (AMS) (WANG; HAJIBEYGI; TCHELEPI, 2014) is a state-of-the-art method that emerged from the generalisation of the standard Multiscale Finite Volume method (JENNY; LEE; TCHELEPI, 2003; JENNY; LEE; TCHELEPI, 2006; ZHOU; TCHELEPI, 2008). The simple matrix notation allows the prolongation operator and a set of correction functions to be computed as a set of straightforward algebraic operations performed on the discrete system at a fine scale. Combined with an iterative multiscale stage, this method proves to be efficient and robust with results comparable to multigrid methods (WANG; HAJIBEYGI; TCHELEPI, 2014). In this subsection we review the standard Algebraic Multiscale Solver (AMS) (WANG; HAJIBEYGI; TCHELEPI, 2014) and consider the extension to general unstructured grids.

Wirebasket Classification The wirebasket classification is at the core (ZHOU; TCHELEPI, 2011; WANG; HAJIBEYGI; TCHELEPI, 2014; ŞENE; KOBAISI; HAJIBEYGI, 2016) of the AMS method. It consists of grouping fine-scale volumes into different categories: Nodes (x^p), Edges ($\partial I_i \forall \Omega_i^p \in \Omega^p$) and Internals (see figure 7), where Internals refers to the centres of the fine-scale cells enclosed by the (red) edges.

4.2.1 Algebraic Multiscale Solver Formulation

Let us imagine a fine-scale discretisation of the elliptic pressure equation as shown in equation (4.15):

$$M_f p_f = Q_f \tag{4.15}$$

Let G be a permutation matrix that sorts a vector according to wirebasket segregation.

$$\widetilde{X}_f = \begin{bmatrix} x_i \\ x_e \\ x_n \end{bmatrix} = GX_f \tag{4.16}$$

where the subscripts n, e,and i stand for all groups of the wirebasket segregation: nodes, edges and internals.

Let the wirebasket matrix be the transmissibility matrix permuted to combine the wirebasket categories together, i.e.:

$$\widetilde{A} = \begin{bmatrix} \widetilde{A}_{ii} & \widetilde{A}_{ie} & \widetilde{A}_{in} \\ \widetilde{A}_{ei} & \widetilde{A}_{ee} & \widetilde{A}_{en} \\ \widetilde{A}_{ni} & \widetilde{A}_{ne} & \widetilde{A}_{nn} \end{bmatrix} = GM_f G^T \tag{4.17}$$

where the block matrix $\widetilde{A}_{\alpha\beta}$ denotes the influence of α upon β, where α and β represent respective groups of the wirebasket hierarchy, and where the superscript T represents the transpose of a matrix.

The reordered linear system of equations is then written as:

$$\widetilde{A}\widetilde{p}_f = \widetilde{Q}_f \tag{4.18}$$

The AMS method forms an upper triangular matrix by neglecting the influence of block matrices below the main diagonal (WANG; HAJIBEYGI; TCHELEPI, 2014), resulting in a wirebasket matrix hierarchy where the volumes belonging to one group only have influence on other volumes of the same or higher dimensional categories. The resulting AMS system is written as follows:

$$M = \begin{bmatrix} \widetilde{A}_{ii} & \widetilde{A}_{ie} & \widetilde{A}_{in} \\ 0 & M_{ee} & \widetilde{A}_{en} \\ 0 & 0 & M_c \end{bmatrix} \tag{4.19}$$

where M is a permuted and modified version of M_f, M_c is approximated by the transmissibility matrix onto the coarse-scale, and M_{ee} receives the redistributed influence of $\widetilde{A}_{ei}$ as defined by the following equation:

$$M_{ee} = \widetilde{A}_{ee} + \text{diag}\left(\sum_k^e \widetilde{A}_{ki}\right) \tag{4.20}$$

The modified system of equations is written as:

$$Mp_{ms} = \widetilde{Q} = \begin{bmatrix} \widetilde{Q}_i \\ \widetilde{Q}_e \\ Q_c \end{bmatrix} \tag{4.21}$$

where the multiscale solution p_{ms} is an approximation of $\widetilde{p}_f$. It should be pointed out that the last line on the RHS in equation (4.21) represents the primal coarse scale source and sink terms Q_c and not not $\widetilde{Q_n}$. Therefore, $\widetilde{Q}$ is the modified source and sink terms.

Let us assume that M^{-1} can be split such that:

$$M^{-1} = \left(\begin{bmatrix} 0 & 0 & a \\ 0 & 0 & b \\ 0 & 0 & c \end{bmatrix} M_{nn}^{-1} + \begin{bmatrix} d & g & 0 \\ e & h & 0 \\ f & i & 0 \end{bmatrix} \right) \tag{4.22}$$

Since $MM^{-1} = I$, and M has an upper triangular form, M^{-1} is found by backward substitution (WANG; HAJIBEYGI; TCHELEPI, 2014).

$$M^{-1} = (\underline{P} M_c^{-1} + \underline{C}) \tag{4.23}$$

where:

$$\underline{P} = \begin{bmatrix} 0 & 0 & \widetilde{A}_{ii}^{-1}(\widetilde{A}_{ie} M_{ee}^{-1} \widetilde{A}_{en} - \widetilde{A}_{in}) \\ 0 & 0 & -M_{ee}^{-1} \widetilde{A}_{en} \\ 0 & 0 & I_{nn} \end{bmatrix} \tag{4.24}$$

where:

$$\underline{C} = \begin{bmatrix} \widetilde{A}_{ii}^{-1} & -\widetilde{A}_{ii}^{-1} \widetilde{A}_{ie} M_{ee}^{-1} & 0 \\ 0 & M_{ee}^{-1} & 0 \\ 0 & 0 & 0 \end{bmatrix} \tag{4.25}$$

Note that by definition, the last row in $\underline{C}$ is null. Therefore, the following equality holds true:

$$\underline{C} \widetilde{Q} = \underline{C} \widetilde{Q}_f \tag{4.26}$$

By premultiplying Equation (4.21) by (4.23), we find:

$$\widetilde{p}_f \simeq p_{ms} = (\underline{P} M_c^{-1} + \underline{C}) \widetilde{Q} \tag{4.27}$$

$\widetilde{p}_f$ is often written as:

$$\widetilde{p}_f \simeq p_{ms} = \underline{P} M_c^{-1} Q_c + \underline{C} \widetilde{Q} \tag{4.28}$$

where $\underline{P}_{op}$ is defined removing the two empty columns:

$$\underline{P} = \begin{bmatrix} \widetilde{A}_{ii}^{-1}(\widetilde{A}_{ie} M_{ee}^{-1} \widetilde{A}_{en} - \widetilde{A}_{in}) \\ -M_{ee}^{-1} \widetilde{A}_{en} \\ I_{nn} \end{bmatrix} \tag{4.29}$$

The pressure on the coarse scale is defined by:

$$p_c = M_c^{-1} Q_c \tag{4.30}$$

Hence, we use this definition to rewrite Equation (4.27) as:

$$p_{ms} = \underline{P} p_c + \underline{C}\widetilde{Q} \tag{4.31}$$

As $\underline{P}$ projects the coarse-scale pressure solution on to the high-resolution grid, it is referred to as the Prolongation Operator denoted by $\underline{P}_{op}$. In addition $\underline{C}$ known as the Correction Function captures complex well behaviour and other phenomena included in the fine-scale RHS and not explicitly expressed by the Prolongation Operator (WANG; HAJIBEYGI; TCHELEPI, 2014). Thus, we can rewrite Equation (4.31) as:

$$p_{ms} = \underline{P}_{op} M_c^{-1} Q_c + \underline{C}\widetilde{Q}_f \tag{4.32}$$

Using the Finite Volume restriction operator $\underline{R}_{op}$ defined in equation (4.12), we can find the projection of the fine-scale system of equations onto the coarse scale. To do this, we substitute the equation (4.31) into (4.18) and pre-multiply the result by the restriction operator to obtain:

$$\underline{R}_{op}\widetilde{A}(\underline{P}_{op} p_c + \underline{C}\widetilde{Q}_f) = \underline{R}_{op}\widetilde{Q}_f \tag{4.33}$$

By expanding and manipulating the result, we find:

$$\underline{R}_{op}\widetilde{A}\underline{P}_{op} p_c = \underline{R}_{op}\widetilde{Q}_f - \underline{R}_{op}\widetilde{A}\underline{C}\widetilde{Q}_f \tag{4.34}$$

Note that equation (4.34) represents the fine-scale system of equations projected on the coarse-scale, i.e.:

$$M_c p_c = Q_c \tag{4.35}$$

where:

$$M_c = \underline{R}_{op}\widetilde{A}\underline{P}_{op} \quad \text{and} \quad Q_c = \underline{R}_{op}\widetilde{Q}_f - \underline{R}_{op}\widetilde{A}\underline{C}\widetilde{Q}_f \tag{4.36}$$

Thus, the multiscale solution can be obtained by solving Equation (4.35) and substituting the result into (4.27) resulting in:

$$\widetilde{p_f} \simeq p_{ms} = \underline{P}_{op}(\underline{R}_{op}\widetilde{A}\underline{P}_{op})^{-1} Q_c + \underline{C}\widetilde{Q}_f \tag{4.37}$$

By definition, we find p_f by sorting it back to its original form:

$$p_f = G^T \widetilde{p}_f \tag{4.38}$$

The flux reconstruction algorithm defined on section 4.1.3 is used to ensure a locally conservative solution.

4.2.2 AMS on structured grids using the Two Point Flux Approximation

If the entries a,b and b,a in the transmissibility matrix Mf are non-zero, two fine-scale volumes a and b are said to be connected. Connections can be asserted in a standard TPFA when two volumes share an edge in 2D or a face in 3D. Since multiple entries in the wirebasket matrix are zero, there is also a natural decoupling between the categories internals and nodes, which further simplifies the computation of $\underline{P}_{op}$ and $\underline{C}$. As a result, we can rewrite equation (4.17) for the TPFA method (WANG; HAJIBEYGI; TCHELEPI, 2014) as follows:

$$\widetilde{A}_{\text{TPFA}} = \begin{bmatrix} \widetilde{A}_{ii} & \widetilde{A}_{ie} & 0 \\ \widetilde{A}_{ei} & \widetilde{A}_{ee} & \widetilde{A}_{en} \\ 0 & \widetilde{A}_{ne} & \widetilde{A}_{nn} \end{bmatrix} \tag{4.39}$$

In turn, this leads to $\underline{P}_{op}$ and $\underline{C}$ being defined as:

$$\underline{P}_{op} = \begin{bmatrix} 0 & 0 & \widetilde{A}_{ii}^{-1}\widetilde{A}_{ie}M_{ee}^{-1}\widetilde{A}_{en} \\ 0 & 0 & -M_{ee}^{-1}\widetilde{A}_{en} \\ 0 & 0 & I_{nn} \end{bmatrix} \tag{4.40}$$

and where:

$$\underline{C} = \begin{bmatrix} \widetilde{A}_{ii}^{-1} & -\widetilde{A}_{ii}^{-1}\widetilde{A}_{ie}M_{ee}^{-1} & 0 \\ 0 & M_{ee}^{-1} & 0 \\ 0 & 0 & 0 \end{bmatrix} \tag{4.41}$$

An ideal permutation matrix G would take advantage of this natural uncoupling that arises from the reordering of the internal and edge volumes, so that each dual cell and each sub-edge are separate. The sparsity representation of this resulting wirebasket matrix $\widetilde{A}_{\text{TPFA}}$ is shown in Figure 10. Note that $\widetilde{A}_{ii}$ and $\widetilde{A}_{ee}$ / M_{ee} consist of several independent block matrices that are perfectly split. From a computational point of view, finding M_{ee}^{-1} and $\widetilde{A}_{ii}^{-1}$ becomes a set of simple and small parallelizable problems. Similar to the original MsFV, the AMS solves the uncoupled basis functions hierarchically at the edges by using normalised Dirichlet boundary conditions at the nodes ensuring partition of unity. The basis functions at the edges are later used to calculate the value of the internal basis functions. Partition of unity is achieved because the sub-edges neither intersect nor connect. This in turn leads to the calculation of the prolongation operator $\underline{P}_{op}$ that converges to the standard MsFV (ZHOU; TCHELEPI, 2008; JENNY; LEE; TCHELEPI, 2003; JENNY; LEE; TCHELEPI, 2006). Therefore, it is possible to find a permutation matrix G on structured meshes that guarantees that sub-edges and dual cells can generate disconnected block matrices.

4.2.3 Algebraic Multiscale Solver for MultiPoint Flux Approximation schemes

In Control Volume Distributed MultiPoint Flux Approximation schemes, a common vertex is sufficient to establish a connection between two fine-scale control volumes.

Figure 10 – Sparsity pattern representation of a TPFA wirebasket matrix for a 2D structured mesh: The natural uncoupling of the dual grid and the sub-edges is reflected in the wirebasket matrix creating independent block matrices for each of these regions (red).

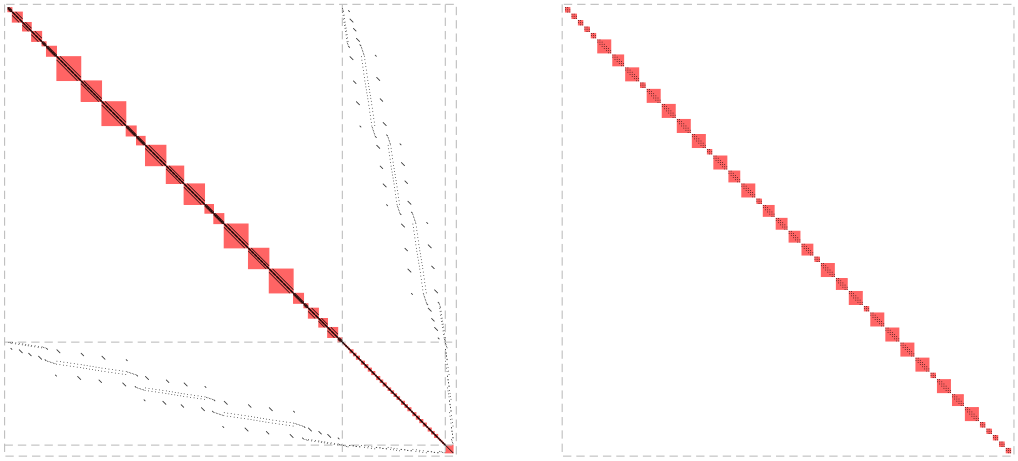

(a) $\widetilde{A}_{\text{TPFA}}$ (b) $\widetilde{A}_{ee}$ and M_{ee}

Source: (SOUZA et al., 2022).

Figure 11 – Sparsity pattern representation of a MPFA wirebasket matrix for the same 2D structured mesh as Figure 10: The natural uncoupling of the dual grid and sub-edges is lost as the block matrices (red) of wirebasket matrix remain intertwined.

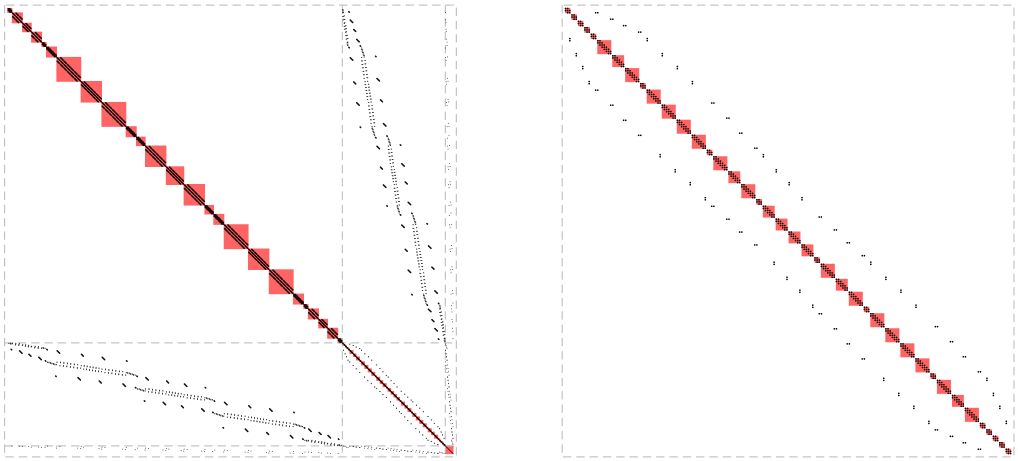

(a) $\widetilde{A}_{\text{MPFA}}$ (b) $\widetilde{A}_{ee}$ and M_{ee}

Source: (SOUZA et al., 2022).

Figure 11 illustrates the sparsity pattern of the wirebasket MPFA matrix $\widetilde{A}_{\text{MPFA}}$ assembled for the same problem used to illustrate the TPFA pattern in Figure 11. We note that the natural decoupling of the matrices M_{ee} and $\widetilde{A}_{ee}$ is lost since the sub-edges remain connected by the common nodes.

The problem worsens when we apply the AMS method to unstructured grids in

Figure 12 – Sparsity pattern representation of a MPFA wirebasket matrix for 2D unstructured fine and coarse scale meshes: The natural uncoupling of the standard AMS is broken as sub-edges and dual grid volumes block matrices (red) are indivisible and deeply connected.

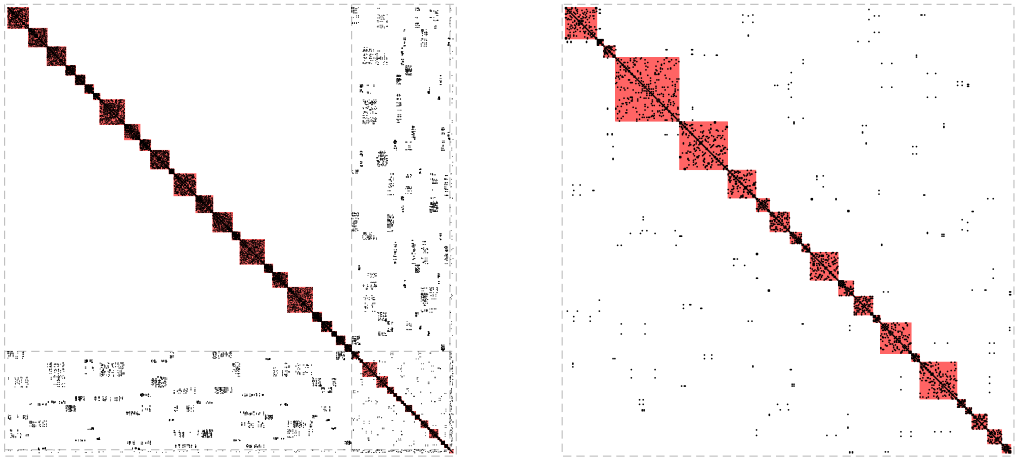

(a) $\widetilde{A}_{\text{MPFA}}$ (b) $\widetilde{A}_{ee}$ and M_{ee}

Source: (SOUZA et al., 2022).

general. The irregular nature of the underlying fine-scale mesh makes it impossible to guarantee that all sub-edges neither intersect nor connect. For example, for a quadrilateral background grid with an underlying unstructured triangular mesh, as shown in Figure 7b, each coarse cell centre must be connected to four different sub-grids. This forces the sub-edges to have at least one common fine volume. Thus, if the number of faces of the coarse cell centre is less than the number of faces of a corresponding background grid cell, the resulting sub-grids will be connected.

This phenomenon is reflected in the sparsity pattern of the wirebasket matrix illustrated in Figure 12. We note that even in a simple case, multiple sub-edges are clustered together to form large block matrices. This in turn this has two important consequences for the AMS solution introduced by the MPFA formulation. First, the clustering together of multiple sub-edges leads to the leakage of the basis functions outside the corresponding support region of each primal coarse volume. In other words, the connections among sub-edges create paths that allow the local basis function to propagate outside the region to which the reduced boundary conditions are applied. Secondly, the loss of partition of unity as the shared fine-scale volumes are subject to different boundary conditions on each edge.

4.2.4 Algebraic Multiscale Solver for Unstructured grids

To develop a consistent multiscale scheme on general unstructured grids, two conditions must be met: a more robust flux approximation must be used and a suitable multiscale solver must be employed (SOUZA et al., 2020). The first problem is solved

by using the CVD-MPFA presented in section 3.1.4 , i.e. the MPFA-D method. In this section, we address the second problem by developing an algorithm that prevents the leakage of basis functions while preserving the partition of unity and partially restoring the uncoupled nature of the AMS. Note that our method is a generalisation of the AMS for general linear flux approximation schemes and therefore other methods could be used. Hencefoward, we refer to AMS on unstructured grids with MPFA-D as AMS-U.

The idea is to analyse the second line $\underline{P}_{en}$ of the prolongation operator $\underline{P}_{op}$ defined by equation (4.24):

$$\underline{P}_{en} = -M_{ee}^{-1}\widetilde{A}_{en} \tag{4.42}$$

Mathematically, computing $\underline{P}_{en}$ is equivalent to solve:

$$M_{ee}\underline{P}_{en} = -\widetilde{A}_{en} \tag{4.43}$$

This in turn is equivalent to solving the M_{ee} system of equations of the edges restricted for all the n coarse volumes. As we know, the support region of a coarse volume is the subset of a domain that contains only non-zero elements.

In the context of multiscale problems, the support region of a basis function of the coarse volume i consists of the dual coarse volumes sharing the node i excluding the boundaries of this region.

On structured grids, sub-edges of the boundaries and the support region have no intersection. Therefore, the edges basis functions of a given support region (see Figure 13a) are computed on the entire extent of the sub-edges within the corresponding support region.

In contrast, for unstructured grids, the sub-edges (see figure 13b) within the support region may share a common volume with the sub-edges from the boundary of the support region (see figure 13c). As a result, the sub-edges within the support region are solved in a smaller domain (see Figure 13d), limiting the reach of a basis function and its ability to capture the underlying physics.

To solve this problem, we propose to solve the edges basis function on an extended support region, i.e., to use the support region I_k and the boundaries of the support region ∂I_k. Instead of solving the equation (4.43), we reformulate the problem as follows:

$$M_{e^i}\underline{P}_{e^i i} = -\widetilde{A}_{e^i i} \tag{4.44}$$

where i represents one of the n nodes, and e^i stands for the edges included in the extended support region i.

Therefore, for each i, we solve the problem restricted to the support region and the boundaries of the support region of the coarse volume i. Consequently, we explicitly

Figure 13 – Illustration of the problem risen from the intersection between the sub-edges belonging to the boundaries of the support region and those inside the support region.

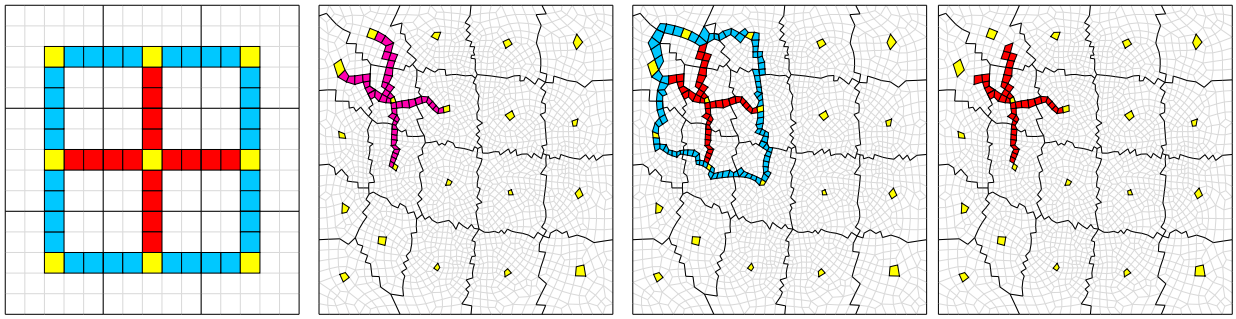

(a) Boundary of Support Region (blue) and Edges in the Support Region (red) on a structured grid.

(b) Sub-edges (pink) connecting coarse cell centres x^P (yellow) with its background grid neighbours.

(c) Boundary of Support Region (blue) and Edges in the Support Region (red).

(d) Edges in the Support Region (red).

Souce: (SOUZA et al., 2022).

restrict the influence of the edges to these regions, preventing the leakage of the basis function. Nevertheless, the value of the basis functions at the edges of the support regions is by definition zero. As soon as $\underline{P}_{e^i i}$ is calculated, the values at the boundaries of this support region are set to zero:

$$\underline{P}_{e^t i} = 0 \quad \forall t \in \text{boundary of the support region of } i \tag{4.45}$$

The superposition between the sub-edges of the dual coarse mesh and equation (4.45) breaks the partition of unity of the basis functions. We deal with this problem by using the idea proposed by Moyner & Lie (2015) to explicitly normalise $\underline{P}_{en}$:

$$\underline{P}_{en}^{cor} = \frac{\underline{P}_{en}}{\sum_{k=1}^{n} \underline{P}_{ek}} \tag{4.46}$$

where $\underline{P}_{en}^{cor}$ stands for the corrected basis functions .

Figure 14 illustrates the basis functions computed for the original support region (14a) and the extended support region (14b) on a homogeneous isotropic domain. Note that the basis function in the latter case has a better distribution within the support region. In our experience, this extended basis function has given better results in all the examples presented in the next chapter.

Figure 14 – Comparison between the basis function calculated on the support and extended support region. The boundaries of the support region and the coarse cell centres, respectively in light blue and yellow are represented to highlight the region where the basis functions are being calculated.

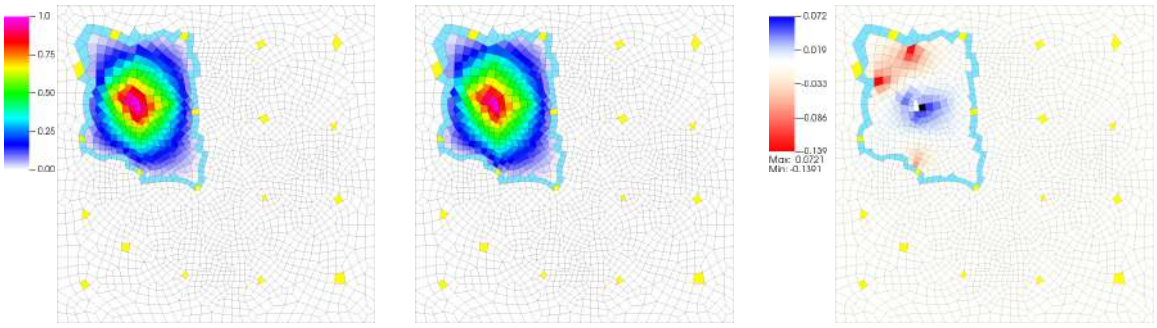

(a) Basis function calculated exclusively on the support region.

(b) Basis function calculated on the extended support region.

(c) Difference between the basis function calculated on the support region and the extended support region.

Source: (SOUZA et al., 2022).

4.2.5 Algebraic Multiscale Solver Prolongation Operator and Correction Functions

Once $\underline{P}_{en}^{cor}$ is properly defined, we can redefine equation (4.24) to find the corrected Prolongation Operator $\underline{P}_{op}^{cor}$ for the AMS-U as:

$$\underline{P}_{op}^{cor} = \begin{bmatrix} 0 & 0 & -\widetilde{A}_{ii}^{-1}(\widetilde{A}_{ie}\underline{P}_{en}^{cor} + \widetilde{A}_{in}) \\ 0 & 0 & \underline{P}_{en}^{cor} \\ 0 & 0 & I_{nn} \end{bmatrix} \tag{4.47}$$

Lastly, we need to define a modified correction function $\underline{C}^{cor}$ taking into account the modifications to compute $\underline{P}_{op}^{cor}$. By assuming that $\underline{P}_{en}^{cor}$ and $\widetilde{A}_{en}$ are known, we substitute them in Equation (4.43) to find a suitable approximation for M_{ee}^{-1}, thus:

$$\underline{P}_{en}^{cor} = -(M_{ee}^{\text{cor}})^{-1}\widetilde{A}_{en} \tag{4.48}$$

By isolating $(M_{ee}^{\text{cor}})^{-1}$, we have:

$$\mathcal{M}_{ee}^{-1} = -\underline{P}_{en}^{cor}/\widetilde{A}_{en} \tag{4.49}$$

where equation (4.43) is now redefined as:

$$\underline{C}^{cor} = \begin{bmatrix} \widetilde{A}_{ii}^{-1} & -\widetilde{A}_{ii}^{-1}\widetilde{A}_{se}\mathcal{M}_{ee}^{-1} & 0 \\ 0 & (M_{ee}^{\text{cor}})^{-1} & 0 \\ 0 & 0 & 0 \end{bmatrix} \tag{4.50}$$

4.2.6 Multiscale Iterative Procedures

The iterative procedure used to converge the AMS-U pressure field to the fine-scale reference solution within a given tolerance is a variation of the iterative scheme used by several authors (MOYNER; LIE, 2015; ŢENE; KOBAISI; HAJIBEYGI, 2016; BOSMA et al., 2017). In this scheme, successive multiscale and smoothing steps are employed to reduce the error to the desired tolerance, as described in algorithm 1. Note that the second step uses the ILU(0) decomposition (SAAD, 2003) of M_f and the biconjugate gradient stabilised method (BiCGSTAB) (VORST, 1992) to approximate the smoothing operator M_s^{-1}.

Algorithm 1: Multiscale Iterative Procedure

Input: M_f, Q_f, p_{ms}, $\underline{P}_{op}$ and $\underline{R}_{op}$

Output: iterative pressure solution, p_{it}.

$p^n \leftarrow p_{ms}$

$r^n \leftarrow Q_f - M_f p^n$

do

$\delta p^{n+1/2} \leftarrow \underline{P}_{op}(\underline{R}_{op} M_f \underline{P}_{op})^{-1} \underline{R}_{op} r^n$

$r^{n+1/2} \leftarrow r^n - M_f \delta p^{n+1/2}$

$\delta p^{n+2/2} \leftarrow M_s^{-1} r^{n+1/2}$

$p^{n+1} \leftarrow \delta p^{n+1/2} + \delta p^{n+2/2}$

$r^n \leftarrow Q_f - M_f p^{n+1}$

$p^n \leftarrow p^{n+1}$

while $r^n < \epsilon$

5 RESULTS

In this chapter we present the results of the formulations described in the previous chapters. To this end, we use these numerical methods to simulate several benchmark problems from the literature adapted to the context of unstructured grids. Both of these formulations were coded using an in-house preprocessor and simulators using Matlab R2020b.

5.1 Flux Limited Splitting

In the first section, we present the results of flux limmited splitting coupled with MPFA-D for simulating single-phase flows in highly heterogeneous and anistropic media. Before continuing, it is worth remembering the notation used for the FLS initialization parameters. First, tol_1 and tol_2 represent the tolerance of a cycle and for the DMP test as described on the Flowchart 2, lim_{WS} is the number of iterations required to start the limiting procedure and tol_3 is the tolerance of the final solver in Flowchart 1.

5.1.1 Fluid flow in a domain with a square hole in an heterogeneous and extremely anisotropic medium

This first example was originally devised by Queiroz et al. (2013) to study the loss of monotonicity in CVD-MPFA schemes. In this problem, the analysed domain is in the form of a square $\Omega = [0,1]^2$ with a concentric opening that is also in the form of a square $\Omega = [4/9, 5/9]^2$. Dirichlet boundary conditions are applied to the boundaries of the domain, with the outer boundaries set as $g_D^1 = 0$ at $\partial\Omega_1$ and the inner boundaries set as $g_D^2 = 2$ at $\partial\Omega_2$. The diffusion tensor is strongly anisotropic and discontinuous, as given by:

$$K(x,y) = \begin{cases} \begin{bmatrix} \cos(\pi/2) & -\sin(\pi/2) \\ sin(\pi/2) & cos(\pi/2) \end{bmatrix} \begin{bmatrix} 100 & 0 \\ 0 & 0.01 \end{bmatrix} \begin{bmatrix} \cos(\pi/2) & \sin(\pi/2) \\ -sin(\pi/2) & cos(\pi/2) \end{bmatrix} & K_1 : x \leq 0.5 \\ \begin{bmatrix} (y+\epsilon)^2 + \delta(x+\epsilon)^2 & -(1-\delta)(y+\epsilon)(x+\epsilon) \\ -(1-\delta)(y+\epsilon)(x+\epsilon) & (x+\epsilon)^2 + \delta(y+\epsilon)^2 \end{bmatrix} & K_2 : x > 0.5 \end{cases} \tag{5.1}$$

with $\epsilon = 10^{-3}$.

The physical domain is discretised with three different unstructured grids. The first is a coarser grid with 1,280 quadrilateral slightly distorted elements, the second is a medium-fine grid with 2,678 uniform isotropic triangular elements and the last is an extremely fine grid with 10,712 triangular elements. For comparison, we ran

Table 1 – Initialization parameters for the fluid flow in a domain with a square hole in an heterogeneous and extremely anisotropic medium example

Initialization Parameters	tol_1	tol_2	tol_3	lim_{WS}	# CVs
Coarse grid with quadrilateral CVs	5.00E-04	5.00E-04	1.00E-12	3	1,280
Intermediate grid with triangular CVs	5.00E-04	5.00E-04	1.00E-12	3	2,678
Refined grid with triangular CVs	5.00E-04	5.00E-04	1.00E-12	3	10,712

Source: Author.

a simulation for each of these grids with four different schemes, the Flux Limited Splitting, the MPFA-D, a positive-preserving monotone nonlinear TPFA (CONTRERAS, 2017) and the standard linear TPFA. The initializations parameter for the FLS algorithm can be found at table 1.

On the first grid analysed, the coarser grid, one can already see the advantages of the Flux Limited Splitting in comparison to the other methods. See Figure 15. While the MPFA-D had qualitatively a good solution, the method produced a strong undershoot and a small overshoot as shown in Table 2. The TPFA solution produced a result that is consistent with the Discrete Maximum Principle, but is quite diffuse and does not represent the physics of the problem. The pressure field of the nonlinear TPFA complied with the DMP as expected, without the large amounts of diffusion that occur in the linear TPFA. This pattern of linear TPFA is observed throughout all the examples in this work. The Flux Limited Splitting solution, in turn, fixes the overshoot and undershoot problems of the MPFA-D solution. It is possible to see the similarity between the NL-TPFA and the FLS solution, despite two main differences. The first main difference is the discontinuity on the left side of the inner boundary. While the MPFA-D, the NL-TPFA and the linear TPFA produce solutions with a smooth pressure distribution, the FLS solution produces an area of near zero pressure in this part of the region. The second difference is seen in the pressure distribution next to the upper right corner, where NL-TPFA produces a region resembling a channel with high permeability. This pattern could not be observed with the MPFA-D and Flux-Splitting solutions.

On the medium and finer grids we analysed, the FLS behaved similarly, using the triangular grids and despite of the huge undershoot of the MPFA-D solutions as shown in Figures 16 and 17 . For both grids, the approximation NL-TPFA has either not converged or converged to a solution violating the DMP even after several iterations. The zero pressure region next to the left inner boundary also appeared with the FLS solution in both grids.

It is also interesting to see how the Flux Limitation Algorithm influence the maximum and minimum pressure values for each iteration. In Figure 18 it can be seen that the FLS approaches the DMP as the method limits the cross diffusion terms. At the

Table 2 – Maximum pressure, $p_{max}$and minimum pressure, $p_{min}$for the fluid flow in a heterogenous domain with a square hole in a extremely anisotropic media example.

	TPFA		MPFA-D		FLS		Nonlinear TPFA	
	p_{min}	p_{max}	p_{min}	p_{max}	p_{min}	p_{max}	p_{min}	p_{max}
Coarse grid with quadrilateral CVs	0.005	1.837	-1.711E-01	2.039	6.810E-04	1.902	7.286E-07	1.927
Intermediate grid with triangular CVs	8.432E-05	1.985	-1.139	2.099	2.330E-06	1.977	2.871-12	2.151
Refined grid with triangular CVs	4.192E-05	1.986	0.324	2.214	1.228E-06	2.198	0.000	3.137

Source: Author.

beginning of the simulation, an increase in overshoot or undershoot can be observed. This is due to the warm start described in the flowchart given in Figure 3, which shifts the start of the limiting algorithm. On the intermediate grid and the refined grid, this drove the solution to move away from the bounding pressure values. The oscillating behaviour occurs every time the algorithm restarts the outer loop using the initial solution of the warm start. The idea behind this is that the FLS algorithm can detect and capture and limit different frequency errors in each loop. The FLS was able to produce a DMP-compliant solution despite the large number of iterations. In terms of computational cost, the FLS takes about 7 times more time than the a simulation with he MPFA-D, including preprocessing costs.

5.1.2 Fluid Flow in a Highly Anisotropic and Heterogeneous Reservoir

The next example was originally proposed by Yuan & Sheng (2008) to evaluate the loss of monotonicity in nonlinear positive preserving methods. The problem consists of a unitary quadratic domain $\Omega = [0,1]^2$ whose boundaries are subject to a prescribed pressure ($p = 0$), and into which a unitary source term is injected in a concentric square as defined by :

$$f(x,y) = \begin{cases} 1 & (x,y) \in \left[\frac{3}{8} \ \frac{5}{8}\right]^2; \\ 0, & (x,y) \notin \left[\frac{3}{8} \ \frac{5}{8}\right]^2 \end{cases} \tag{5.2}$$

The permeability field of the media is highly heterogeneous and anisotropic, defined as it follows:

$$\underline{K} = \begin{bmatrix} y^2 + \epsilon x^2 & -(1-\epsilon)xy \\ -(1-\epsilon)xy & \epsilon y^2 + x^2 \end{bmatrix}, \quad \epsilon = 5x10^{-2} \tag{5.3}$$

Figure 15 – Fluid flow in a domain with a square hole in an heterogeneous and extremely anisotropic medium using a coarse grid with 1,280 quadrilateral elements.

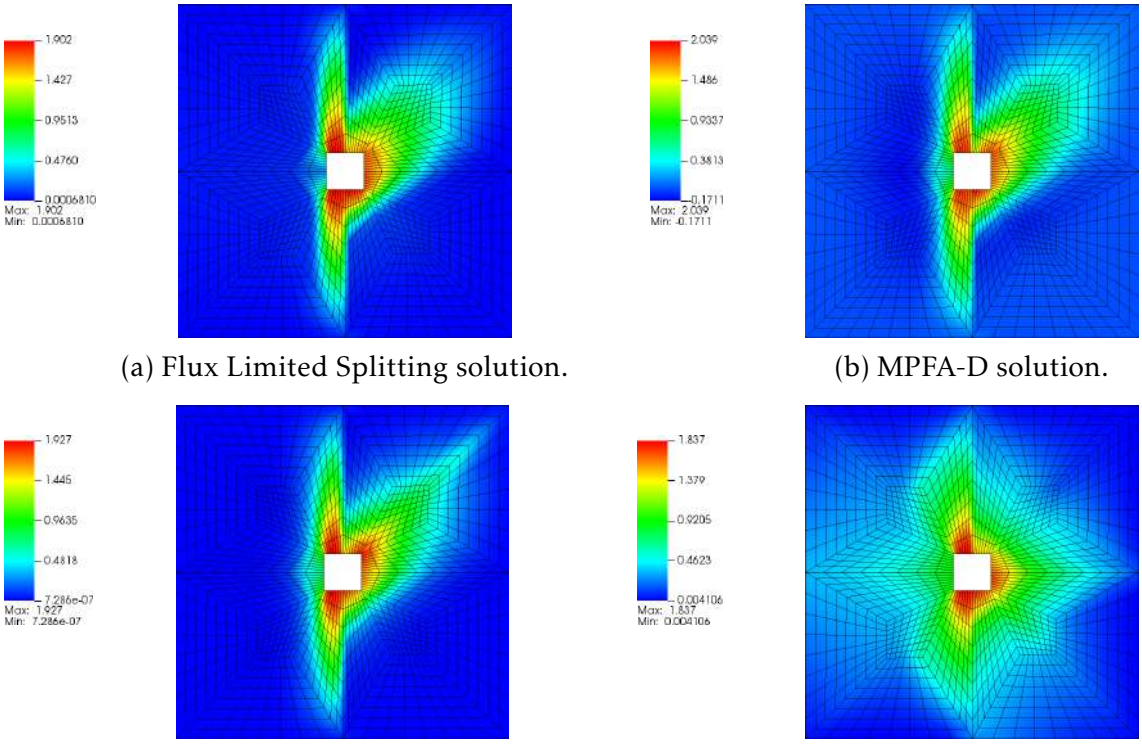

(a) Flux Limited Splitting solution.

(b) MPFA-D solution.

(c) Nonlinear TPFA converged with 36 iterations.

(d) TPFA solution.

Source: Author

Table 3 – Initialization parameter for the fluid flow in a highly anisotropic and heterogeneous reservoir example.

Initialization Parameters	tol_1	tol_2	tol_3	lim_{WS}	# CVs
Structured Grid	5.00E-04	5.00E-03	1.00E-12	4	1024
Distorted Grid	5.00E-04	5.00E-03	1.00E-12	4	1024
Unstructured Grid	1.00E-04	5.00E-04	1.00E-12	4	4791

Source: Author.

In this example, the physical domain is also discretised for comparison purposes by using three different configurations of quadrilateral grids. The first grid consists of a structured grid with 1,024 elements Yuan & Sheng (2008), the second grid is obtained by randomly distorting the elements of the first grid, and the last is an unstructured grid with 4,791 elements. Again, the results are compared using the Flux Limited Splitting technique, the MPFA-D, a nonlinear TPFA (CONTRERAS et al., 2021) and the standard linear TPFA are compared. The initializations parameter for the FLS algorithm can be found at table 3.

First of all, it is important to note that, in contrast to the previous example,

Figure 16 – Fluid flow in a domain with a square hole in an heterogeneous and extremely anisotropic medium using an intermediate grid with 2,678 triangular elements.

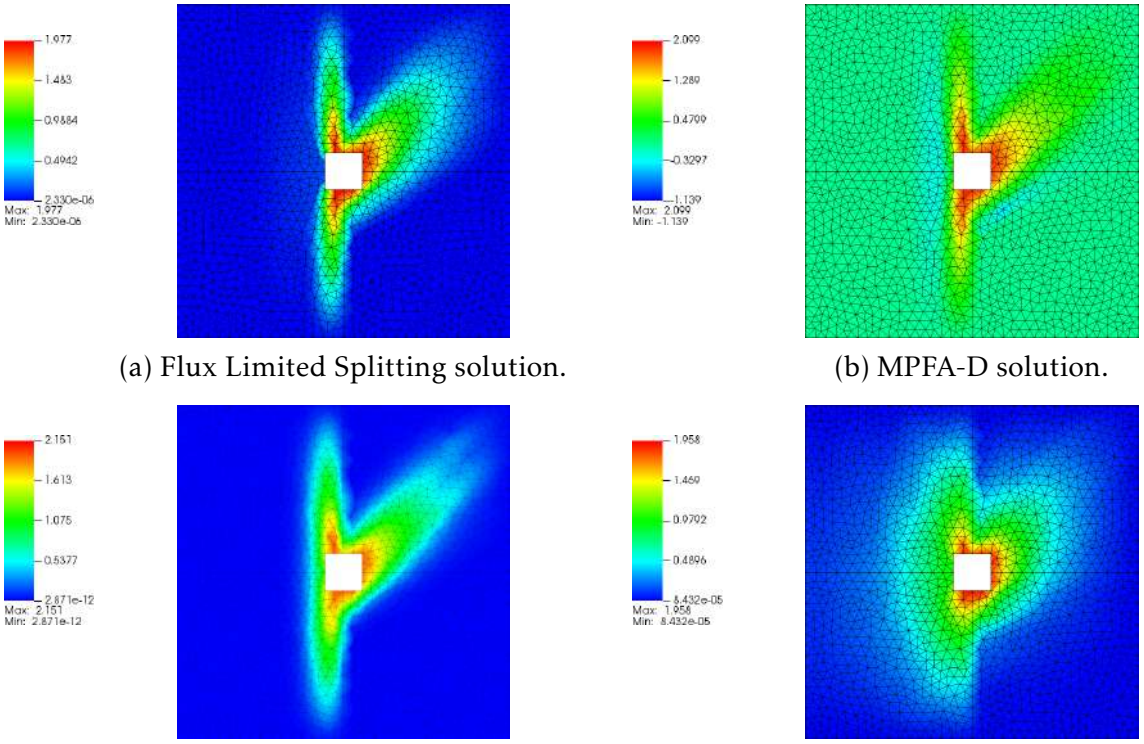

(a) Flux Limited Splitting solution.

(b) MPFA-D solution.

(c) Nonlinear TPFA failed to converge: Pressure solution with 2,000 iterations.

(d) TPFA solution.

Source: Author

all methods are qualitatively quite close to each other, the exception of the linear TPFA, which once again produced a DMP-satisfying, non-physical solution, with a large amount of diffusion. On the three grids used for this example, the MPFA-D proved to be robust, as all solutions were quite close to NL-TPFA and FLS, despite a minor undershooting. See Table 4. On the first grid analysed, the structured grid on Figure 19, the MPFA-D and FLS solution are qualitatively almost identical. In turn, the NL-TPFA appears to have produced a slightly more elongated pressure distribution with less diffusion. While the maximum and minimum pressure values of MPFA-D and FLS remained very close, with the FLS compensating for the loss of positivity of the MPFA-D solution, the spread between these values on NL-TPFA is considerably larger. On the distorted mesh in Figure 20, contrary to expectation, the perturbations actually helped the MPFA-D solution perform better and reduce undershoot. In turn, the FLS solution and the solutions from NL-TPFA repeated the pattern observed on the structured grid with similar solutions. Finally, on the third and finer grid, shown in Figure 21, the pattern seen on the other two grids seems to be reinforced. The NL-TPFA solution appears more stretched and with a larger difference between the maximum

Figure 17 – Fluid flow in a domain with a square hole in an heterogeneous and extremely anisotropic medium using a more refined grid with 10,712 triangular elements.

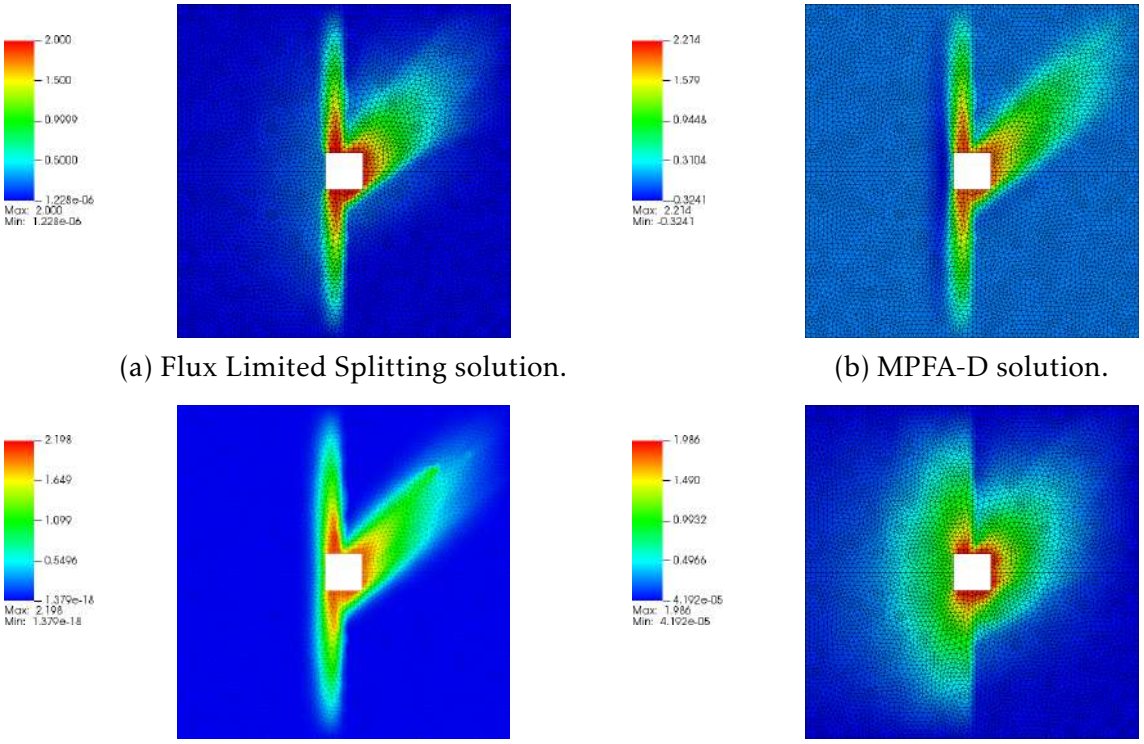

(a) Flux Limited Splitting solution.

(b) MPFA-D solution.

(c) Nonlinear TPFA converged wit 111 iterations.

(d) TPFA solution.

Source: Author

Table 4 – Maximum $p_{max}$and minimum p_{min}pressure for the fluid flow in a highly anisotropic and heterogeneous reservoir example.

	TPFA		MPFA-D		FLS		Nonlinear TPFA	
	p_{min}	p_{max}	p_{min}	p_{max}	p_{min}	p_{max}	p_{min}	p_{max}
Structured grid	0.001	1.147	-1.033E-04	1.638	1.065E-05	1.601	8.919E-12	1.863
Distorted grid	4.908E-04	1.189	-9.389E-05	1.665	7.125E-0.6	1.633	1.437E-19	1.854
Unstructured grid	4.473E-05	1.270	-2.776E-07	1.677	2.618E-06	1.636	4.714E-16	1.945

Source: Author.

and minimum pressures. Despite the differences in the meshes and the distortions, the FLS was able to repair the MPFA-D solution in all cases to ensure that it remained positive. The limiting algorithm described in Figure 22 shows that undershoot appears to appear towards the beginning of the iterative limiting procedure. With reasonable cost, the FLS was able to eliminate the spurious oscillations of the MPFA-D formulation. In terms of computational cost, the FLS took about 1 to 2 times more time than the MPFA-D counterpart, including pre-processing costs.

Figure 18 – Flux Limitation: Maximum and minimum pressure - $p_{\max}$and $p_{\min}$on the example fluid flow in a domain with a square hole in an heterogeneous and extremely anisotropic medium.

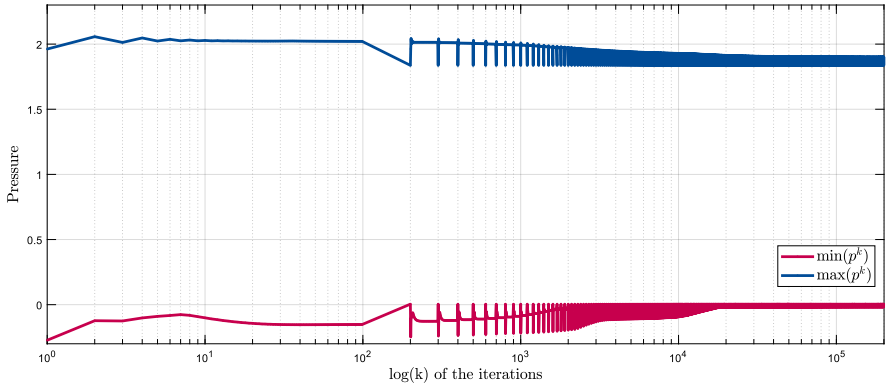

(a) Coarse Grid.

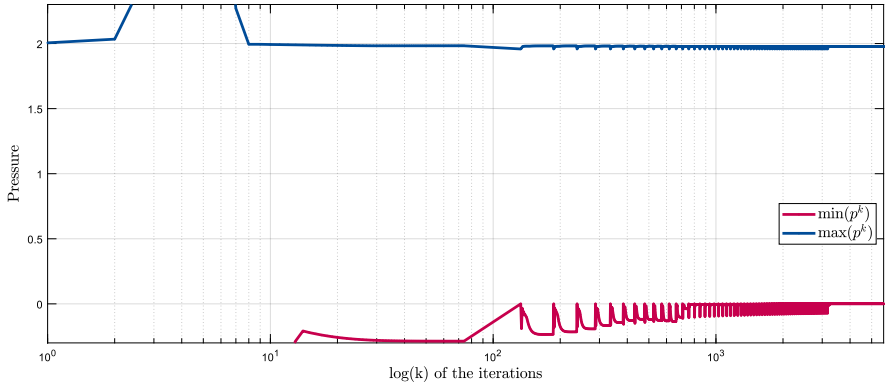

(b) Intermediate Grid.

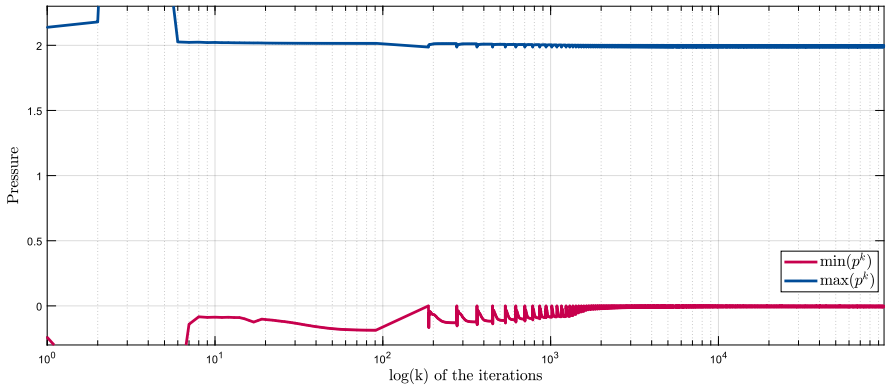

(c) Refined Grid.

Source: Author

5.1.3 Two Wells with an Anisotropic and Rotated Permeability Tensor

The third example is the simplest, but also the most difficult. It consists of a homogeneous and anisotropic medium in a uniform square domain $\Omega = [0,1]^2$ subjected to zero flux along its boundaries. The permeability tensor with an anisotropy ratio of 1.000 is rotated counterclockwise $3\pi/8$ as described in equation (5.4). This problem was proposed by (AAVATSMARK et al., 2008; TEREKHOV; MALLISON; TCHELEPI, 2017)

Figure 19 – Fluid flow in a highly anisotropic and heterogeneous reservoir using a structured grid with 1,024 quadrilateral elements.

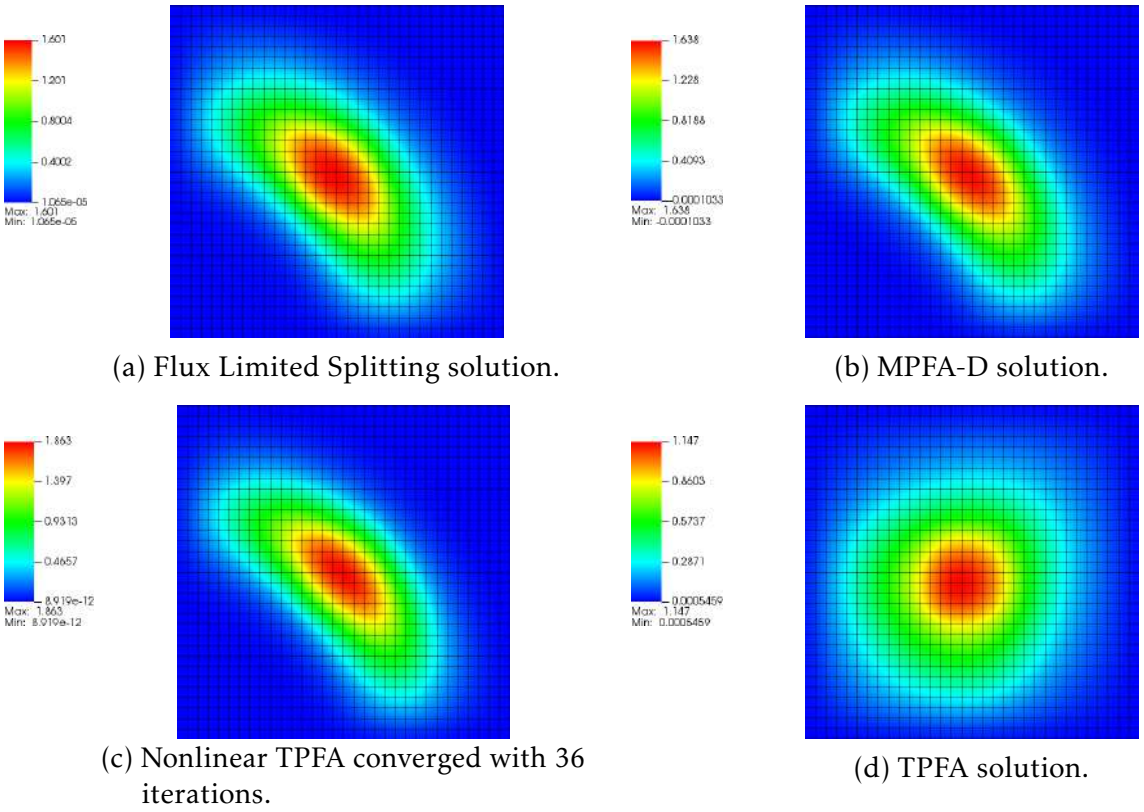

(a) Flux Limited Splitting solution.

(b) MPFA-D solution.

(c) Nonlinear TPFA converged with 36 iterations.

(d) TPFA solution.

Source: Author

to study the loss of monotonicity in cell-centred finite volume methods using an 11 x 11 structured grid. Originally, the two wells were placed in specific control volumes with prescribed pressure , $p_A = 0$, $p_B = 1$. To adapt it to the context of the unstructured grid, we use the two wells whose control volume centroids are closest to the centroids of the original control volumes, as shown in Figure 23.

$$K = \begin{bmatrix} \cos(3\pi/8) & -\sin(3\pi/8) \\ sin(3\pi/8) & cos(3\pi/8) \end{bmatrix} \begin{bmatrix} 1 & 0 \\ 0 & 10^3 \end{bmatrix} \begin{bmatrix} \cos(3\pi/8) & \sin(3\pi/8) \\ -sin(3\pi/8) & cos(3\pi/8) \end{bmatrix} \tag{5.4}$$

For the sake of comparison, we use four different grids in this problem. The first is the original grid (AAVATSMARK et al., 2008; TEREKHOV; MALLISON; TCHELEPI, 2017), an 11x11 structured grid, the second is a randomly distorted version of the first grid, we also use an intermediate unstructured grid with 5,156 triangular elements and the last grid used is a refined unstructured grid with 20,582 triangular elements. Again, for each of these grids we compare the solutions using the Flux Limited Splitting technique, the MPFA-D, a nonlinear TPFA (CONTRERAS et al., 2021) and the standard linear TPFA. The initializations parameter for the FLS algorithm can be found at table 5.

The first noticeable difference between this problem and the previous ones is

Figure 20 – Fluid flow in a highly anisotropic and heterogeneous reservoir using a distorted quadrilateral mesh with 1,024 elements.

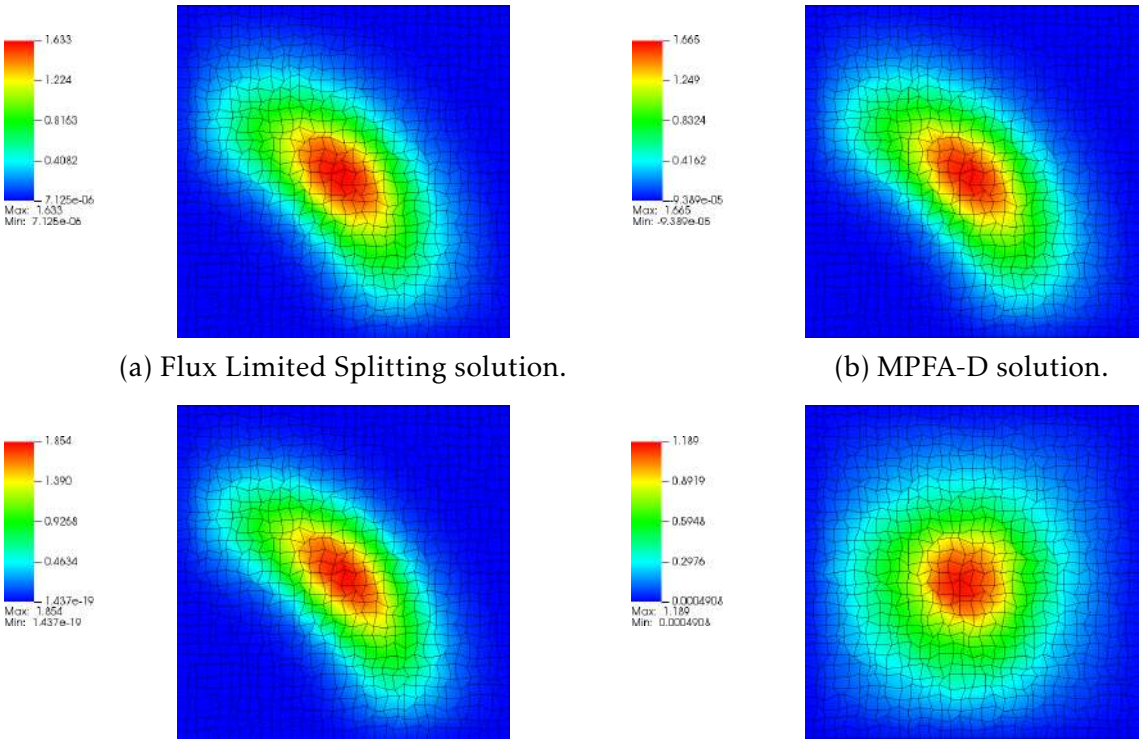

(a) Flux Limited Splitting solution.

(b) MPFA-D solution.

(c) Nonlinear TPFA converged with 42 iterations.

(d) TPFA solution.

Source: Author

Table 5 – Initialization parameter for the two wells with an anisotropic and rotated permeability tensor example.

Initialization Parameters	tol_1	tol_2	tol_3	lim_{WS}	# CVs
Structured Grid	1.00E-04	5.00E-05	1.00E-12	0	121
Distorted Grid	5.00E-05	5.00E-03	1.00E-12	4	121
Unstructured Grid	5.00E-04	5.00E-04	1.00E-12	1	5,156
Refined Unstructured Grids	5.00E-04	5.00E-04	1.00E-12	1	20,582

Source: Author.

the fact that each method produces a particularly different solution with some very distinguishable features. As expected, the linear TPFA solution satisfied the Discrete Maximum Principle, but with excess of artificial diffusion. In turn, the nonlinear TPFA solution performed qualitatively well on the structured and random distorted mesh in Figures 24 and 25, however, the method did not converge on the intermediate and refined triangular meshes on Figures 26 and 27, see Table 6. It is interesting to note that the NL-TPFA produced a solution complying with the DMP for the distorted mesh, but not for the structured grid mesh. The MPFA-D also struggles with the structured mesh with spurious oscillations, with the results being the worst with significant

Figure 21 – Fluid Flow in a Highly Anisotropic and Heterogeneous Reservoir using a refined quadrilateral mesh with 4,791 elements

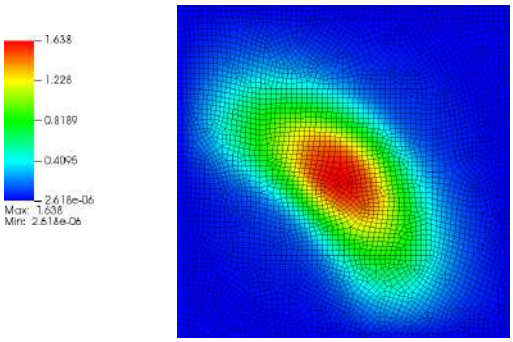

(a) Flux Limited Splitting solution.

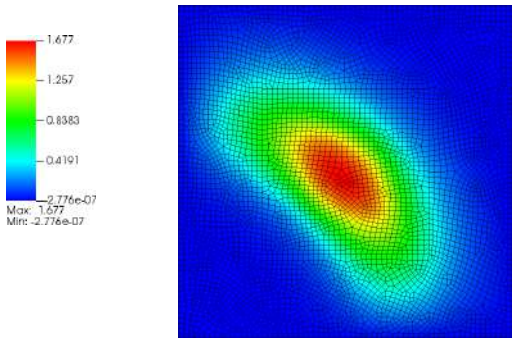

(b) MPFA-D solution.

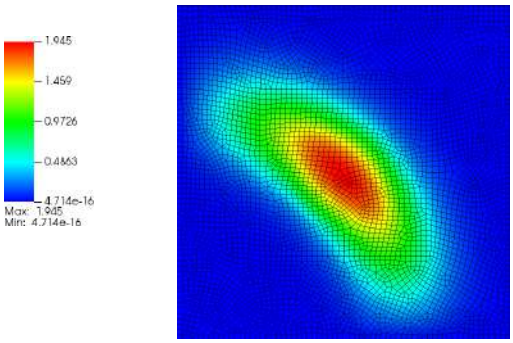

(c) Nonlinear TPFA converged with 47 iterations.

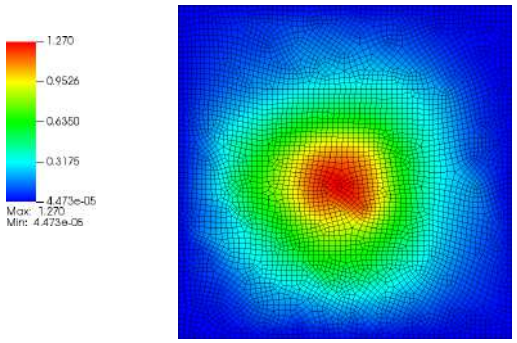

(d) TPFA solution.

Source: Author

overshoot and undershoot. Nonetheless, when the mesh was distorted and refined, these oscillations decreased. The FLS was by far the most coherent method. The FLS solutions produced a low and a high plateau, each with a peak and a valley bounded by the Dirichlet pressures. Once Again, the FLS was capable of repairing the MPFA-D solution by reintroducing the DMP. It is interesting to note that throughout limitation procedure showed in Figure 28, unlike the previous examples, the DMP was observed during all iterations, except for the intermediate grid, which showed undershooting in the first few iterations. Although there are no analytical solutions to this problem, the FLS produced results that are more coherent than the other attempted methods.

Figure 22 – Flux Limitation: Maximum and minimum pressure values - $p_{\max}$and $p_{\min}$on the example fluid flow in a highly anisotropic and heterogeneous reservoir.

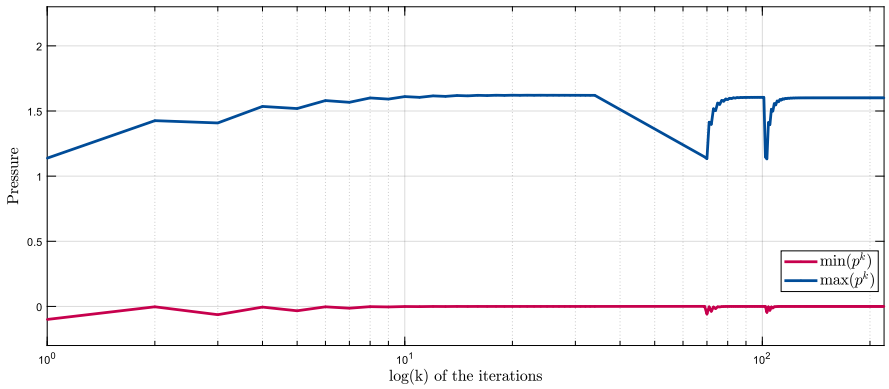

(a) Structured grid.

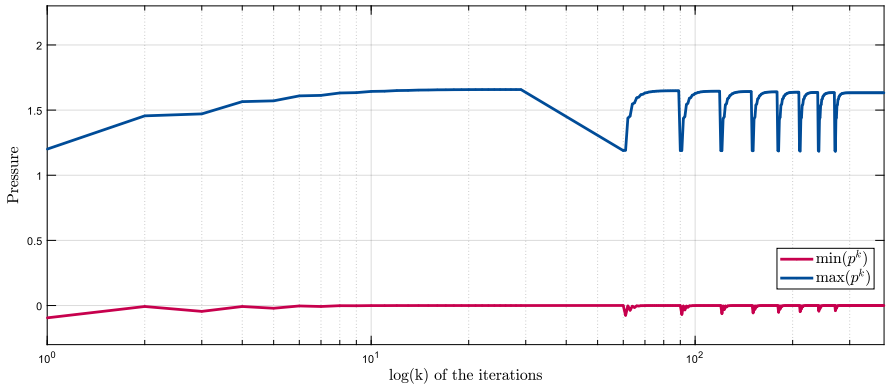

(b) Randomly distorted grid.

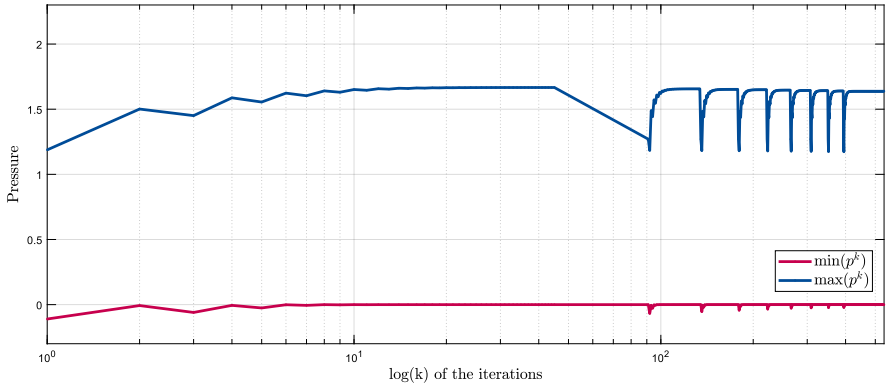

(c) Refined grid.

Source: Author

Figure 23 – Domain of the example: two wells with a anisotropic and rotated permeability tensor .

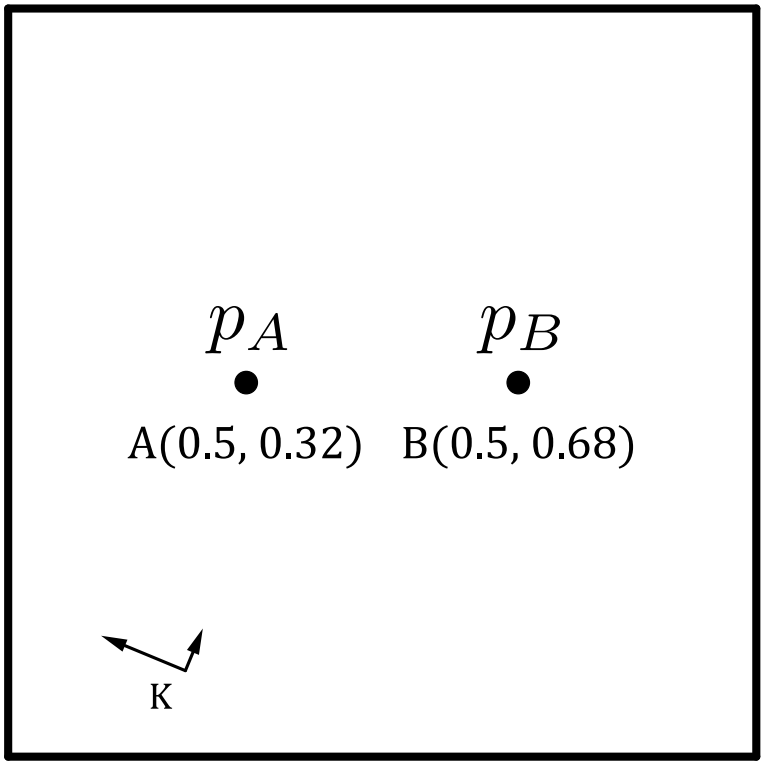

Source: Author

Table 6 – Maximum p_{max} and minimum p_{min} pressures for the two wells with an anisotropic and rotated permeability tensor example.

	TPFA		MPFA-D		FLS		Nonlinear TPFA	
	p_{min}	p_{max}	p_{min}	p_{max}	p_{min}	p_{max}	p_{min}	p_{max}
Structured Grid	0.000	1.000	-1.133E+00	2.133	0.000E+00	1.000	0.000E+00	1.642
Distorted Grid	0.000E+00	1.000	-9.137E-01	1.282	0.000E+00	1.000	0.000E+00	1.000
Unstructured Grid	0.000E+00	1.000	-2.508E-01	1.237	0.000E+00	1.000	Not converged	
Refined Unstructured Grid	0	1.000	-1.347E-01	1.030	0.000E+00	1.000	Not Converged	

Source: Author.

Figure 24 – Two wells with an anisotropic and rotated permeability tensor using a structured quadrilateral mesh with 11x11 elements.

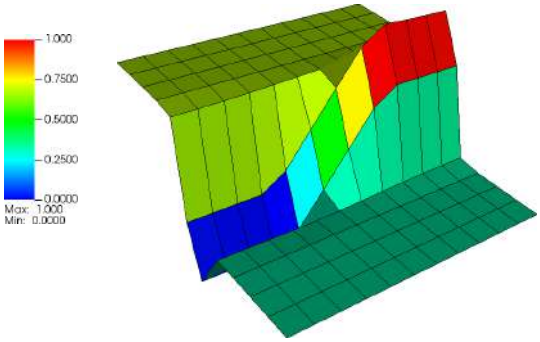

(a) Flux Limited Splitting solution.

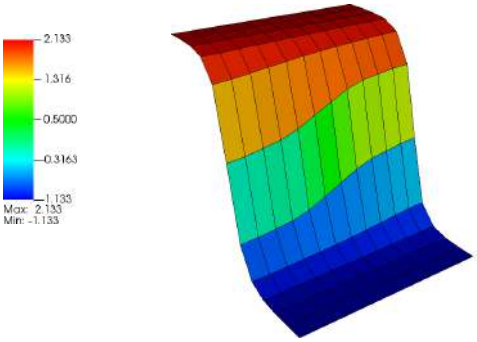

(b) MPFA-D solution.

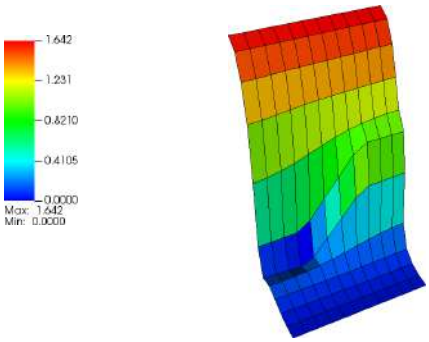

(c) Nonlinear TPFA converge with iterations.

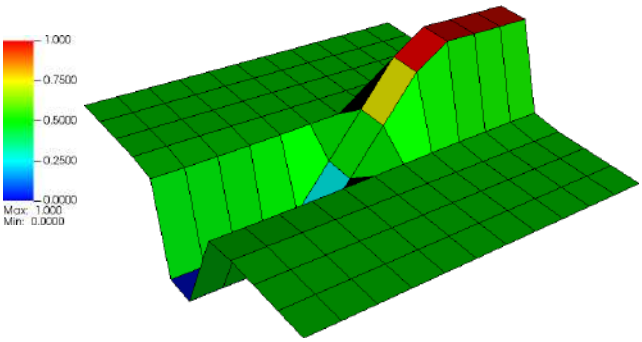

(d) TPFA solution.

Source: Author

Figure 25 – Two wells with an anisotropic and rotated permeability tensor using a randomly distorted quadrilateral mesh with 11x11 elements.

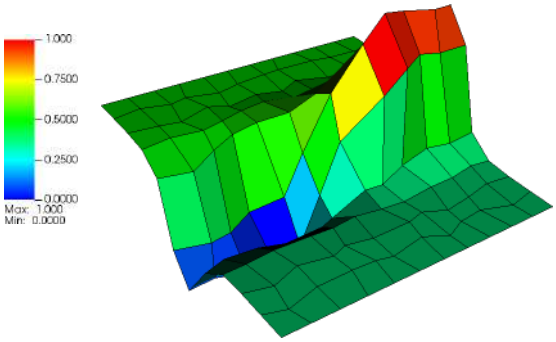

(a) Flux Limited Splitting solution.

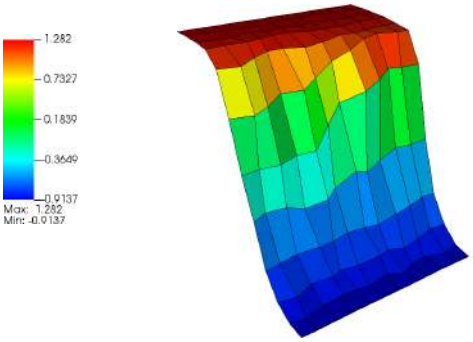

(b) MPFA-D solution.

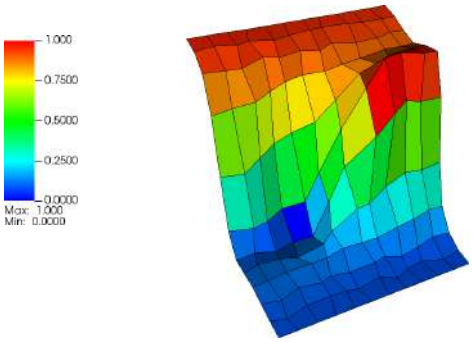

(c) Nonlinear TPFA converged with 192 iterations.

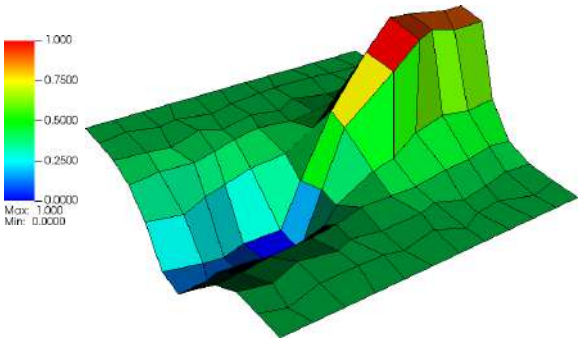

(d) TPFA solution.

Source: Author

Figure 26 – Two wells with an anisotropic and rotated permeability tensor using an intermediate unstructured mesh with 5,156 triangular elements.

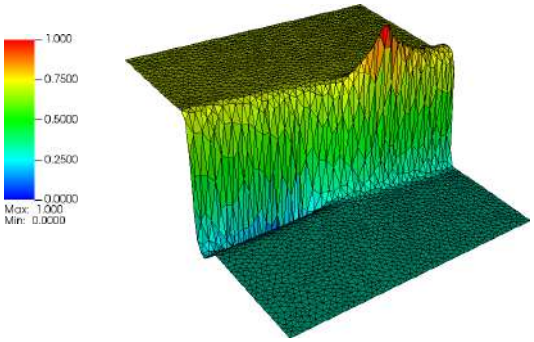

(a) Flux Limited Splitting solution.

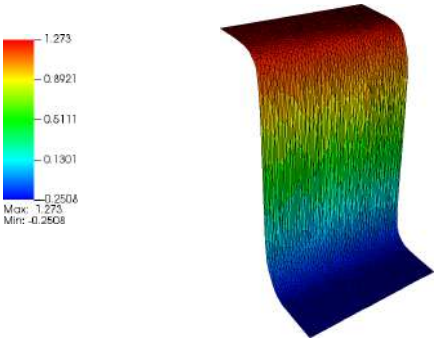

(b) MPFA-D solution.

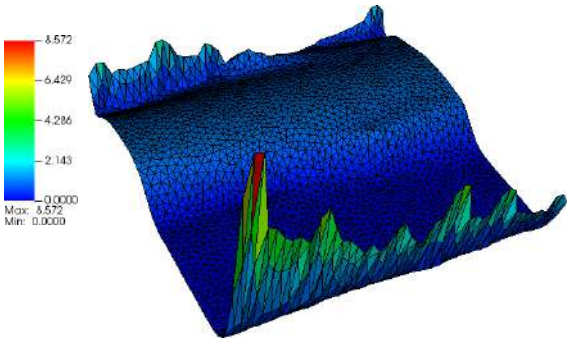

(c) Nonlinear TPFA diverged: Pressure solution after 1,000 iterations.

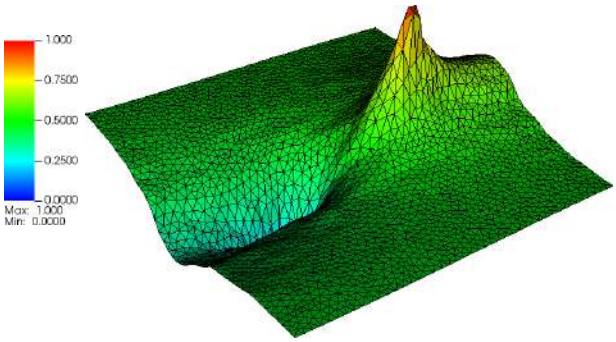

(d) TPFA solution.

Source: Author

Figure 27 – Two wells with an anisotropic and rotated permeability tensor using a refined unstructured mesh with 20,582 triangular elements.

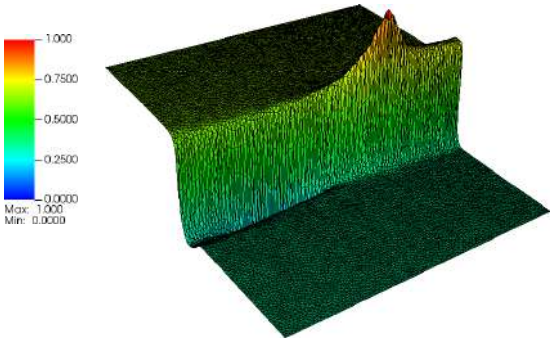

(a) Flux Limited Splitting solution.

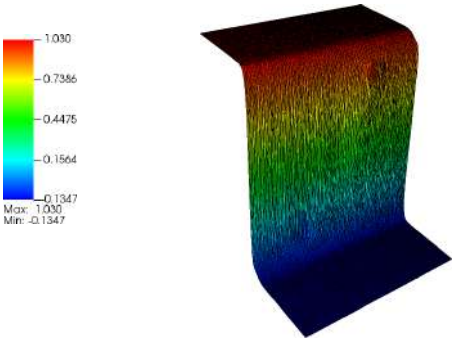

(b) MPFA-D solution.

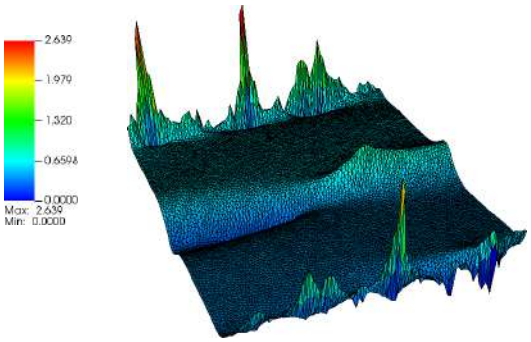

(c) Nonlinear TPFA diverged: Pressure solution after 1,000 iterations.

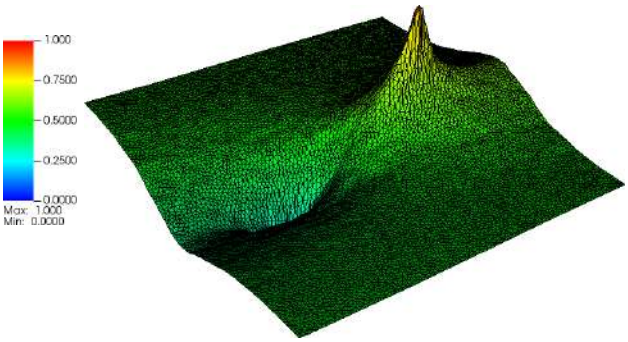

(d) TPFA solution.

Source: Author

Figure 28 – Flux Limitation: Maximum and minimum pressure $p_{\max}$and $p_{\min}$on the example two wells with a anisotropic and rotated permeability tensors.

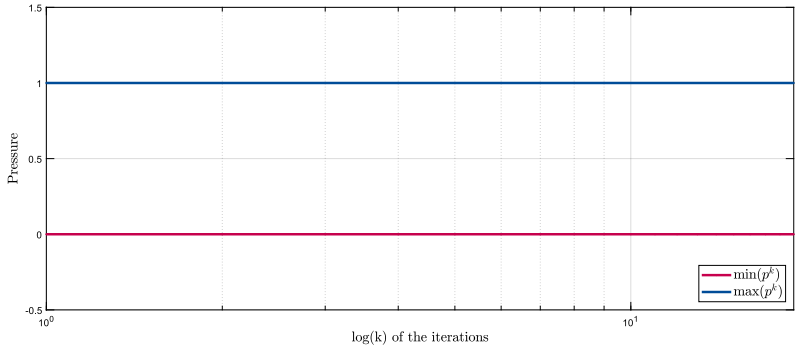

(a) Structured grid.

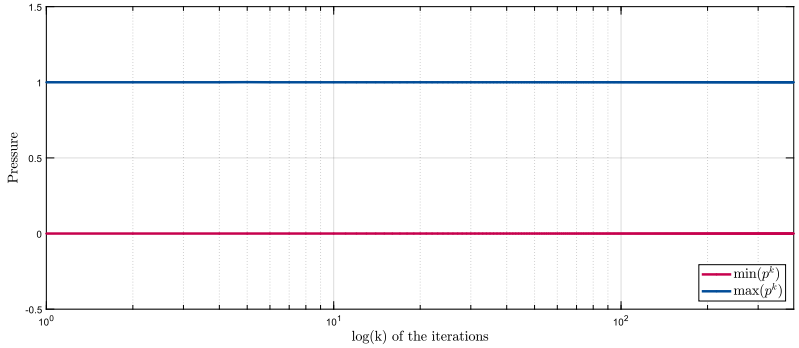

(b) Randomly distorted grid.

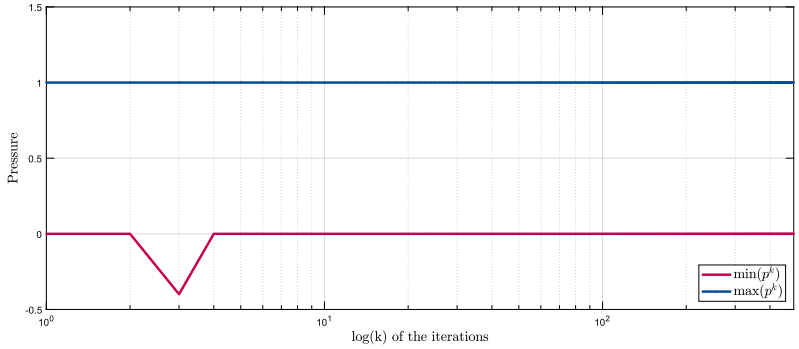

(c) Intermediate grid.

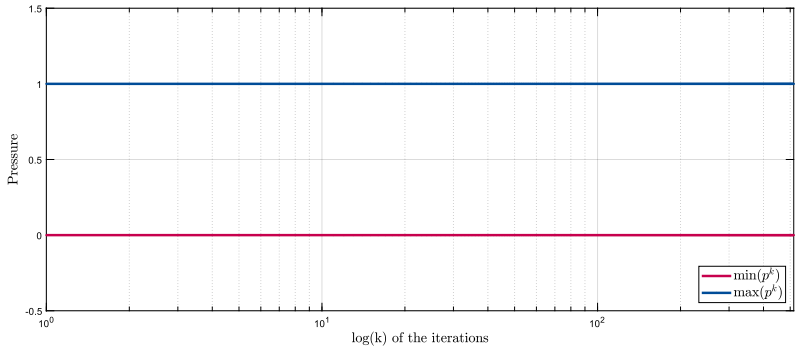

(d) Refined grid.

Source: Author

5.2 Algebraic Multiscale Solver for Unstructured Grids

In this second section, we present the results of the Algebraic Multiscale Solver for Unstructured Grids coupled with the MPFA-D for simulating single-phase and two-phase flow on highly heterogeneous and anistropic media.

5.2.1 Single-phase flow simulation in a fractured reservoir (Maltese cross)

In the first example of the AMS-U section, we simulate an incompressible single-phase flow subject to a quarter of five spot boundary condition. Here we use a unitary domain $\Omega = [0,1] \times [0,1]$ with zero normal flux conditions at the boundaries and prescribed flux ($Q_{inj} = 1$) and a prescribed pressure ($p_{\text{pro}} = 1$) in the injection well in the lower left corner and the production well in the upper right corner, respectively.

The permeability field shown in Figure 29a describes a homogeneous domain in red (K_1) with a fault in the form of a Maltese cross, developed to test the ability of AMS-U to handle this problem. We simulate flow with two different permeability field configurations, a channel (K_3) and a barrier (K_2). Two dual coarse meshes were created from two different background meshes: a simple structured 4x4 mesh that avoids the permeability contrast, and an unstructured mesh created specifically to fit the Maltese cross (see Figures 29b, 29c, and 29d). The simulations were performed on a fine-scale mesh with 2,276 quadrilateral elements. The permeability tensors used are given by:

$$\underline{K}_1 = \begin{bmatrix} 1 & 0 \\ 0 & 1 \end{bmatrix}, \quad \underline{K}_2 = \begin{bmatrix} \frac{1}{1{,}000} & 0 \\ 0 & \frac{1}{1{,}000} \end{bmatrix}, \quad \underline{K}_3 = \begin{bmatrix} 1{,}000 & 0 \\ 0 & 1{,}000 \end{bmatrix} \tag{5.5}$$

Figure 29 – Permeability field and multiscale entities used on the Example 5.2.1.

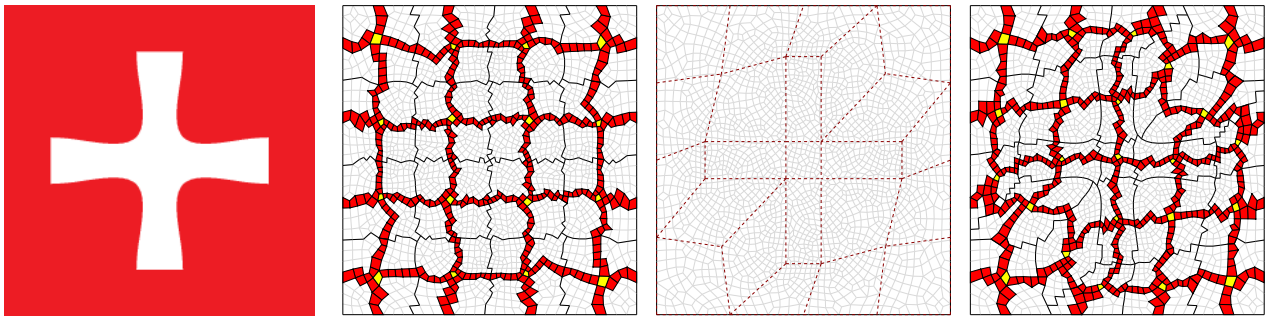

(a) Fault Permeability Field: Red K_1 White: K_2 and K_3.

(b) Primal and Dual Mesh created from a 4x4 background grid.

(c) Background grid capturing important features of the domain.

(d) Primal and Dual-grid created from the background grid given in Figure 29c.

Source: Author

The multiscale solution for the channel configuration shown in Figure 31 demonstrates that AMS-U is able to reproduce the underlying high-resolution physics of the

Table 7 – Table with the $\|p\|_2$ and $\|p\|_\infty$ errors of Example 5.2.1.

	4x4 Background Grid				**Unstructured Background Grid**			
	Channel		**Barrier**		**Channel**		**Barrier**	
Errors (%)	p_{it}	p_{ms}	p_{it}	p_{ms}	p_{it}	p_{ms}	p_{it}	p_{ms}
$\|p\|_2$	5.60E-3	9.832	0.159	7.063	8.000E-4	9.611	9.500 E-3	9.053
$\|p\|_\infty$	3.91E-2	1.082E+2	2.423	1.102E+2	1.01E-2	1.061E+2	1.217E-2	1.368E+2
Smoothing	143	-	44	-	55	-	44	-

Source: Author.

problem. For both the 4x4 background grid (see Figure 31b) and the unstructured background grid (see Figure 31c), the computed multiscale solution remains qualitatively very close to the converged solution. The errors presented in table 7 confirm this last claim. The error norm indicates that the multiscale solution remains very close to the fine-scale solution despite relatively high errors in L_∞. In this case, the L_2 and L_∞ norms of the errors were approximately 9.7% and 107%, respectively. Note that the 4x4 background grid produces only 2% higher L_∞ errors than the unstructured grid counterpart, while the difference in L_2 remains below 0.25 %. Nevertheless, the multiscale solution computed on the unstructured background grid converged with almost two-thirds fewer smoothing steps than the 4x4 background grid.

For the barrier configuration, a similar pattern emerges for multiscale errors with small errors in the L_2 norm and larger errors in the L_∞ norm. Again, the multiscale solution for both grids remains qualitatively very close to the fine-scale solution illustrated on Figure 30. This time, however, Table 7 has shown that the 4x4 background grid produces more accurate results with about 7% and 110% for the L_2 and L_∞ error norms, respectively. We note that smaller errors in the non-iterative multiscale solution do not lead to fewer iteration steps. In this case, 44 smoothing steps were sufficient to drop the L_2 below 0.01% for the unstructured background grid solution.

The non-iterative AMS-U solution is able to adequately reproduce the physics of the problem at a fine scale, despite some local errors. Moreover, a few smoothing steps were able to significantly reduce the multiscale errors, except for the simulation of a 4x4 background grid with one channel configuration.

5.2.2 Single-phase flow simulation in a reservoir with a strong permeability contrast

In the second example, we simulate an incompressible single-phase flow in a rectangular domain $\Omega = [0, 1.5] \times [0, 1]$. Concentric to the boundaries a diamond-shaped region with diagonals of 1.2 and 0.75, where the main diagonal lies on the $x$axis. While the upper and lower sides of the physical domain are subjected to zero normal flow conditions, the left and right boundaries are subjected to the prescribed pressure $p = 1$ and $p = 0$, respectively. Also, a concentric circle with radius ($R = 0.2$) is removed from

Figure 30 – Solution of the Example 5.2.1 under a barrier configuration.

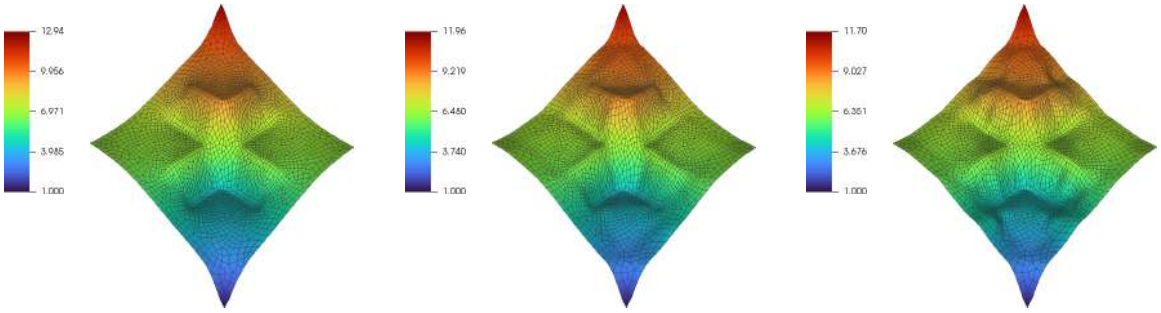

(a) Fine-scale solution.

(b) Multiscale solution using a 4x4 background grid.

(c) Multiscale solution using an unstructured background grid adapted to the permeability field.

Source: Author

Figure 31 – Pressure solution of the Example 5.2.1 under a channel configuration.

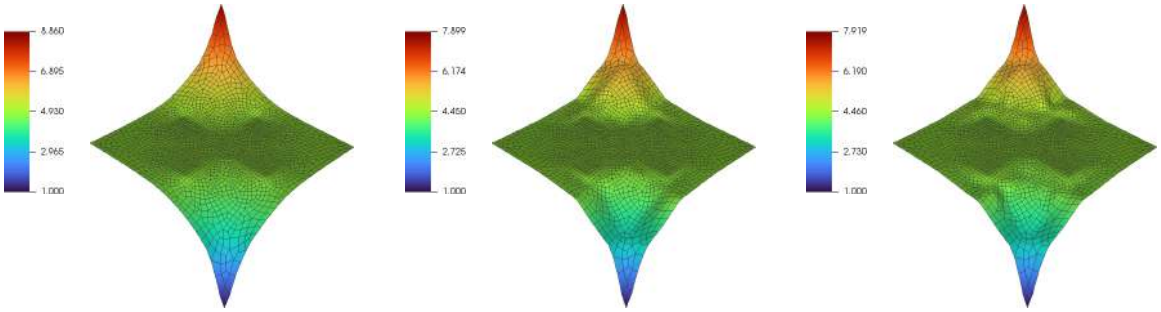

(a) Fine-scale solution.

(b) Multiscale solution using a 4x4 background grid.

(c) Multiscale solution using an unstructured background grid adapted to the permeability field.

Source: Author

the domain and this new boundaries are subjected to prescribed pressure ($p = 0.5$). The reservoir is depicted on Figure 32. Again, the example is simulated twice, with a channel (K_2) and a barrier (K_3) configuration for the diamond part of the domain, with (K_1) for the green part of the domain, as defined in equation (5.5).

The use of schemes capable of handling flexible meshes offers several advantages over formulations restricted to structured meshes. In particular, we highlight the ability to create an accurate model with complex wells and geologic structures such as sealing faults, channels, and oblique stratified layers (CARVALHO et al., 2005; CARVALHO; WILLMERSDORF; LYRA, 2007b). The AMS-U was devised to take full advantage of unstructured grids. The background grid strategy generates the primal and dual coarse meshes accordingly and provides a unified method for generating all

Figure 32 – Permeability field shaped as the Brazilian Flag: Green Rectangle K_1 (Sides: 1.5×1), Yellow Diamond: K_2 / K_3 (Diagonals: 1.2×0.75, check Equation 5.5) and Blue Circle ($R = 0.2$): Hole.

Source: Author

Table 8 – Table with the $\|p\|_2$ and $\|p\|_\infty$ errors of Example 5.2.2.

	Coarser Unstructured Background Grid 1				**Refined unstructured Background Grid 2**			
	Channel		**Barrier**		**Channel**		**Barrier**	
Errors (%)	p_{it}	p_{ms}	p_{it}	p_{ms}	p_{it}	p_{ms}	p_{it}	p_{ms}
$\|p\|_2$	7E-4	5.761	5.5E-3	4.375	1.6E-3	6.383	3.24 E-2	3.708
$\|p\|_\infty$	1.3E-3	15.826	1.29E-2	12.378	2.3E-3	15.982	5.83E-2	9.602
Smoothing	32	-	26	-	34	-	22	-

Source: Author.

multiscale entities. Therefore, the only requirement for the background grid procedure is a coarse background grid based solely on physical domain information. For the sake of comparison, in this example we use two unstructured background grids, as shown in Figure 33, with an underlying triangular fine-scale mesh with 9,252 elements.

In this example, for all proposed permeability fields, the AMS-U is able to accurately capture the physics at high resolution, as shown in Figures 34 and 35. Both the channel and barrier configurations presented solutions that are qualitatively similar to the converged solution. The measured errors presented in Table 8 corroborate this assertion. However, intrinsic oscillations at the boundaries of primal coarse volumes are imprinted on the multiscale solution. For the barrier configuration, the finer unstructured grid yields better solutions with L_2 and L_∞ norms of the errors of approximately 3.7% and 9.6%, respectively. The counterpart with the coarser background grid produced slightly higher errors of approximately 4.4% and 12.4%, using the L_2 and L_∞ norms, respectively. The errors for the channel configuration were slightly higher, with the coarser background grid being mildly more accurate than the refined unstructured

Figure 33 – Multiscale entities used on the Example 5.2.2.

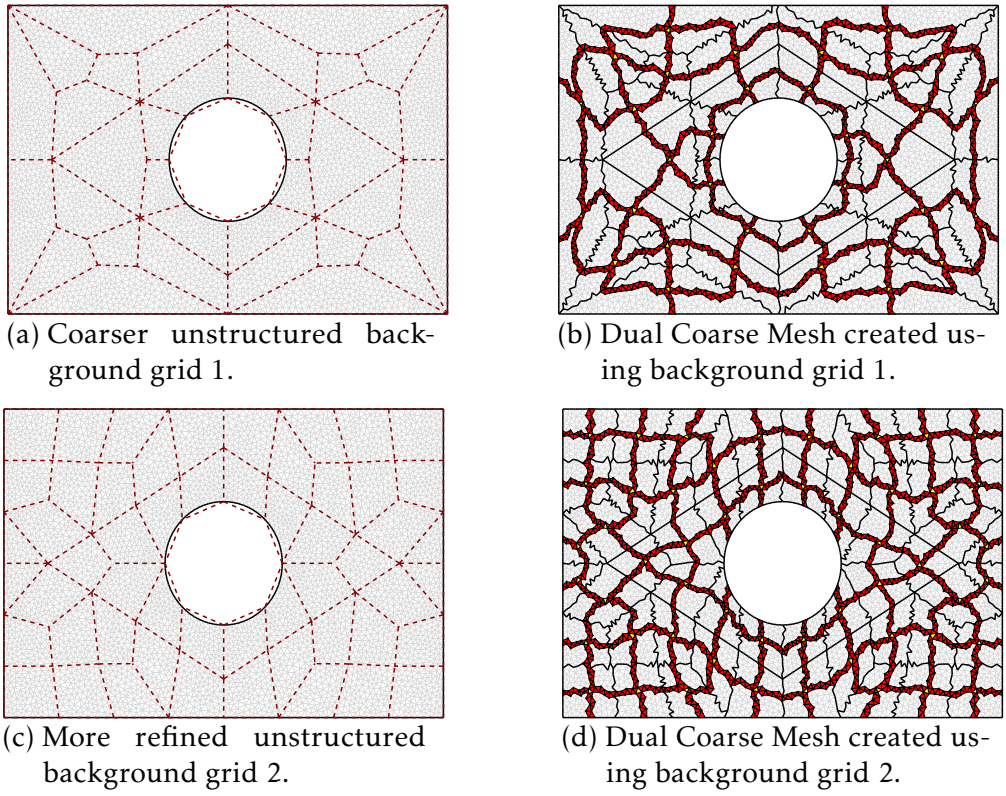

(a) Coarser unstructured background grid 1.

(b) Dual Coarse Mesh created using background grid 1.

(c) More refined unstructured background grid 2.

(d) Dual Coarse Mesh created using background grid 2.

Source: Author

grid with L_2 and L_∞ errors of about 5.8% and 15.8%, respectively. Possibly due to the good quality of the multiscale solution, the effects of the iterative smoothing stage were very effective. We attribute these small errors to two different factors. The first is the quality of the background grids generated and the resulting multiscale entities. While simulating the flow in a physical domain with a hole is a challenging task for formulations that rely on structured grids, the background grid strategy has no difficulty in satisfying all geometric requirements. The second aspect is the quality of the prolongation operator and the correction functions and their interaction in the construction of the multiscale solution. Figures 36 and 37 illustrate how the non-iterative multiscale solution is composed on the refined background grid. The low-resolution pressures projected onto the fine-scale system (see Figures 36b and 37b) are added to the correction functions (see Figures 36c and 37c), resulting in the multiscale solution (see Figures 36a and 37a). In the MPFA-D, the prescribed pressures on the nodes are part of the RHS of the discrete linear system. Since the boundary conditions are the same in both cases, the AMS-U correction functions remain identical. We note that the valleys in the projected coarse pressure solutions perfectly match the peaks of the correction function terms. Therefore, the AMS-U has no difficulty producing an overall good iterative and non-iterative multiscale solutions, despite the challenges of the physical domain.

Figure 34 – Pressure solution of the Example 5.2.2 under a barrier configuration.

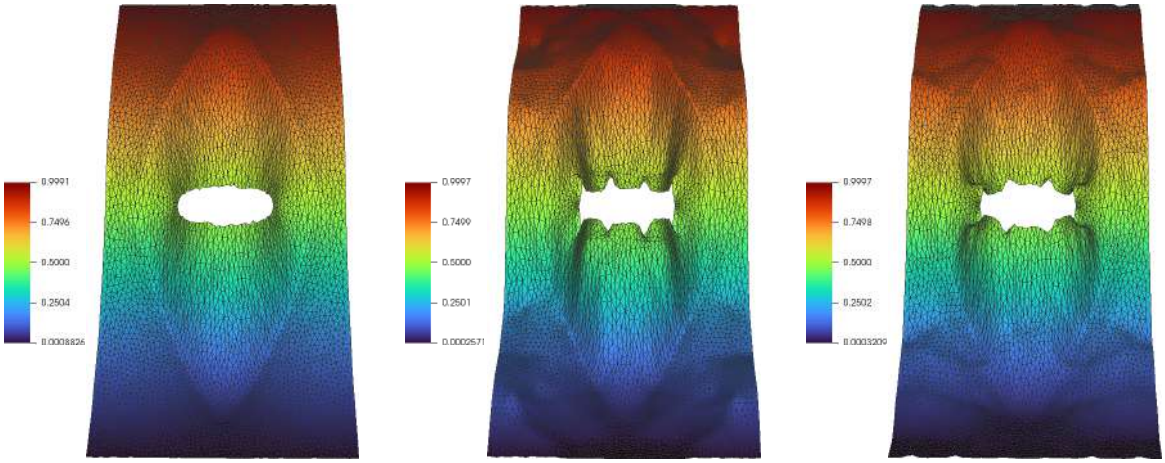

(a) Fine-scale solution.

(b) Coarser unstructured background grid 1.

(c) Refined unstructured background grid 2.

Source: Author

Figure 35 – Pressure solution of the Example 5.2.2 under a channel configuration.

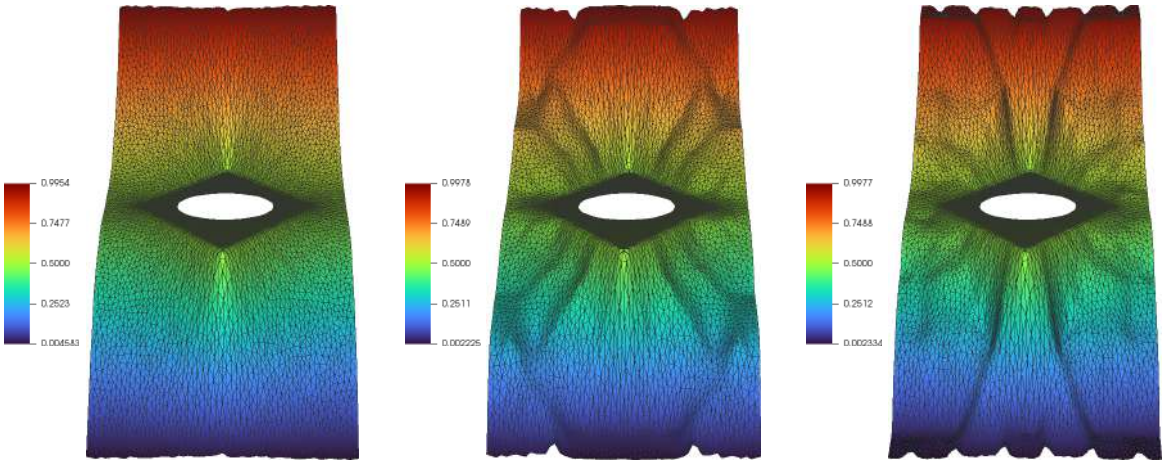

(a) Fine-scale solution.

(b) Coarser unstructured background grid 1.

(c) Refined unstructured background grid 2.

Source: Author

5.2.3 Single-phase flow simulation in a highly heterogeneous and anisotropic reservoir.

The following example was originally designed by Yuan & Sheng (2008) to compare their monotone non-linear finite-volume formulations, and for that we have already used it to test the FLS on section 5.1.2.

In the context of the multiscale methods, this example is used to evaluate the monotonicity of the AMS-U solution and compare it with the standard AMS. Both meth-

Figure 36 – Multiscale solution, multiscale solution without the corrections functions, and correction terms of the refined unstructured background grid 2 under a barrier configuration.

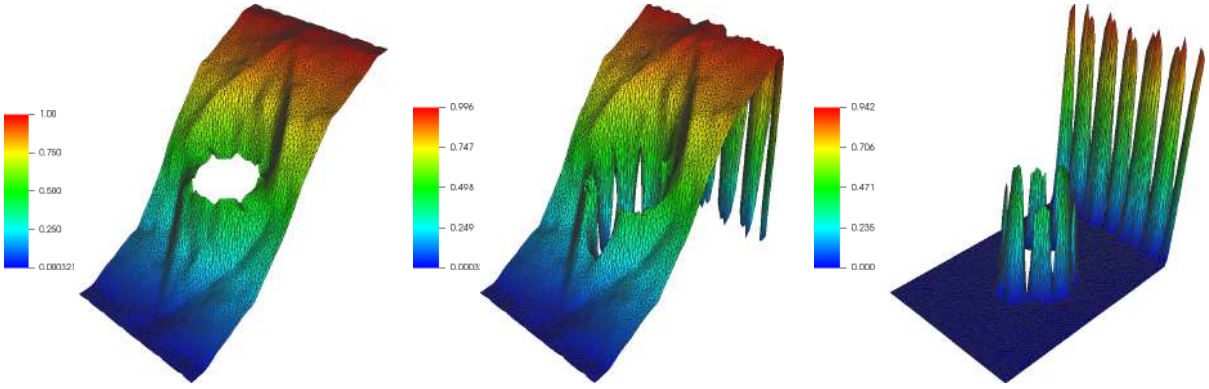

(a) p_{ms} (b) $\underline{P}_{op}p_c$ (c) $\underline{C}\widetilde{F}$

Source: Author

Figure 37 – Multiscale solution, solution without the corrections functions, and correction terms of the refined unstructured background grid 2 under a channel configuration.

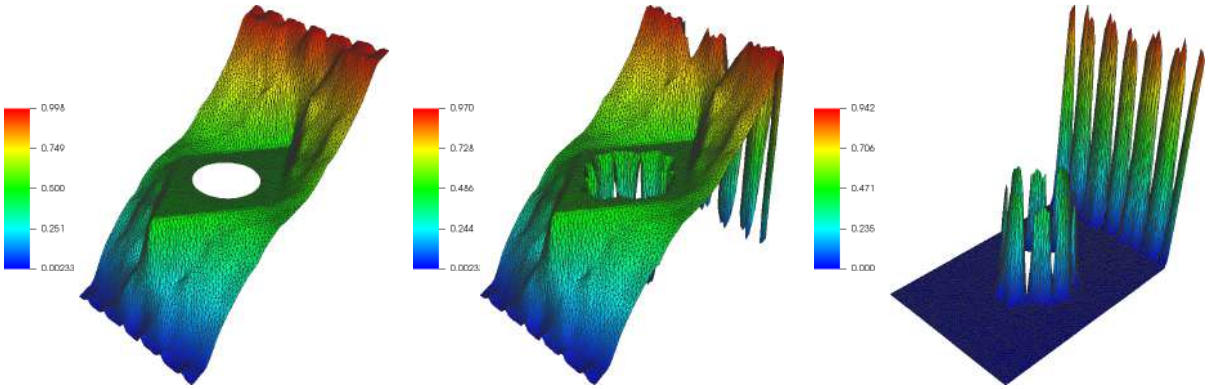

(a) p_{ms} (b) $\underline{P}_{op}p_c$ (c) $\underline{C}\widetilde{F}$

Source: Author

ods are applied to a 4x4 background grid and an unstructured adaptive background grid, as shown in Figure 39, using a fine-scale mesh comprised of 2,932 triangular elements. Although the analytical solution to this problem is not known, the solution is non-negative (PROTTER; WEINBERGER, 1984) according to the maximum principle.

Qualitatively, the noniterative AMS-U solution shown in Figures 40b and 40c is not as good as in the previous examples. It is clear that the AMS-U solution is not monotonic and also does not respect the DMP, since the two background grids chosen lead to undershoots (pink cells) in the multiscale solution. It is also possible to see overshoots (black cells) on the 4x4 background grid, where the spurious oscillations appear stronger on this grid.

However, the errors presented in Table 9 show that the AMS-U with an adequate grid strategy is able to achieve significantly better results compared to AMS with a non-adaptive grid. In all tests, AMS-U outperformed classical AMS, and the adaptive unstructured background grid outperformed a more standard 4x4 dual grid. When these strategies are combined, the L_2 and L_∞ norms of the multiscale errors are about 27.5% and 48.4%, respectively. In contrast, the worst configuration takes place when the standard AMS is used with the 4x4 grid. In this case, the errors exceed 1.000% on both the L_2 and L_∞ norms. We note that the analytic solution to this problem is unknown, but again the solution is non-negative (PROTTER; WEINBERGER, 1984) by the maximum principle.

However, even the fine-scale solution shown in Figure 40a produces negative pressures. A direct consequence of the loss of monotonicity due to the fine-scale flux approximation scheme used by the multiscale method is that it is not possible to guarantee the positivity of the basis functions nor DMP. Figures 41a and 41b illustrate the loss of monotonicity and the emergence of negative values in two-basis functions of the AMS-U.

While MPFA-D is known to significantly reduce problems with spurious oscillations in cases where earlier CVD-MPFA methods (using TPS) would struggle (SOUZA et al., 2020; CONTRERAS et al., 2016; GAO; WU, 2010), as a linear CVD-MPFA -scheme, it can still be subjected to eventual loss of monotonicity, depending on the problem. Furthermore, we know that regardless of the underlying fine-scale flux approximation, projecting the high-resolution system of equations onto the low-resolution grid using the multiscale operators produces a coarse-scale system with an MPFA-type approximation. Therefore, we attribute the loss of monotonicity of our multiscale method to these two key factors.

In conclusion, we note that no other multiscale method based on TPFA or CVD-MPFA without full pressure support can handle the simulation of this problem. The relatively good quality of the AMS-U solution allowed the iterative smoothing step to converge with few iterations. Even though the converged solution has some undesirable oscillations, the results are comparable to those computed with nonlinear schemes (YUAN; SHENG, 2008).

Table 9 – Table with the $||p||_2$ and $||p||_\infty$ errors of Example 5.2.3.

	4x4 Structured Background Grid				**Best Unstructured Background Grid**			
	AMS		**AMS-U**		**AMS**		**AMS-U**	
Errors (%)	p_{it}	p_{ms}	p_{it}	p_{ms}	p_{it}	p_{ms}	p_{it}	p_{ms}
$\|\|p\|\|_2$	5.8 E-3	1.063E3	2.273E-2	63.955	7 E-3	32.400	1.08E3	27.417
$\|\|p\|\|_\infty$	$2.65\text{x}10^{-2}$	$5.208\text{x}10^{3}$	0.2301	5.202E2	1.580 E-2	1.1723E2	1.81E-2	48.4624
Smoothing	41	-	24	-	28	-	24	-

Source: Author.

Figure 38 – Permeability representation of the highly heterogeneous and anisotropic reservoir of the Example 5.2.3.

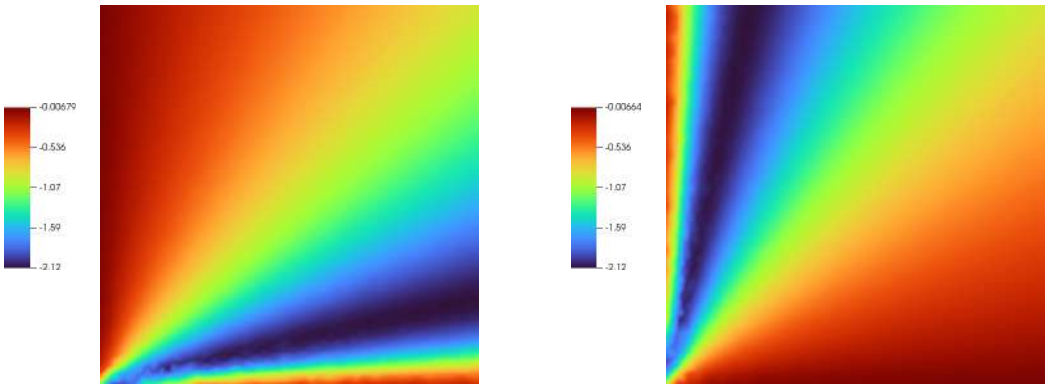

(a) kxx/kxy (b) kyy/kxy

Source: Author

Figure 39 – Multiscale entities used on the simulation of single-phase flow simulation on a highly heterogeneous and anisotropic reservoir.

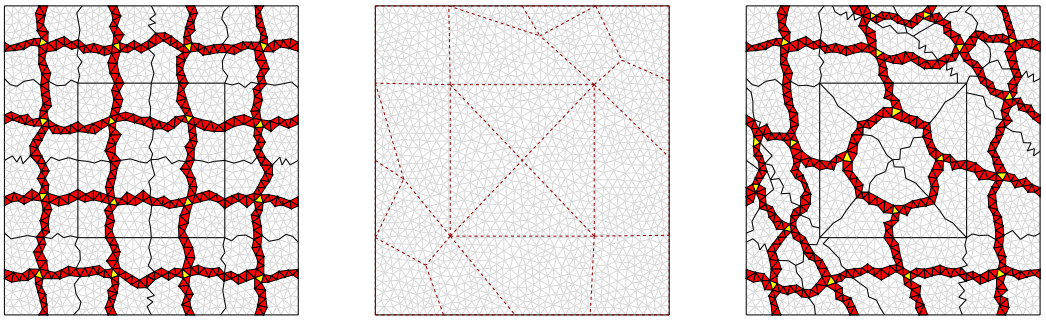

(a) Primal and dual mesh created from a 4x4 structured background grid.

(b) Unstructured background grid meshed in accordance with the physical domain.

(c) Primal and dual-grid created from the background grid in Figure 39b.

Source: Author

5.2.4 Two-phase flow in a heterogeneous reservoir with a discontinuous full tensor and high anisotropy ratios

In this example, we simulate water-oil flow in a heterogeneous reservoir with a discontinuous full tensor with high anisotropy ratio, proposed by Contreras et al. (2016) and tested by Souza et al. (2020) in the multiscale context. The reservoir consists of a unitary domain $\Omega = [0,1] \times [0,1]$ with 4 layer discontinuous anisotropic permeability tensors, each representing the same anisotropic tensor in different rotations, as shown in Figure 42 and Equation 42. The problem is simulated under 1/4 of five spot configuration with null normal flow conditions along its boundaries, $Q_{\text{inj}} = 1$ and $S_w = 1$ at

Figure 40 – Control volumes in which occur over and undershoots in black and pink, respectively, using the 4x4 structured background grid coarse mesh (40b) and the best background grid (40c).

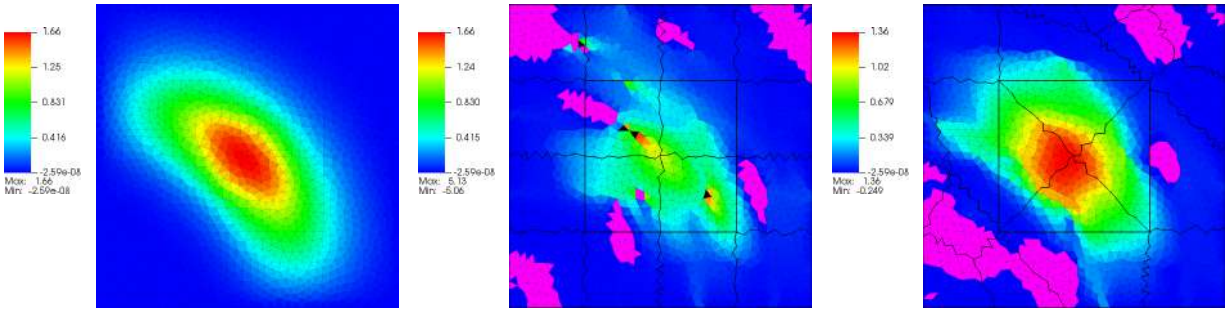

(a) Converged iterative solution.

(b) 4x4 structured background grid.

(c) Best unstructured background grid.

Source: Author

Figure 41 – Basis functions of the AMS-U used on Example 5.2.3: Overshooting and undershooting cells in black and pink, respectively.

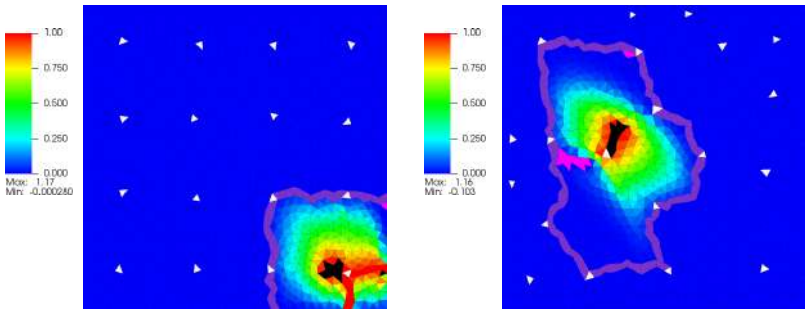

(a) 4x4 structured background grid.

(b) Best unstructured background grid.

Source: Author

the injection well in the lower left corner and the production well located at the upper right corner with prescribed pressure ($p_{\text{pro}} = 0$). The reservoir is initially fully saturated with oil ($\bar{S}_w^o = 0$).

$$\underline{K}_1 = \begin{bmatrix} 505 & 495 \\ 495 & 505 \end{bmatrix}, \quad \underline{K}_2 = \begin{bmatrix} 1,000 & 0 \\ 0 & 100 \end{bmatrix}, \quad \underline{K}_3 = \begin{bmatrix} 100 & 0 \\ 0 & 1,000 \end{bmatrix} \tag{5.6}$$

Originally, this example was used to evaluate the relative accuracy of the CVD-MPFA-D formulation compared to the standard TPFA (CONTRERAS et al., 2016). The effects of a highly anisotropic permeability field are poorly captured by the TPFA formulation on both unstructured and structured grids, making this example a benchmark case that demonstrates the advantages of a consistent MPFA formulation. High anisotropy ratios are a challenge for multiscale methods in the MsFV family in general (HAJIBEYGI et al., 2008; HAJIBEYGI; JENNY, 2009; BARBOSA et al., 2018; SOUZA et

Figure 42 – Permeability representations heterogeneous reservoir with a discontinuous full tensor with high anisotropy ratio (see Equation 42).

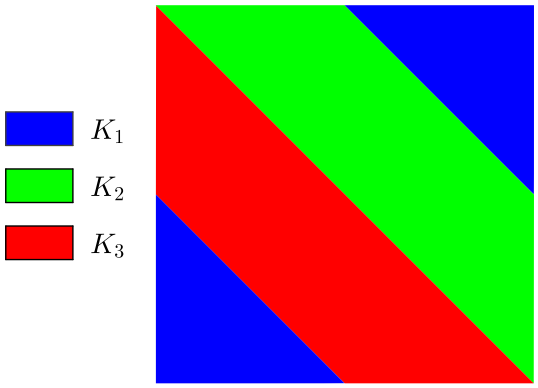

Source: Author

Figure 43 – Multiscale entities used to simulate oil and water flow in a heterogeneous reservoir with a discontinuous full tensor and high anisotropy ratio.

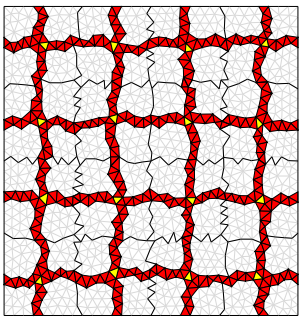

(a) Primal and Dual Mesh created from a 4x4 background grid: Mesh 1 with 2,328 triangular fine-scale elements.

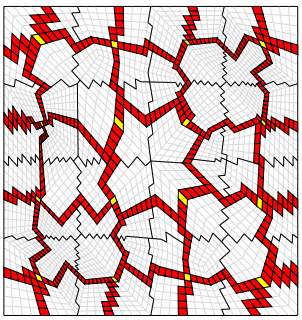

(b) Primal and Dual Mesh created from a 4x4 background grid: Mesh 2 with 2,496 quadrilateral fine-scale elements.

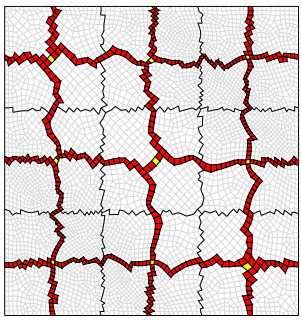

(c) Primal and Dual Mesh created from a 3x3 background grid: Mesh 3 with 4,890 quadrilateral fine-scale elements.

al., 2020; JENNY; LUNATI, 2009; HAJIBEYGI; JENNY, 2011b; JENNY; LEE; TCHELEPI, 2003; JENNY; LEE; TCHELEPI, 2006).

To evaluate the AMS-U formulation, the problem is simulated using three different fine-scale grids and the respective primal, dual, and background grids, as shown in Figure 43. In addition to the fine-scale solution using the MPFA-D, we also compare the AMS-U formulation with TPFA simulated on each grid. For the iterative procedure, the tolerance for the smoothing step is set to 10^{-6} for multiscale simulations.

First, a fine-scale unstructured grid with 2,328 triangular elements (see Figure 43a) is used. The primal and dual coarse grids were created based on a structured 4x4 background grid. For this grid, Figure 44 shows that the multiscale formulation of the AMS-U is able to qualitatively reproduce the most important aspects of the underlying high-resolution physics. For PVI=0.02 and PVI=0.07, the largest difference is seen as the saturation front appears more smeared. With time, the difference becomes less

Figure 44 – Oil and water flow in a heterogeneous reservoir with a discontinuous full tensor and high anisotropy ratios using mesh 1. a) to d) fine-scale solution using the MPFA-D; e) to h) fine scale solution using the TPFA method; i) to l) AMS-U + MPFA-D solution.

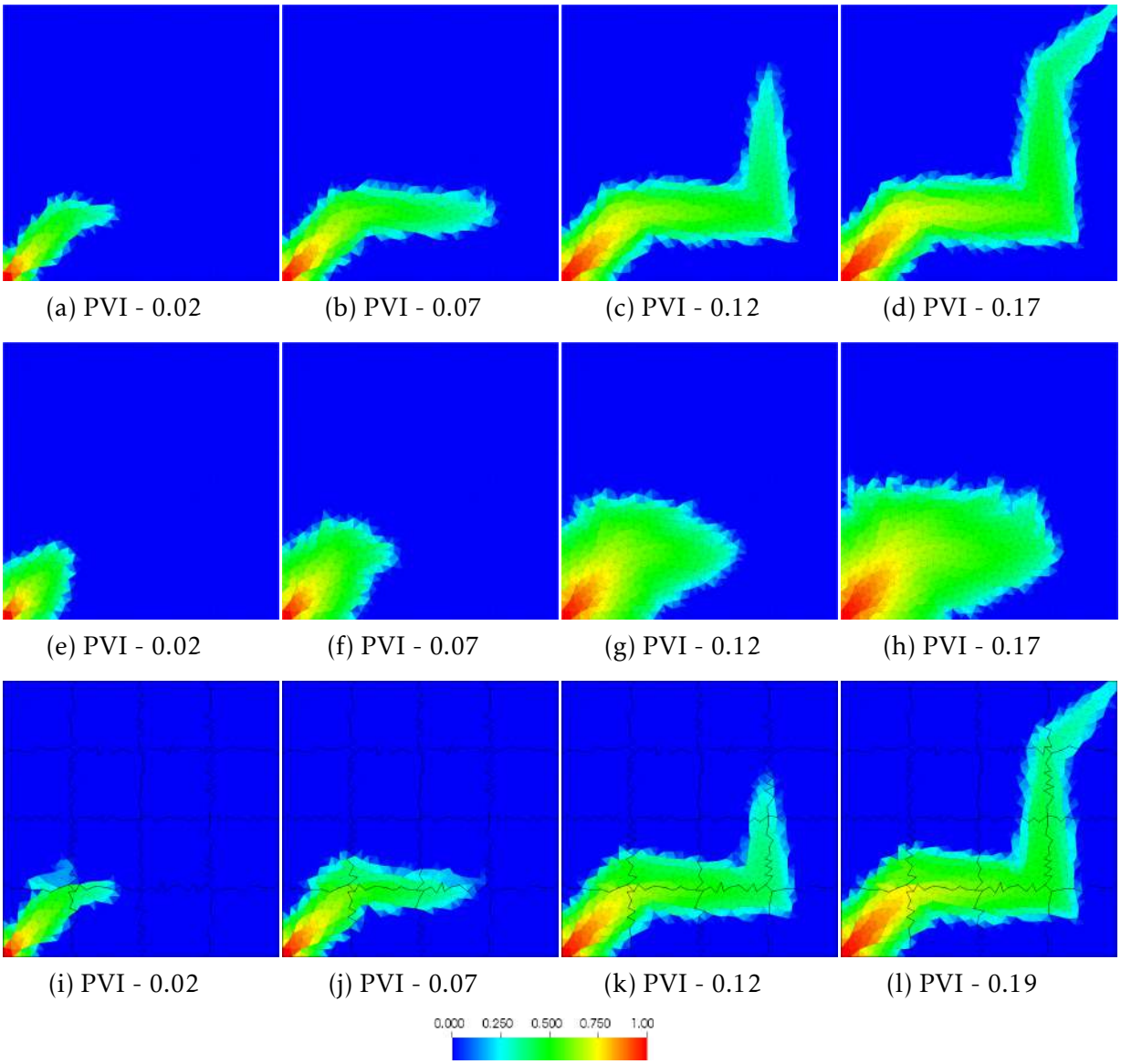

(a) PVI - 0.02 (b) PVI - 0.07 (c) PVI - 0.12 (d) PVI - 0.17

(e) PVI - 0.02 (f) PVI - 0.07 (g) PVI - 0.12 (h) PVI - 0.17

(i) PVI - 0.02 (j) PVI - 0.07 (k) PVI - 0.12 (l) PVI - 0.19

Source: Author

visible as the saturation front almost exactly replicates the MPFA-D fine scale solution. In contrast, the TPFA saturation solution shows no similarity to the MPFA-D solution.

The second fine-scale mesh used consists of a distorted unstructured grid with 2,496 quadrilateral elements, as shown in Figure 43b. Once more, the primal and dual coarse grids were created using a structured 4x4 background grid. Note that the saturation field of the fine-scale solution using the MPFA-D is affected by the grid orientation. In this case, the saturation front looks more diffusive and the breakthrough is delayed. The AMS-U multiscale solution also repeats this pattern, but with additional

Figure 45 – Oil and water flow in a heterogeneous reservoir with a discontinuous full tensor and high anisotropy ratios using mesh 2. a) to d) fine-scale solution using the MPFA-D; e) to h) fine scale solution using the TPFA method; i) to l) AMS-U + MPFA-D solution.

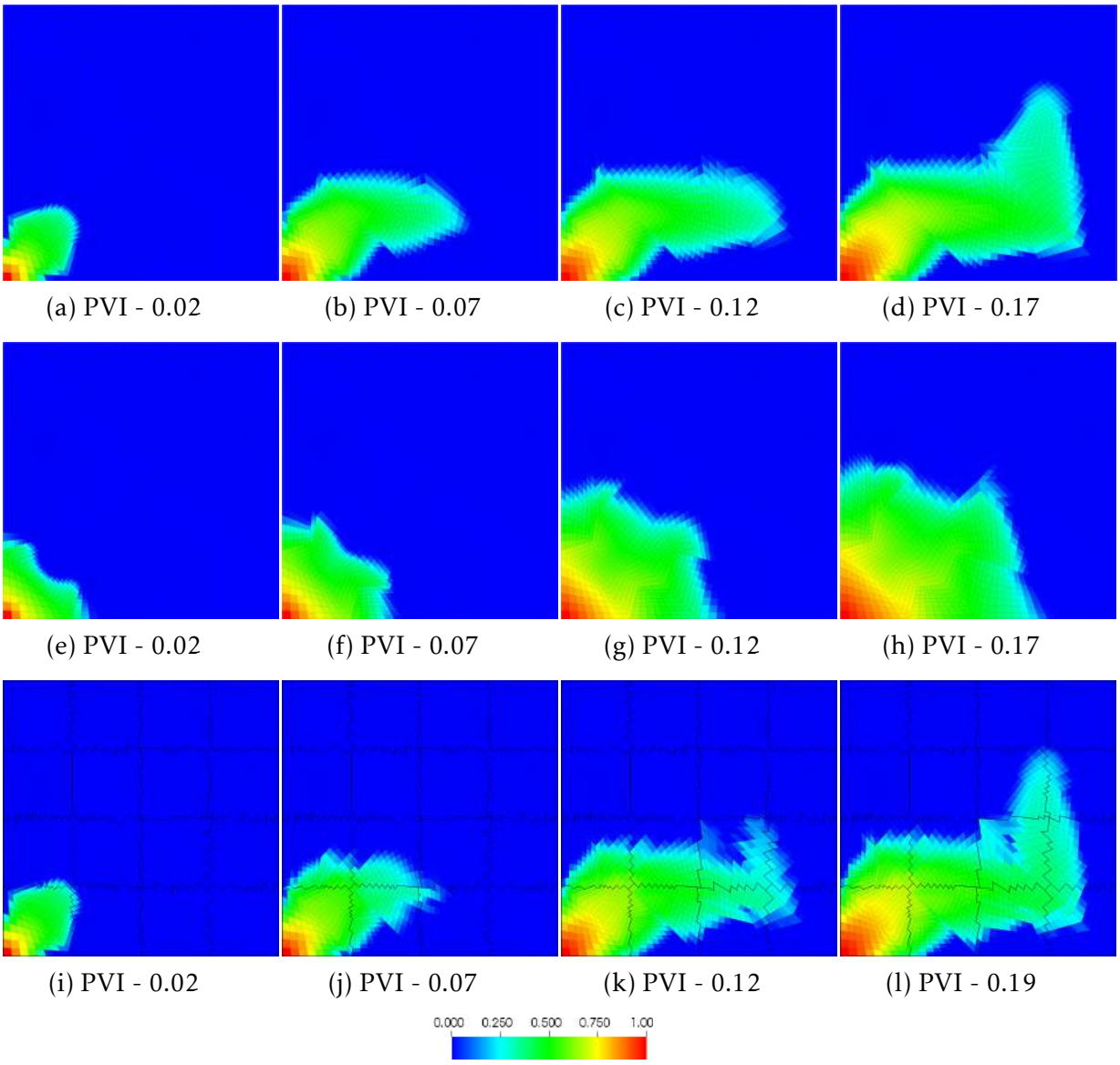

(a) PVI - 0.02 (b) PVI - 0.07 (c) PVI - 0.12 (d) PVI - 0.17

(e) PVI - 0.02 (f) PVI - 0.07 (g) PVI - 0.12 (h) PVI - 0.17

(i) PVI - 0.02 (j) PVI - 0.07 (k) PVI - 0.12 (l) PVI - 0.19

Source: Author

errors along the saturation front. In addition, the errors appear to decrease qualitatively with time. The TPFA fine-scale solution, in turn, is unable to capture the physics of the problem, indicating that the TPFA solution is extremely mesh dependent

The third mesh used is the finest mesh with 4,890 unstructured quadrilateral elements. This mesh is almost twice the size of the other meshes studied, as shown in Figure 43b. The primal and dual coarse grids were created using a structured 3x3 background grid. We note that the AMS-U saturation field is able to preserve the most important aspects of the high-resolution physics using the MPFA-D, see Figure 46.

Figure 46 – Oil and water flow in a heterogeneous reservoir with a discontinuous full tensor and high anisotropy ratios using mesh 3. a) to d) fine-scale solution using the MPFA-D; e) to h) fine scale solution using the TPFA method; i) to l) AMS-U + MPFA-D solution..

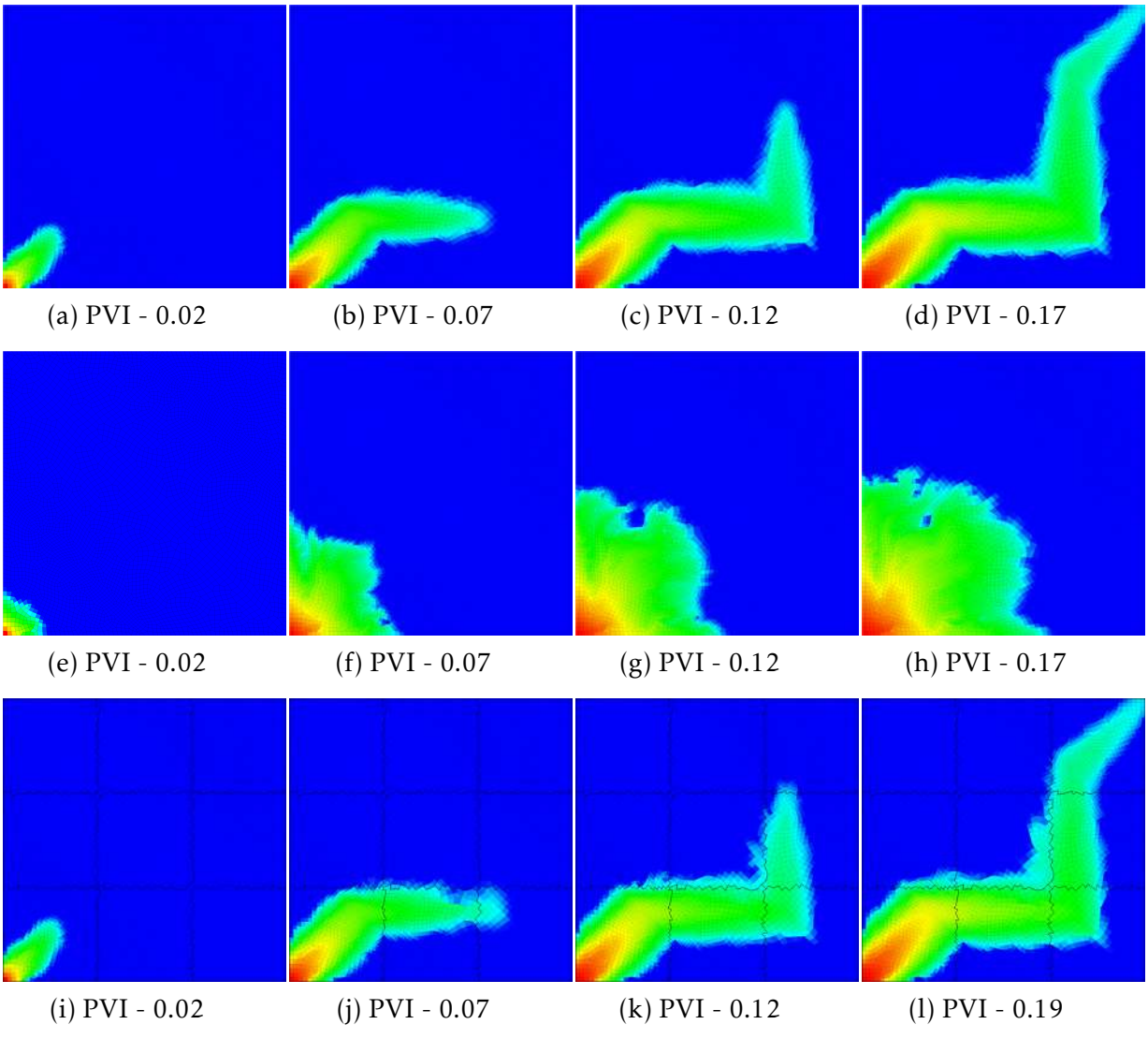

(a) PVI - 0.02 (b) PVI - 0.07 (c) PVI - 0.12 (d) PVI - 0.17

(e) PVI - 0.02 (f) PVI - 0.07 (g) PVI - 0.12 (h) PVI - 0.17

(i) PVI - 0.02 (j) PVI - 0.07 (k) PVI - 0.12 (l) PVI - 0.19

Source:Author

Note that both the fine-scale and multiscale solutions in this example are similar to the solution obtained with mesh 01. Qualitatively, the differences between the AMS-U and the MPFA-D solutions are small but not imperceptible. In particular, the saturation front for PVI=0.07 appears to cross a bottleneck, while the saturation front for PVI=0.17 looks smeared with more diffusion. Note that the bottleneck observed for PVI=0.07 was also obtained in simulations with different background grids. Finally, the TPFA fine-scale solution is again unable to resolve the physics of the problem, leading to a grid-dependent solution that is not consistent.

Figure 47 – Productions curves for all meshes simulating oil and water flow in a heterogeneous reservoir with a discontinuous full tensor and high anisotropy ratios.

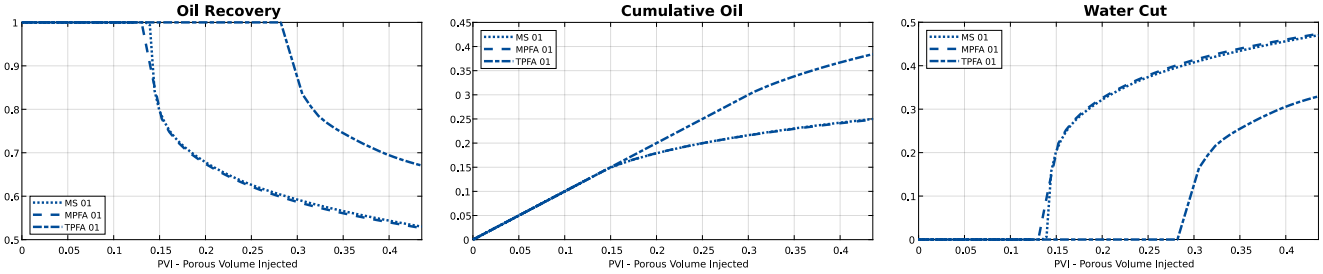

(a) 4x4 background grid with a fine-scale mesh with 2,328 triangular elements.

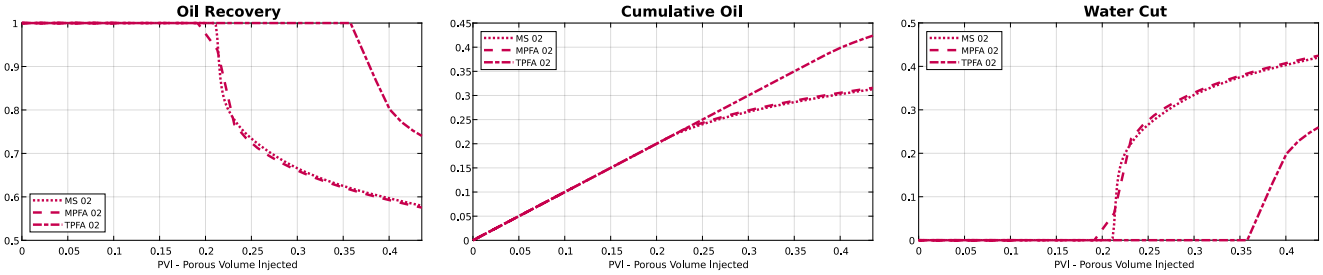

(b) 4x4 background grid with a fine-scale mesh with 2,496 quadrilateral elements.

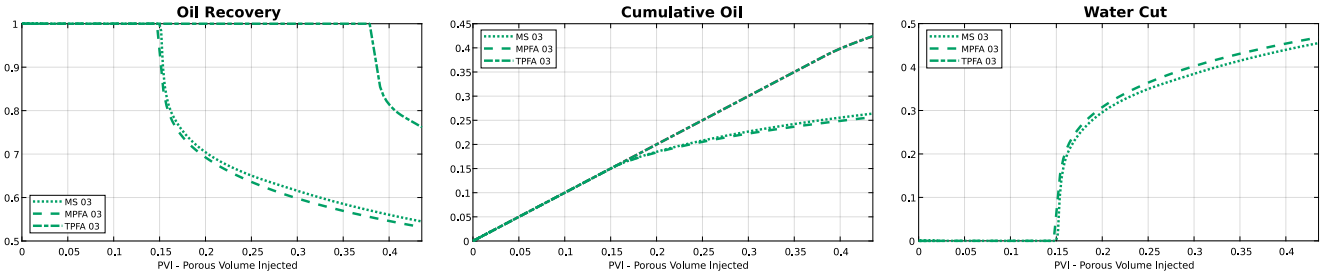

(c) 3x3 background grid with a fine-scale mesh with 4,890 quadrilateral elements.

Regarding the productions curves presented in Figure 47, we note the MPFA-D and the AMS-U and oil recovery curves for mesh 1 and 3 remain extremely close to one another despite the number of elements of the mesh. The production curve of mesh 2, in turn, shows a late breakthrough as observed qualitatively in the saturation fields. In all analysed grids, the AMS-U curves remained quite close to the corresponding MPFA-D fine-cale solution. Finally, for this problem, it is clear that the use of the classical linear TPFA method is unable to produce physical meaningful solutions even using the fine scale mesh.

The norm of the errors shown in Figure 48 evaluates how close the TPFA and AMS-U solutions coupled with an MPFA-D solution remain to the corresponding MPFA-D solution. As expected, the L_2 and L_∞ norms of the errors were higher for the TPFA saturation solution were higher in comparison with the others. The AMS-U replicated the MPFA-D solution for all meshes with good accuracy. Note that AMS-U depends on the accuracy of the MPFA-D fine-scale solution. The distortion of mesh 2 caused the

Figure 48 – L_2 and L_∞ norms of the saturation field obtained by simulating oil and Water flow in a heterogeneous reservoir with a discontinuous full tensor and high anisotropy ratios.

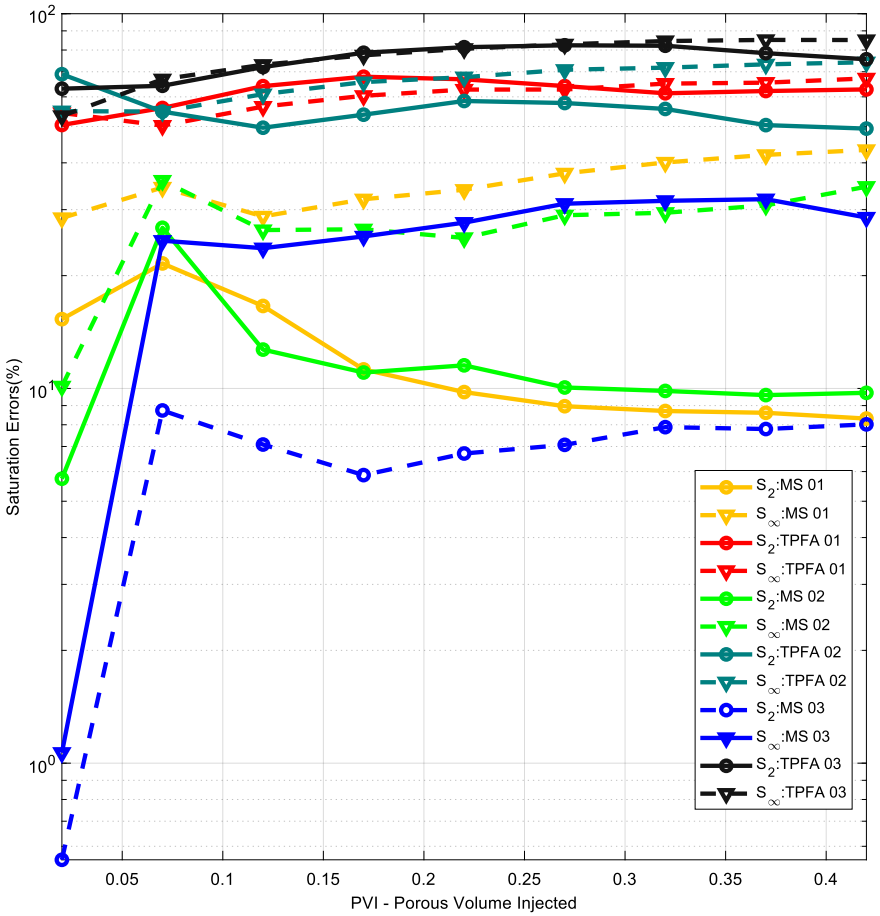

Source: Author

MPFA-D formulation to lose some of the physics of the problem. On the other hand, the best solution that multiscale methods based on TPFA can achieve is the fine-scale TPFA solution itself.

5.2.5 Two-phase flow of oil and water in a reservoir with a random permeability field

The last example consists of a two-phase flow of oil and water in a reservoir with a random isotropic permeability tensor adapted from Chueh et al. (2010) with two injections and one production well, as illustrated in Figure 49. Zero normal flow conditions are applied along the reservoir boundaries. Water is injected with $Q_{\text{inj}} = 1$ and $S_w = 1$ at the injection wells. At the single production well, the pressure is set to $p_{\text{pro}} = 0$. Again, the reservoir is assumed to be fully saturated with oil initially ($\bar{S}_w^o = 0$). An unstructured grid with 2,396 quadrilateral elements is used as the fine mesh, which was further refined around the production and injection wells. The tolerance of the iterative smoothing stage is again set to 10^{-6}.

Figure 49 – Representation of the log of the permeability field used for the two-phase flow of oil and water in a reservoir with a random permeability field. Injection wells, and the production well represented by red and white dots, respectively.

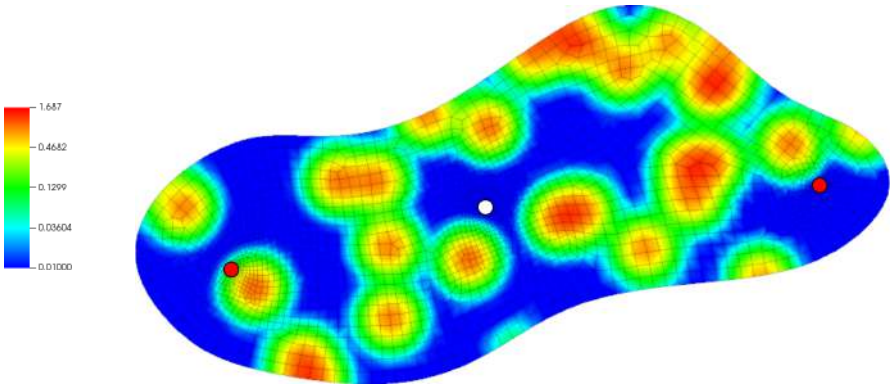

Source:Author

While most multiscale methods would struggle to define the primal and dual meshes for a curved geologic formation such as the one presented on Figure 49, the background grid strategy makes the process extremely straight forward. For this case, we have chosen an unstructured background grid with 19 quadrilateral elements as illustrated by Figure 50a. The corresponding primal and dual coarse grids are shown in Figure 50b.

The saturation profile presented in Figure 51 indicates that the AMS-U + MPFA-D qualitatively converge to the MPFA-D fine-scale solution for this configuration, with the largest difference between the saturation profiles occurring at the beginning of the simulation near PVI=0.045. It is possible to observe multiple saturation fronts moving from the two injection wells toward the production well. Despite small differences, the AMS-U in conjunction with the MPFA-D is able to accurately capture these details. In addition, the differences between the multiscale and MPFA fine-scale solutions become less visible over time. With the exception of a few cells on the saturation front, no significant difference is seen at PVI=0.26 and PVI=0.545. The norms of the errors of the saturation field shown in Figure 52 support the idea, also observed in the last example, that the error of the AMS-U solution tends to decrease with time. Note that around PVI=0.05 larger errors occur and around PVI=0.6 at the end of the simulation the L_2 norm of the error is close to 1 %, while the L_∞.

Finally, by observing the production curves in Figure 53, we find that the AMS-U formulation converges to the fine-scale solution. The oil production, cumulative oil and water cut curves remain virtually identical, demonstrating the robustness and accuracy of our formulation.

Figure 50 – Multiscale entities used for the two-phase flow of oil and water in a reservoir with a random permeability fieldd using a unstructured quadrilateral fine-scale mesh with 2,396 control volumes.

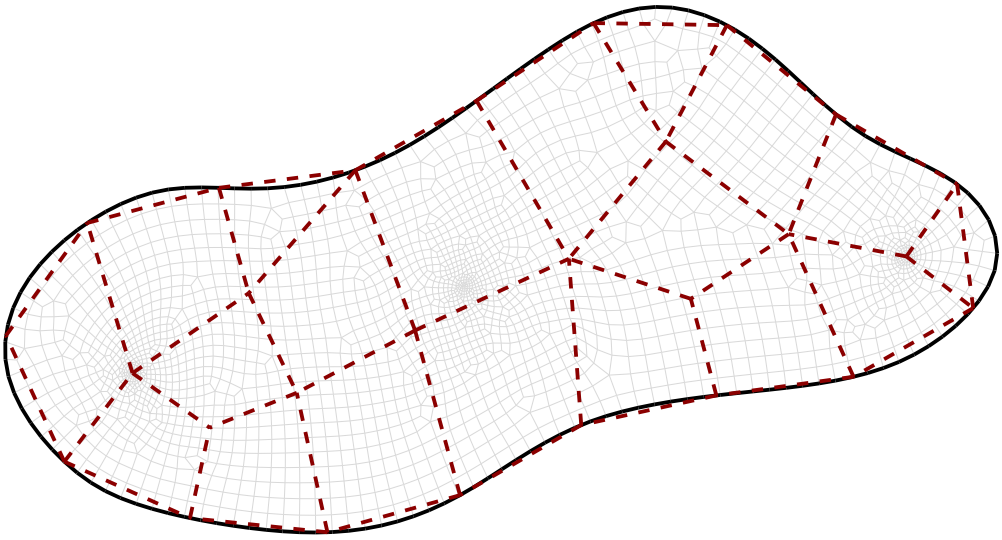

(a) Background grid adapting to the curved shaped reservoir.

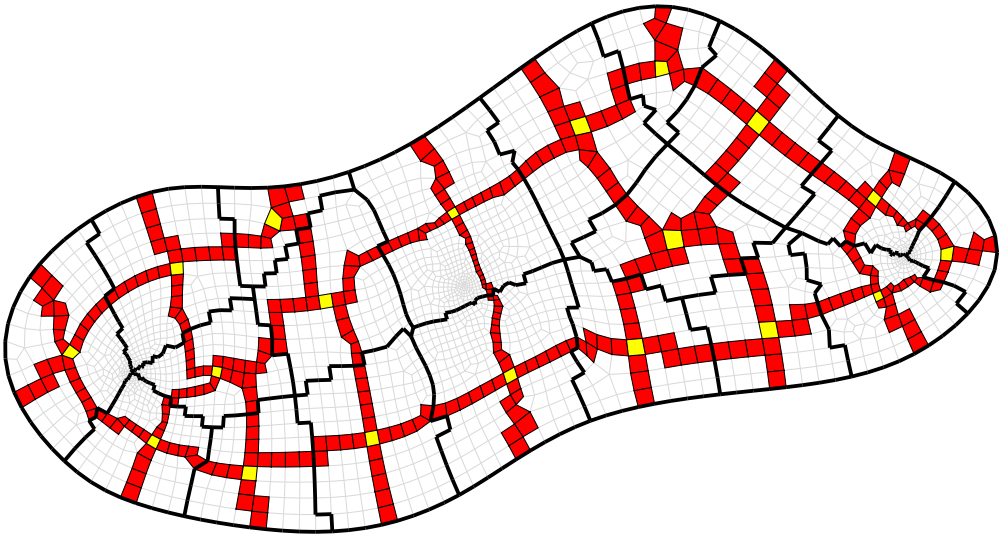

(b) Primal and dual grid also adapting to the curved shaped reservoir.

Source: Author

Figure 51 – Water-oil flow on a curved shaped reservoir with random permeability field: Reference, and multiscale solution on a rectangular grid and multiscale solution presented on the top and bottom row respectively.

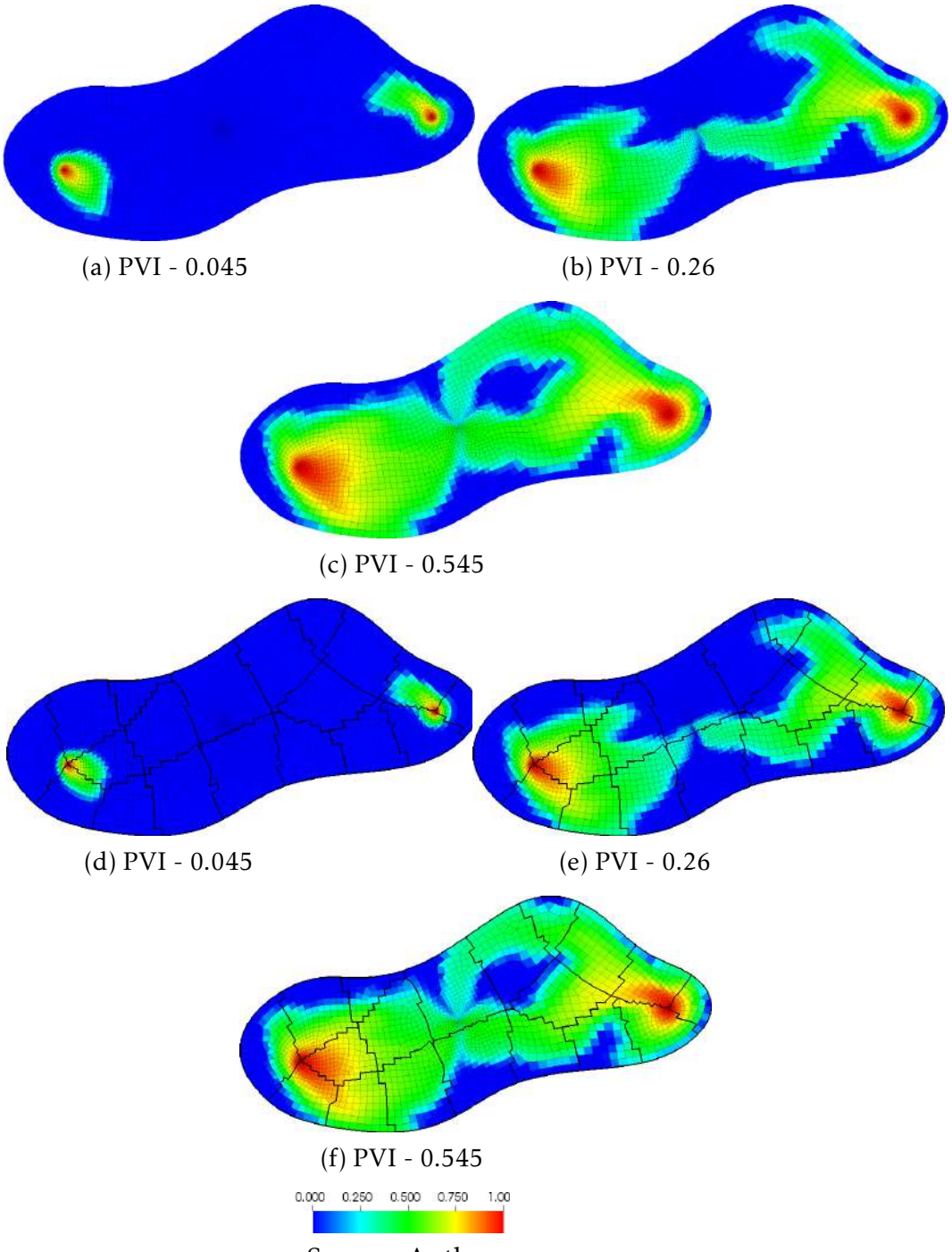

(a) PVI - 0.045 (b) PVI - 0.26

(c) PVI - 0.545

(d) PVI - 0.045 (e) PVI - 0.26

(f) PVI - 0.545

Source: Author

Figure 52 – L_2 and L_∞ norms of the saturation field obtained by water-oil flow on a curved shaped reservoir with random permeability field.

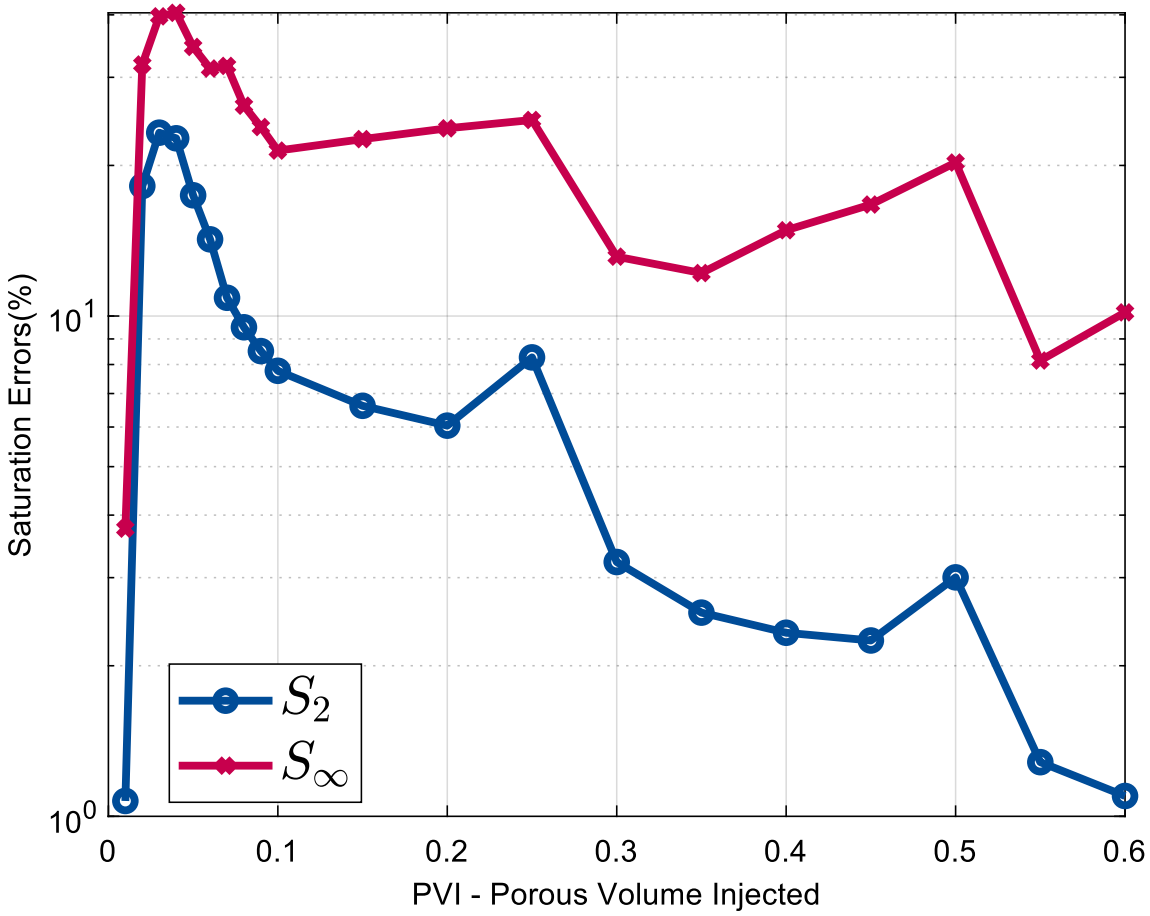

Source: Author

Figure 53 – Comparison of the production curves for the two-phase flow of oil and water in a reservoir with a random permeability field using the AMS-U + MPFA-D and the reference solution obtained using the MPFA-D directly in the fine mesh.

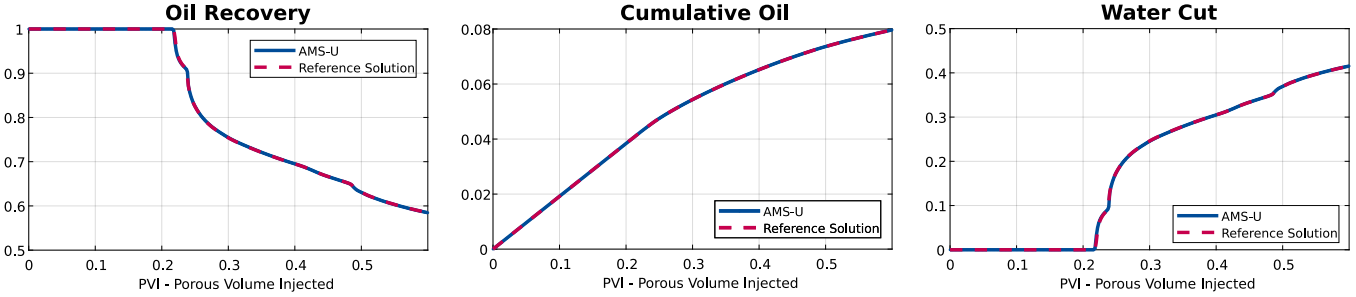

Source: Author

6 CONCLUSIONS

In the present work, we have investigated and developed formulations in the family of cell-centred finite volume methods. For this purpose, we have divided our work into two different groups of schemes developed for unstructured grids: the study of consistent flux approximations respecting the DMP and the study of mass-conservative multiscale methods. Both resulting formulations have been used to solve single-phase problems of incompressible flows in highly heterogeneous and anisotropic media, but for the latter we have also tested two-phase flow problems in equally challenging domains. On this case, we have used a sequential implicit strategy in which the pressure solution and the saturation equations are solved separately.

The first part of the work was concerned with the investigation and study of nonlinear flow approximation techniques consistent on general unstructured grids. We have successfully developed a novel repair technique for linear MPFA methods based on the M-Matrix Flux Splitting (EDWARDS, 2000) and the flux limitation concept in (KUZMIN; SHASHKOV; SVYATSKIY, 2009) that is able to convert these schemes into nonlinear methods that comply with the Discrete Maximum Principle. This strategy was tested using the MPFA-D for unstructured 2D grids with the conservative LPEW2 interpolation. The resulting framework was tested on benchmark problems for single-phase flows, which pushed the original MPFA-D to its limits. Nevertheless, our method was able to produce solutions that qualitatively reproduced the quality of the MPFA formulation while respecting the DMP. However, in some examples, it was observed that our method added more artificial diffusion for this purpose. The method was developed using a mathematical operator we developed that allows the transmissibility matrix to be written as a matrix multiplication between the divergent operator and the face transmissibility matrix. In this way, the mass balance is performed on a matrix. This operator allowed the vectorisation of the code, which increases the performance of our method. The results of our formulation were comparable to state-of-the-art nonlinear TPFA methods but with the computational costs to more extreme cases are still prohibitive.

As for the second part of this work, we have investigated and developed schemes and the associated algorithms necessary for the simulation of multiscale methods in the MsFV framework on unstructured grids. In particular, we have developed a generalisation of the state-of-the-art Algebraic Multiscale Solver (WANG; HAJIBEYGI; TCHELEPI, 2014) to unstructured grids. This was done by developing the background grid strategy, a novel technique that uses an additional grid to support the creation of the multiscale entities in 2-D and extendible to 3-D by using an MPFA for the fine-scale,

and by modifying the multiscale operators of the standard AMS to ensure that the basis functions are restricted to their respective support regions. Combined with an iterative smoothing stage, the resulting framework has been shown to be consistent even in highly heterogeneous and anisotropic media. Moreover, our method is the very flexible formulation in terms of creating the multiscale meshes, as it is able to make full use of unstructured meshes to create primal and dual coarse meshes that adapt he geometric features of convoluted physical domains.

Finally, the positive results obtained with the developed formulations motivate further research to improve and extend them to more general problems. In particular, the algorithms of both formulations have been developed in such a way that they can be easily extended to 3-D. Therefore, we can cite as possible future extensions of our work:

1. Extending the Flux Limited Splitting to 3-D.
2. Investigation of new algorithms for limiting the cross diffusion terms.
3. Create strategies to acelerate the FLS method.
4. Investigation and comparison of the FLS formulation with other robust flux approximation methods for unstructured grids such as the MPFA-H, FPS etc.
5. Extension of the background grid strategy to automatically adapt to the permeability field of the media to improve the multiscale solution.
6. Coupling the FLS strategy with multiscale schemes to create methods that comply with the DMP.
7. Extension of the AMS-U for 3-D.
8. Extend AMS-U to incorporate Non-Uniform ADM in unstructured grid enviroment.
9. Develop fracture models for the AMS-U.

REFERENCES

AAVATSMARK, I.; BARKVE, T.; BOE, O.; MANNSETH, T. Discretization on unstructured grids for inhomogeneous, anisotropic media. part i: Derivation of the methods. *SIAM Journal on Scientific Computing*, v. 19, n. 5, p. 1700–1716, 1998.

AAVATSMARK, I.; EIGESTAD, G.; MALLISON, B.; NORDBOTTEN, J. A compact multipoint flux approximation method with improved robustness. *Numerical Methods for Partial Differential Equations*, v. 24, n. 5, p. 1329–1360, 2008.

AZIZ, K.; SETTARI, A. *Petroleum resevoir simulation*. [S.l.]: Applied Science, 1979.

BARBOSA, L. M. C.; ANTUNES, A. R. E.; LYRA, P. R. M.; CARVALHO, D. K. E. An iterative modified multiscale control volume method for the simulation of highly heterogeneous porous media flow. *Journal of the Brazilian Society of Mechanical Sciences and Engineering*, Springer Science and Business Media LLC, v. 40, n. 2, jan 2018. Available on: <https://doi.org/10.1007/s40430-017-0929-z>.

BOSMA, S.; HAJIBEYGI, H.; TENE, M.; TCHELEPI, H. A. Multiscale finite volume method for discrete fracture modeling on unstructured grids (MS-DFM). *Journal of Computational Physics*, Elsevier BV, v. 351, p. 145–164, dec. 2017. Available on: <https://doi.org/10.1016/j.jcp.2017.09.032>.

BOSMA, S. B.; KLEVTSOV, S.; MØYNER, O.; CASTELLETTO, N. Enhanced multiscale restriction-smoothed basis (MsRSB) preconditioning with applications to porous media flow and geomechanics. *Journal of Computational Physics*, Elsevier BV, p. 109934, oct 2020. Available on: <https://doi.org/10.1016/j.jcp.2020.109934>.

BURDEN, R. L.; FAIRES, J. D. *Numerical analysis*. [S.l.]: Brooks/Cole, Cengage Learning, 2011.

CAO, H. *Development of Techniques for General Purpose Simulators*. Thesis (PhD) — Stanford University, 2002.

CARVALHO, D. K. E. de. *Uma Formulação do Método dos Volumes Finitos com Estrutura de Dados por Aresta para a Simulação de Escoamentos em Meios Porosos*. Thesis (PhD) — Federal University of Pernambuco, 2005.

CARVALHO, D. K. E. de; LYRA, P. R. M.; WILLMERSDORF, R. B.; ARAÚJO, F. D. S. An unstructured edge-based finite volume formulation for solving immiscible two-phase flows in porous media. *Communications in Numerical Methods in Engineering*, Wiley, v. 21, n. 12, p. 747–756, jul 2005. Available on: <https://doi.org/10.1002/cnm.790>.

CARVALHO, D. K. E. de; WILLMERSDORF, R. B.; LYRA, P. R. M. A node-centred finite volume formulation for the solution of two-phase flows in non-homogeneous porous media. *International Journal for Numerical Methods in Fluids*, v. 53, n. 8, p. 1197–1219, 2007.

CARVALHO, D. K. E. de; WILLMERSDORF, R. B.; LYRA, P. R. M. A node-centred finite volume formulation for the solution of two-phase flows in non-homogeneous

porous media. *International Journal for Numerical Methods in Fluids*, Wiley, v. 53, n. 8, p. 1197–1219, 2007. Available on: <https://doi.org/10.1002/fld.1238>.

CHEN, Q.-Y.; WAN, J.; YANG, Y.; MIFFLIN, R. T. Enriched multi-point flux approximation for general grids. *Journal of Computational Physics*, v. 227, n. 3, p. 1701–1721, 2008.

CHEN, Z.; HUAN, G.; MA, Y. *Computational methods for multiphase flows in porous media*. [S.l.]: Knovel, 2006.

CHUEH, C.; SECANELL, M.; BANGERTH, W.; DJILALI, N. Multi-level adaptive simulation of transient two-phase flow in heterogeneous porous media. *Computers & Fluids*, Elsevier BV, v. 39, n. 9, p. 1585–1596, oct 2010. Available on: <https://doi.org/10.1016/j.compfluid.2010.05.011>.

CONTRERAS, F. R.; CARVALHO, D. K.; GALINDEZ-RAMIREZ, G.; LYRA, P. R. A non-linear finite volume method coupled with a modified higher order muscl-type method for the numerical simulation of two-phase flows in non-homogeneous and non-isotropic oil reservoirs. *Computers & Mathematics with Applications*, v. 92, p. 120–133, 2021.

CONTRERAS, F. R.; LYRA, P. R.; CARVALHO, D. K. de. A new multipoint flux approximation method with a quasi-local stencil (mpfa-ql) for the simulation of diffusion problems in anisotropic and heterogeneous media. *Applied Mathematical Modelling*, v. 70, p. 659–676, 2019.

CONTRERAS, F. R. L. *Métodos de Volumes Finitos Robustos para a Simulação de Escoamentos Bifásicos de Água e Óleo em Reservátorios de Petróleo*. Thesis (PhD) — Federal University of Pernambuco, 2017.

CONTRERAS, F. R. L.; LYRA, P. R. M.; SOUZA, M. R. A.; CARVALHO, D. K. E. A cell-centered multipoint flux approximation od with a diamond stencil coupled with a higher order finite volume method for the simulation of oil-water displacements in heterogeneous and anisotropic petroleum reservoirs. *Computers and Fluids*, v. 127, p. 1–16, 2016.

CORMEN, T. H. *Introduction to Algorithms, 3rd Edition (The MIT Press)*. The MIT Press, 2009. ISBN 0262033844. Available on: <https://www.xarg.org/ref/a/0262033844/>.

CORTINOVIS, D.; JENNY, P. Zonal multiscale finite-volume framework. *Journal of Computational Physics*, v. 337, p. 84–97, 2017.

CRUMPTON, P.; SHAW, G.; WARE, A. Discretisation and multigrid solution of elliptic equations with mixed derivative terms and strongly discontinuous coefficients. *Journal of Computational Physics*, v. 116, n. 2, p. 343–358, 1995.

CUSINI, M.; FRYER, B.; KRUIJSDIJK, C. van; HAJIBEYGI, H. Algebraic dynamic multilevel method for compositional flow in heterogeneous porous media. *Journal of Computational Physics*, Elsevier BV, v. 354, p. 593–612, feb 2018.

DIJKSTRA, E. W. A note on two problems in connexion with graphs. *Numerische Mathematik*, Springer Science and Business Media LLC, v. 1, n. 1, p. 269–271, dec. 1959. Available on: <https://doi.org/10.1007/bf01386390>.

EDWARDS, M. G. M-matrix flux splitting for general full tensor discretization operators on structured and unstructured grids. *Journal of Computational Physics*, Academic Press Inc., v. 160, p. 1–28, 5 2000. ISSN 00219991.

EDWARDS, M. G.; ROGERS, C. F. Finite volume discretization with imposed flux continuity for the general tensor pressure equation. *Computational Geosciences*, v. 2, n. 4, p. 259–290, 1998.

EDWARDS, M. G.; ZHENG, H. A quasi-positive family of continuous darcy-flux finite-volume schemes with full pressure support. *Journal of Computational Physics*, v. 227, n. 22, p. 9333–9364, 2008.

EDWARDS, M. G.; ZHENG, H. Double-families of quasi-positive darcy-flux approximations with highly anisotropic tensors on structured and unstructured grids. *Journal of Computational Physics*, v. 229, n. 3, p. 594–625, 2010.

EWING, R. E. *The mathematics of reservoir simulation*. [S.l.]: Society for Industrial and Applied Mathematics (SIAM, 3600 Market Street, Floor 6, Philadelphia, PA 19104), 1983.

FRIIS, H. A.; EDWARDS, M. G. A family of mpfa finite-volume schemes with full pressure support for the general tensor pressure equation on cell-centered triangular grids. *Journal of Computational Physics*, Elsevier BV, v. 230, n. 1, p. 205–231, jan 2011.

FRIIS, H. A.; EVJE, S. Numerical treatment of two-phase flow in capillary heterogeneous porous media by finite-volume approximations. *Int. J. Numer. Anal. Mod*, v. 9, p. 505–208, 2012.

GAO, Z.; WU, J. A linearity-preserving cell-centered scheme for the heterogeneous and anisotropic diffusion equations on general meshes. *International Journal for Numerical Methods in Fluids*, v. 67, n. 12, p. 2157–2183, 2010.

GEUZAINE, C.; REMACLE, J.-F. Gmsh: A 3-d finite element mesh generator with built-in pre- and post-processing facilities. *International Journal for Numerical Methods in Engineering*, v. 79, n. 11, p. 1309–1331, 2009.

HAJIBEYGI, H.; BONFIGLI, G.; HESSE, M. A.; JENNY, P. Iterative multiscale finite-volume method. *Journal of Computational Physics*, Elsevier BV, v. 227, n. 19, p. 8604–8621, oct 2008. Available on: <https://doi.org/10.1016/j.jcp.2008.06.013>.

HAJIBEYGI, H.; JENNY, P. Multiscale finite-volume method for parabolic problems arising from compressible multiphase flow in porous media. *Journal of Computational Physics*, Elsevier BV, v. 228, n. 14, p. 5129–5147, aug 2009. Available on: <https://doi.org/10.1016/j.jcp.2009.04.017>.

HAJIBEYGI, H.; JENNY, P. Adaptive iterative multiscale finite volume method. *Journal of Computational Physics*, Elsevier BV, v. 230, n. 3, p. 628–643, feb 2011. Available on: <https://doi.org/10.1016/j.jcp.2010.10.009>.

HAJIBEYGI, H.; JENNY, P. Adaptive iterative multiscale finite volume method. *Journal of Computational Physics*, v. 230, n. 3, p. 628–643, 2011.

HAJIBEYGI, H.; OLIVARES, M. B.; HOSSEINIMEHR, M.; POP, S.; WHEELER, M. A benchmark study of the multiscale and homogenization methods for fully implicit multiphase flow simulations. *Advances in Water Resources*, Elsevier BV, v. 143, p. 103674, sep 2020. Available on: <https://doi.org/10.1016/j.advwatres.2020.103674>.

HAJIBEYGI, H.; TCHELEPI, H. A. Compositional multiscale finite-volume formulation. *SPE Journal*, Society of Petroleum Engineers (SPE), v. 19, n. 02, p. 316–326, apr 2014. Available on: <https://doi.org/10.2118/163664-pa>.

HELMIG, R. *Multiphase Flow and Transport Processes in the Subsurface555*. [S.l.: s.n.], 1997.

HIRSCH, C. *Numerical computation of internal and external flows*. [S.l.]: Wiley, 2002.

HURTADO, F. S. V. *Formulação Tridimensional de Volumes Finitos para Simulação de Reservatórios de Petróleo com Malhas Não-Estruturadas Híbridas*. Thesis (PhD) — Federal University of Santa Catarina, 2011.

JENNY, P.; LEE, S.; TCHELEPI, H. Multi-scale finite-volume method for elliptic problems in subsurface flow simulation. *Journal of Computational Physics*, v. 187, n. 1, p. 47–67, 2003.

JENNY, P.; LEE, S.; TCHELEPI, H. Adaptive fully implicit multi-scale finite-volume method for multi-phase flow and transport in heterogeneous porous media. *Journal of Computational Physics*, v. 217, n. 2, p. 627–641, 2006.

JENNY, P.; LUNATI, I. Modeling complex wells with the multi-scale finite-volume method. *Journal of Computational Physics*, Elsevier BV, v. 228, n. 3, p. 687–702, feb 2009. Available on: <https://doi.org/10.1016/j.jcp.2008.09.026>.

JUVITO, L.; RAMIREZ, G. G.; SOUZA, A. C. R. de; CARVALHO, D. K. E. de; LYRA, P. R. M. An iterative MsCV method coupled to the high-resolution CPR approach via different solution smoothers for the simulation of oil-water flows in 2-D petroleum reservoirs on unstructured grids. *Proceedings of Ibero-Latin American Congress on Computational Methods in Engineering (CILAMCE 2020)*, 2020.

KUZMIN, D.; SHASHKOV, M.; SVYATSKIY, D. A constrained finite element method satisfying the discrete maximum principle for anisotropic diffusion problems. *Journal of Computational Physics*, Elsevier BV, v. 228, n. 9, p. 3448–3463, may 2009. Available on: <https://doi.org/10.1016/j.jcp.2009.01.031>.

LEE, S. H.; WOLFSTEINER, C.; TCHELEPI, H. A. Multiscale finite-volume formulation for multiphase flow in porous media: black oil formulation of compressible, three-phase flow with gravity. *Computational Geosciences*, Springer Science and Business Media LLC, v. 12, n. 3, p. 351–366, jan 2008. Available on: <https://doi.org/10.1007/s10596-007-9069-3>.

LHNER, R. *Applied Computational Fluid Dynamics Techniques*. John Wiley & Sons, Ltd, 2008. Available on: <https://doi.org/10.1002/9780470989746>.

LUNATI, I.; JENNY, P. Multiscale finite-volume method for compressible multiphase flow in porous media. *Journal of Computational Physics*, Elsevier BV, v. 216, n. 2, p. 616–636, aug 2006. Available on: <https://doi.org/10.1016/j.jcp.2006.01.001>.

LUNATI, I.; JENNY, P. Multiscale finite-volume method for density-driven flow in porous media. *Computational Geosciences*, Springer Science and Business Media LLC, v. 12, n. 3, p. 337–350, jan 2008. Available on: <https://doi.org/10.1007/s10596-007-9071-9>.

LUNATI, I.; TYAGI, M.; LEE, S. H. An iterative multiscale finite volume algorithm converging to the exact solution. *Journal of Computational Physics*, Elsevier BV, v. 230, n. 5, p. 1849–1864, mar 2011. Available on: <https://doi.org/10.1016/j.jcp.2010.11.036>.

MEHRDOOST, Z. Unstructured grid adaptation for multiscale finite volume method. *Computational Geosciences*, Springer Science and Business Media LLC, v. 23, n. 6, p. 1293–1316, oct 2019. Available on: <https://doi.org/10.1007/s10596-019-09878-9>.

MEHRDOOST, Z. Multiscale finite volume method with adaptive unstructured grids for flow simulation in heterogeneous fractured porous media. *Engineering with Computers*, 2021.

MOYNER, O.; LIE, K.-A. The multiscale finite volume method on unstructured grids. In: *SPE Reservoir Simulation Symposium*. Society of Petroleum Engineers, 2013. Available on: <https://doi.org/10.2118/163649-ms>.

MOYNER, O.; LIE, K.-A. A multiscale restriction-smoothed basis method for high contrast porous media represented on unstructured grids. *Journal of Computational Physics*, v. 304, p. 46–71, 2015.

PAL, M.; EDWARDS, M. Flux-splitting schemes for improved monotonicity of discrete solutions of elliptic equations with highly anisotropic coefficients. 2006.

PAL, M.; EDWARDS, M. G. Non-linear flux-splitting schemes with imposed discrete maximum principle for elliptic equations with highly anisotropic coefficients. *International Journal for Numerical Methods in Fluids*, v. 66, 5 2011.

PARRAMORE, E.; EDWARDS, M. G.; PAL, M.; LAMINE, S. Multiscale finite-volume cvd-mpfa formulations on structured and unstructured grids. *Multiscale Modeling & Simulation*, v. 14, n. 2, p. 559–594, 2016.

PRICE, H. S. Monotone and oscillation matrices applied to finite difference approximations. *Mathematics of Computation*, American Mathematical Society (AMS), v. 22, n. 103, p. 489–516, 1968. Available on: <https://doi.org/10.1090/s0025-5718-1968-0232550-5>.

PROTTER, M. H.; WEINBERGER, H. F. *Maximum principles in differential equations*. [S.l.]: Springer, 1984.

QUEIROZ, L. E. S.; SOUZA, M. R. A.; CONTRERAS, F. R. L.; LYRA, P. R. M.; CARVALHO, D. K. E. de. On the accuracy of a nonlinear finite volume method for the solution of diffusion problems using different interpolations strategies. *International Journal for Numerical Methods in Fluids*, v. 74, n. 4, p. 270–291, 2013.

SAAD, Y. *Iterative methods for sparse linear systems*. [S.l.]: Society for Industrial and Applied Mathematics, 2003.

SANTOS, J. C. A.; ANDRADE, J. P. R.; SOUZA, A. C. R.; FILHO, R. J. M. L.; CARVALHO, D. K. E.; LYRA, P. R. M. An Adaptive Algebraic Dynamic Multilevel (A-ADM) and Multiscale Method with Enriched Basis Functions for the simulation of two-phase flows in highly heterogeneous petroleum reservoirs. *Proceedings of Ibero-Latin American Congress on Computational Methods in Engineering (CILAMCE 2020)*, 2020.

SANTOS, J. C. A. dos; LYRA, P. R. M.; ANDRADE, J. P. R. de; SOUZA, A. C. R. de; FILHO, R. J. M. de L.; CARVALHO, D. K. E. de. An Algebraic Dynamic Multilevel and Multiscale Method with Non-Uniform Mesh Resolution and Adaptive Algebraic Multiscale Solver operator for the simulation of two-phase flows in highly heterogeneous petroleum reservoirs. *Journal of Computational Physics*, p. 111174, 2022.

SHENG, Z.; YUAN, G. A cell-centered nonlinear finite volume scheme preserving fully positivity for diffusion equation. *Journal of Scientific Computing*, v. 68, n. 2, p. 521–545, 2015.

SILVA, R. N. T.; MATOS, G. M.; SOUZA, A. C. R. de; FILHO, R. J. M. L.; CARVALHO, D. K. E. de; LYRA, P. R. M. Some results on the accuracy of a classical upscaling technique using an Intuitive Multilevel Preprocessor for Smart Simulation. *Proceedings of Ibero-Latin American Congress on Computational Methods in Engineering (CILAMCE 2020)*, 2020.

SOUZA, A. C. R. de. *A MsCV framework using a non-orthodox MPFA-D for the simulation of two-phase flows on truly unstructured grids*. Dissertação (Master's) — Federal University of Pernambuco, 2018.

SOUZA, A. C. R. de; BARBOSA, L. M. C.; CONTRERAS, F. R. L.; LYRA, P. R. M.; CARVALHO, D. K. E. de. A Multiscale Control Volume framework using the Multiscale Restriction Smooth Basis and a non-orthodox Multi-Point Flux Approximation for the simulation of two-phase flows on truly unstructured grids. *Journal of Petroleum Science and Engineering*, Elsevier BV, v. 188, p. 106851, may 2020. Available on: <https://doi.org/10.1016/j.petrol.2019.106851>.

SOUZA, A. C. R. de; CARVALHO, D. K. E. de; SANTOS, J. C. A. dos; WILLMERSDORF, R. B.; LYRA, P. R. M.; EDWARDS, M. G. An algebraic multiscale solver for the simulation of two-phase flow in heterogeneous and anisotropic porous media using general unstructured grids (AMS-U). *Applied Mathematical Modelling*, Elsevier BV, v. 103, p. 792–823, mar 2022. Available on: <https://doi.org/10.1016/j.apm.2021.11.017>.

SOUZA, A. C. R. de; CAVALCANTE de T. M.; CARVALHO, D. K. E. de; EDWARDS, M. G.; LYRA, P. R. M. Numerical simulation of the diffusion equation via a Non-linear Flux Splitting technique with the Multi-Point Flux Approximation method with a Diamond stencil satisfying the Discrete Maximum Principle using 2-D unstructured meshes. *Proceedings of the 26th International Congress of Mechanical Engineering*, 2021.

SOUZA, M. R. de A. *Simulação Numérica de Escoamento Bifásico em Reservatórios de Petróleo Heterogêneos e Anisotrópicos Utilizando um Método de Volumes Finitos "Verdadeiramente Multidimensional" com Aproximação de Alta Ordem*. Thesis (PhD) — Federal University of Pernambuco, 2015.

ŢENE, M.; KOBAISI, M. S. A.; HAJIBEYGI, H. Algebraic multiscale method for flow in heterogeneous porous media with embedded discrete fractures (f-AMS). *Journal*

of Computational Physics, Elsevier BV, v. 321, p. 819–845, sep 2016. Available on: <https://doi.org/10.1016/j.jcp.2016.06.012>.

ŢENE, M.; WANG, Y.; HAJIBEYGI, H. Adaptive algebraic multiscale solver for compressible flow in heterogeneous porous media. *Journal of Computational Physics*, Elsevier BV, v. 300, p. 679–694, nov 2015. Available on: <https://doi.org/10.1016/j.jcp.2015.08.009>.

TEREKHOV, K. M.; MALLISON, B. T.; TCHELEPI, H. A. Cell-centered nonlinear finite-volume methods for the heterogeneous anisotropic diffusion problem. *Journal of Computational Physics*, v. 330, p. 245–267, 2017.

VARGA, R. S. *Matrix iterative analysis*. [S.l.]: Springer, 2009.

VORST, H. A. van der. Bi-CGSTAB: A fast and smoothly converging variant of bi-CG for the solution of nonsymmetric linear systems. *SIAM Journal on Scientific and Statistical Computing*, Society for Industrial & Applied Mathematics (SIAM), v. 13, n. 2, p. 631–644, mar 1992. Available on: <https://doi.org/10.1137/0913035>.

WANG, Y.; HAJIBEYGI, H.; TCHELEPI, H. A. Algebraic multiscale solver for flow in heterogeneous porous media. *Journal of Computational Physics*, Elsevier BV, v. 259, p. 284–303, feb 2014. Available on: <https://doi.org/10.1016/j.jcp.2013.11.024>.

WANG, Y.; HAJIBEYGI, H.; TCHELEPI, H. A. Monotone multiscale finite volume method. *Computational Geosciences*, Springer Science and Business Media LLC, v. 20, n. 3, p. 509–524, aug 2015. Available on: <https://doi.org/10.1007/s10596-015-9506-7>.

WOLFSTEINER, C.; LEE, S. H.; TCHELEPI, H. A. Well modeling in the multiscale finite volume method for subsurface flow simulation. *Multiscale Modeling & Simulation*, Society for Industrial & Applied Mathematics (SIAM), v. 5, n. 3, p. 900–917, jan 2006. Available on: <https://doi.org/10.1137/050640771>.

WU, J.; GAO, Z. Interpolation-based second-order monotone finite volume schemes for anisotropic diffusion equations on general grids. *Journal of Computational Physics*, v. 275, p. 569–588, 2014.

YUAN, G.; SHENG, Z. Monotone finite volume schemes for diffusion equations on polygonal meshes. *Journal of Computational Physics*, Elsevier BV, v. 227, n. 12, p. 6288–6312, jun 2008. Available on: <https://doi.org/10.1016/j.jcp.2008.03.007>.

ZHOU, H.; TCHELEPI, H. A. Operator-based multiscale method for compressible flow. *SPE Journal*, v. 13, n. 02, p. 267–273, 2008.

ZHOU, H.; TCHELEPI, H. A. Two-stage algebraic multiscale linear solver for highly heterogeneous reservoir models. In: *SPE Reservoir Simulation Symposium*. Society of Petroleum Engineers, 2011. Available on: <https://doi.org/10.2118/141473-ms>.

APPENDIX A – PREPROCESSING ALGORITHMS

Generalising the preprocessing phase of multiscale methods is one of the major challenges to be overcome in order to extend these methods for unstructured grids. The non-iterative multiscale solution strongly depends on the quality of the primary and dual coarse grid as well as on the multiscale operators (SOUZA et al., 2020; MEHRDOOST, 2019; MOYNER; LIE, 2015). On the other hand, the right choice of preprocessing algorithm can significantly reduce the number of steps an iterative multiscale solution needs to converge.

Several studies have addressed the development of preprocessing algorithms for multiscale methods using different strategies (MOYNER; LIE, 2013; MOYNER; LIE, 2015; BOSMA et al., 2017; MEHRDOOST, 2019; SOUZA et al., 2020). So far, agglomeration methods, as used in parallel programming load distribuitiong in parallel programming have often been chosen to define the primal coarse grid (BOSMA et al., 2017; MOYNER; LIE, 2015; MEHRDOOST, 2019). Another recurrent choice is to use geometry-dependent algorithms to find a pseudo-similar structured primal coarse grid (SOUZA et al., 2020; MOYNER; LIE, 2013). Both of these strategies have advantages and disadvantages. While the former approach is better suited for discretising physical domains with complex geological formations, the generated partitions are based solely on parallel computer metrics, which in turn can lead to oscillations in the multiscale solution. The latter geometric approach simplifies the calculation of multiscale entities. However, its application is limited compared to the first approach.

Various authors have attempted to extend the MsFV definition for dual coarse grids to extend its application to general grids i.e. unstructured grids at the coarse and fine-scale (SOUZA et al., 2020; MOYNER; LIE, 2013; BOSMA et al., 2017; MOYNER; LIE, 2015; MEHRDOOST, 2019). For simplicity, we combine the different techniques into a global macro-algorithm described as follows:

1. Define the Primal Coarse Volume Centres x_k^p, $\forall \Omega_k^c \in \Omega^c$.
2. Define the Primal Coarse Face Centres y_j^p, $\forall \Gamma_j^c \in \Omega^c$.
3. Create the sub-edges: Find a path that connects x_k^p to y_j^p $\forall \Gamma_j^c \in \partial\Omega_k^c$ ensuring face connectivities.
4. Create the edges and dual coarse internals.
5. Define the Support Regions I_k, x_k^p $\forall \Omega_k^c \in \Omega^c$.

Apart from the MsRSB (MOYNER; LIE, 2015) and the MsCV (SOUZA et al., 2020), which tackle the definition Support Region before the creation of the sub-edges and edges, the main difference between the strategies is the algorithm used in each step of the procedure. While most authors have relied on algorithms that depend on geometry (SOUZA et al., 2020; MOYNER; LIE, 2015; MOYNER; LIE, 2013; BOSMA et al., 2017), more recent work has used a topologically based approach (MEHRDOOST, 2019; MEHRDOOST, 2021). The primal and dual coarse grids are inherently interdependent. Therefore, the choice of the primal coarse grid directly affects the construction and quality of the dual coarse grid. On the other hand, not all algorithms used to construct the dual coarse grid are suitable for every coarse grid definition. Consequently, it is difficult to assess the quality of the primary coarse grid without considering the impact of the strategy used to create the dual coarse grid and vice versa. Therefore, it makes sense to develop an unified strategy to create the prima and dual coarse grids together.

A.1 Unstructured Grids and Graphs

We note that unstructured grids by definition require special data structures to describe the elements, connectivities and other features of the grid. The nature and complexity of these data structures depends on the application and the numerical scheme chosen (LHNER, 2008; CAO, 2002). Standard cell-centred finite volume methods and other schemes that project the discrete fluxes onto faces (or edges in 2D) rely on a specific data structure to define the connectivities of the faces. The structure maps each face in the discrete domain to the neighbouring elements that share that face. Essentially, this construction is a representation of an undirected sparse graph using an adjacency list, where the nodes and edges of the graph represent the control volumes and the faces of the grid, respectively, as shown in Figure (54).

Understanding the nature of unstructured grids allow us to use various topological algorithms based on graphs that can be used to construct multiscale entities. In this context, we would like to highlight Dijkstra's algorithm (DIJKSTRA, 1959; CORMEN, 2009), which computes the shortest path between two nodes in an undirected graph with positively weighted edges, i.e. a graph like the one in Figure 54, where the edges are weighted, in this case by the distance between each control volume. See algorithm 2 for a description of Dijkstra's algorithm.

Putting this algorithm in the context of unstructured grids, different choices for the weights of the graph edges give rise to different interpretations. For example, if we set all the weights to 1, this routine finds the shortest topological distance, while if the weights take the value of the distance between the volume centroids, the algorithm finds the geometrically shortest distance. In all cases, we are able to find paths that ensure the connectivity of the faces.

Figure 54 – An illustration of a graph representation of a unstructured grid and its corresponding adjacency-list.

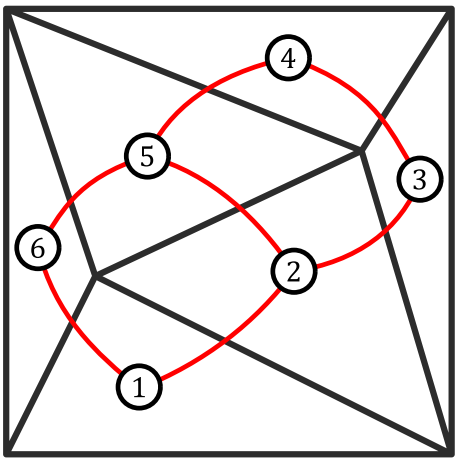

Adjacency List of Graph	
Neighbour 1	Neighbour 2
1	2
1	6
2	3
2	5
3	4
4	5
5	6

Source: (SOUZA et al., 2022).

Algorithm 2: Dijkstra's Weighted Shortest Path Algorithm

Input: A positive weighted undirected graph **G** , a **source** and **target** nodes
Output: A list **L** with sorted nodes containing the shortest distance from **source** to **target** in **G**

```
create set of nodes N
foreach node i in G do
    dist[i] ← ∞
    prev[i] ← NaN
    add i to N
dist[source] ← 0
while N is not empty do
    u ← node in N with minimum dist[u]
    remove u from N
    foreach neighbour i of u do
        tdist ← dist[u] + length(u, i)
        if condition then
            dist[i] ← tdist
            dprev[i] ← u
L ← create list
i ← target
if prev[i] ≠ NaN or source = i then
    while i ≠ NaN do
        place i at the start of L
        i ← prev[i]
```

A.2 The Background Grid Framework

The Background Grid Framework consists of a set of routines for creating multi-scale entities such as the primal coarse grid, the primal coarse volume centres, the dual coarse grid and other related entities. This strategy is named after the auxiliary coarse grid, the background grid, which geometrically and topologically guides the creation of the primal and dual coarse grids. By using this auxiliary grid, we are essentially able to tackle the design of the primary and dual coarse grids simultaneously. The procedure is designed to satisfy three basic assumptions. First, we assume that the fine-scale grid is derived from a given geological grid. Therefore, the primal and dual coarse meshes must be adapted to the fine scale and not vice versa. Secondly, the primal coarse grids must take into account the complex geological features of the petroleum reservoirs, as must the fine-scale grids. Finally, as far as possible, the algorithm must create grids that can be used in upscaling. Hence, strongly non-convex volumes should be avoided.

We illustrate how the background grid framework creates the primal and dual coarse grids by using an example of a physical domain shaped like the Chinese and Japanese character for friend, 友. The following procedure, shown in Figure 55, summarises the strategy:

1. First we create the background grid. This additional coarse grid is obtained by meshing the geometry of the formation with a conventional grid generator (GEUZAINE; REMACLE, 2009), disregarding the high-resolution grid (Figure 55a). This means that the background grid framework allows the boundaries of the volumes of the background grid to cross the surfaces of the fine-scale elements if necessary (see 55b).

2. The second step is to map the volumes of the fine-scale to the background grid by checking which centroids of the fine-scale are contained in each volume of the background grid (see figure). In some cases, as shown in Figure 55d, the centroid of some volumes of the fine-scale may lie outside the boundaries of the background grid. At this point, the resulting distribution does not guarantee face-connectivity among fine-scale elements contained in each volume of the background grid.

3. To solve these problems, the algorithms 3 and 4 are used. The former adds unmapped fine-scale volumes to the group of mapped volumes closest to them. The second algorithm evaluates and moves fine-scale volumes to ensure that the resulting mapped groups have face-connectivities (see figure 55e). The new derived regions are defined as a primal-coarse grid (see Figure 55f). Note that these algorithms introduced connectivities among the primal coarse volumes that were not present in the background grid (see Figure 55g).

4. For most multiscale schemes, computing the centres of the primal volumes x^p and faces y^p is challenging. To solve this problem, we use the geometry and topology of the background grid. First, the primal coarse centres are calculated by simply finding the fine-scale volumes whose centroid is closest to the centroid of the background volume (see Figure 55h). It is possible to move the centres of the primal coarse volumes adjacent to $\partial\Omega$ to a fine-scale volume closest to the centre of the primal coarse face $\Gamma_j \forall \Omega_j \in \partial\Omega$ (BARBOSA et al., 2018). The centres of the primal coarse faces are then computed by finding a fine-scale face in a given primal coarse face Γ_j that is closest to the corresponding centroid of the background grid face. Note that the centre of primal coarse faces and subsequent entities that depend on them are not computed if an associated face on the background grid does not exist, such as the face highlighted in the figure (55g).

5. The next step is to find all the sub-edges that make up the multiscale edges. The sub-edges are a set of face-connected fine-scale volumes that connect the centre of a coarse primal coarse volume to the centre of a coarse primal face. This is done by iterating over the faces of each primal coarse volume, as described in the algorithm 5. The edges group is the union of all sub-edges. Finally, we define the internal volumes by obtaining the fine-scale elements that are neither edges nor nodes. The resulting dual coarse grid is shown in Figure 55i.

We are currently developing a 3-D version of the background grid strategy. In 2D, the background grid strategy has already dealt with how to find nodes, edges and internal volumes. In 3-D, the biggest challenge we have encountered so far is finding a strategy for calculating the surfaces elements of the wirebasket classification ensuring face-connectivity while respecting the hierarchy of the AMS is respected, i.e. a clear separation between nodes, edges, surfaces and internals.

Algorithm 3: Primal Coarse Growth Algorithm

Input: an incomplete localization array **L** that maps fine-scale volumes to the containing primal coarse grid
Output: **L** modified to cover all fine-scale volumes iterative pressure solution, p_{it}.

```
create empty list of fine-scale volumes V
while any elements in L are equal to NaN do
    foreach coarse volume c in Ω^p do
        find the fine-scale volumes U which L[c] = NaN
        H ← fine-scale volumes neighbours with Ω_c^p
        F ← U ∩ H
        L[F] = c
```

Figure 55 – Construction of the primal and dual coarse mesh using a background grid.

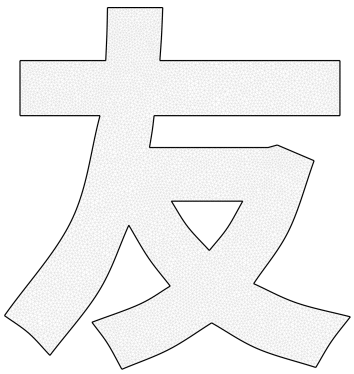

(a) Fine-scale discretization of the physical domain.

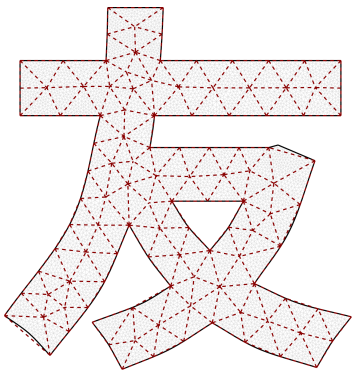

(b) Background grid over the high resolution discretization of the physical domain.

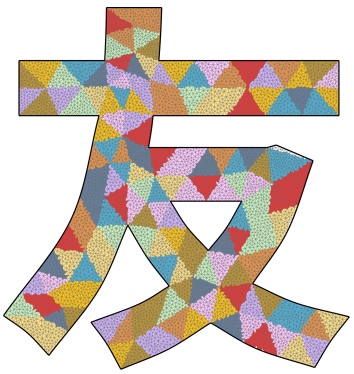

(c) Primal coarse grid candidate obtained locating fine-scale centroids inside each background grid cell.

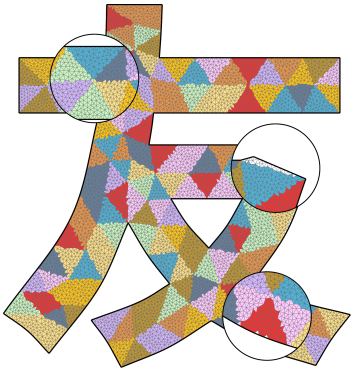

(d) Primal coarse candidate does not ensure that all fine-scale cells belong to a coarse volume nor face connectivities among fine-scales inside the same coarse volume.

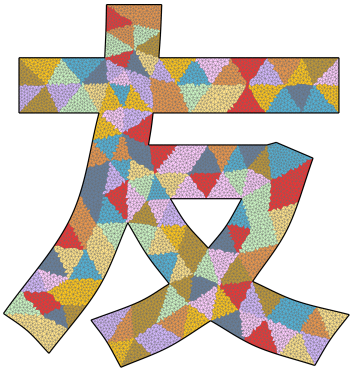

(e) Algorithm 3 and 4 fixes the aforementioned problems by relocating fine-scale cells among primal coarse-volumes.

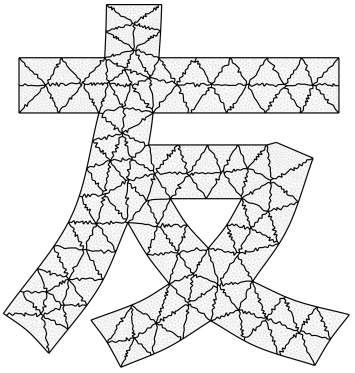

(f) The primal coarse grid candidate becomes the primal coarse mesh.

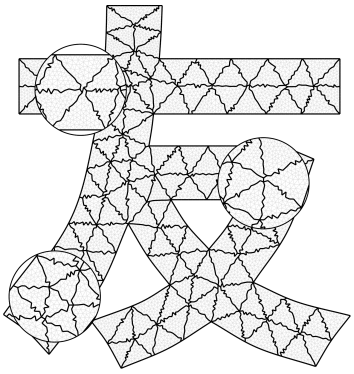

(g) The primal coarse grid introduce coarse-scale face connectivities not presented among the background grid cells.

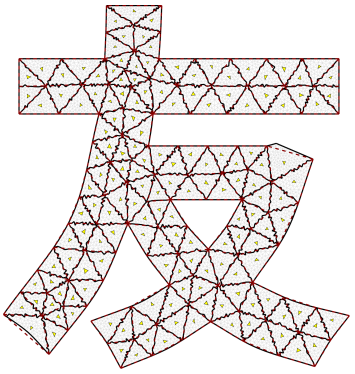

(h) Primal coarse cell centres are calculated using the background grid centroids.

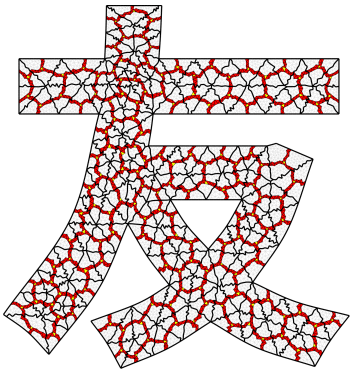

(i) Dual coarse grid is defined ignoring primal coarse face connectivities not presented on the background grid.

Source: (SOUZA et al., 2022).

Algorithm 4: Primal Coarse Growth Algorithm

Input: a localization array **L** that maps all fine-scale volumes to the containing primal coarse volumes
Output: **L** modified to ensures all fine-scale volumes share at least a common surface.

```
create empty list of fine-scale volumes V
foreach tag c in L do
    create a graph G_c where the nodes are the fine-scale volumes in Ω_c^p and the
     edges the face neighbours connectivities.
    split G_c into unconnected sub-graphs H
    F ← sub-graphs in H except the one with the highest cardinality
    add fine-scale volumes in F to V
L[V] ← NaN
foreach tag c in L do
    n ← face neighbours of i
    L[i] ← mode(L[n])
```

Algorithm 5: Dual Grid Generation

Input: primal coarse mesh Ω^p, fine-scale mesh Ω, background grid
Output: edges of the multiscale dual-grid Ω^d

```
create an array ω containing the distance between each face connected volume
 in Ω
foreach coarse volume Ω_k^p in Ω^p do
    create a graph G_c with graph nodes (∀Ω_m ∈ Ω_k^p) and the graph edges (Ω_r, Ω_s
     | Γ_j = Ω_r ∩ Ω_s, ∀Γ_j ∈ Ω_k^p )
    get distance ω_k^c among all fine-scale volumes in Ω_k^c from ω
    targets ← fine-scale volumes neighbours to interfaces centres of the
     background grid and inside c
    source ← x_c^p
    foreach target in targets do
        sub-edge ← Dijkstra(source,target, G_c, w_c)
        add sub-edge to edges
```

APPENDIX B – RESUMO EXPANDIDO

Métodos Conservativos Multescala para o escoamento Multifásico em Reservatórios Petrolíferos Altamente Heterogéneos usando malhas não estruturadas

B.1 Introdução

As simulações computacionais desempenham um papel crucial no gerenciamento de reservatórios de petróleo em subsuperfície. Com o uso de simuladores é possível prever o complexo comportamento do escoamento do petróleo mesmo em meios porosos altamente anisotrópicos e heterogêneos com o intuito de otimizar as taxas de produção de maneira a maximizar o retorno econômico. Técnicas de otimização e ajuste histórico fazem uso extensivo de simulações para melhor compreender e antecipar diferentes cenários e o seu impacto associado as curvas de produção, que são extremamente dependentes das condições de fluxo dadas nos poços de injeção e produção. Por outro lado, os avanços recentes no campo de caracterização tornaram possível a integração de dados petrofísicos em escalas com ordens de magnitude superior a escala utilizada por simuladores de reservatórios de petróleo comerciais (ZHOU; TCHELEPI, 2008; LUNATI; JENNY, 2006; LUNATI; JENNY, 2008; LUNATI; TYAGI; LEE, 2011; MOYNER; LIE, 2015). Além disso, a geometria complicada e a grande heterogeneidade intrínseca a reservatórios não convencionais adicionam um novo grau de complexidade às simulações, tornando-as mais intensas do ponto de vista computacional. Isso limita severamente o uso de modelos geológicos de alta resolução, o que por sua vez limita a precisão das simulações (SOUZA et al., 2020).

Para contornar estas restrições e para usufruir da escala de alta resolução, o método Multiscale Finite Volume (MsFV) foi desenvolvido (JENNY; LEE; TCHELEPI, 2003; JENNY; LEE; TCHELEPI, 2006; ZHOU; TCHELEPI, 2008). Esses esquemas geram conjuntos de funções base que são usadas para projetar o sistema de equações associado a escala de alta resolução no espaço de baixa resolução. O novo sistema é resolvido e depois projetado de volta na malha de alta resolução, calculando assim uma solução conservativa razoavelmente precisa (SOUZA et al., 2020). A ideia por trás deste e de outros métodos multiescala é que resolver um conjunto de sistemas localizados de alta resolução junto com um problema global em escala baixa resolução (LUNATI; TYAGI; LEE, 2011) é mais barato do que simulação direta na escala de alta resolução.

O sucesso do método MsFV na representação do fluxo de fluidos em meios porosos homogêneos e levemente heterogêneos levou ao desenvolvimento de novos estudos visando aprimorar vários aspectos do método original. Alguns autores focaram

na construção de modelos de poços multiescala (WOLFSTEINER; LEE; TCHELEPI, 2006; JENNY; LUNATI, 2009); outros no estudo de técnicas para incorporar modelos físicos mais complexas ao modelo de reservatório (LUNATI; JENNY, 2008; LUNATI; JENNY, 2006; LEE; WOLFSTEINER; TCHELEPI, 2008; HAJIBEYGI; JENNY, 2009; HAJIBEYGI; TCHELEPI, 2014), assim como na melhoria das condições de contorno dos problemas localizados (WANG; HAJIBEYGI; TCHELEPI, 2015). Além disso, inspirado por métodos multigrid, Zhou & Tchelepi (2008) desenvolveu uma descrição matricial para o estágio de prolongamento e restrição, criando o que se tornou a notação padrão do MsFV. Neste método, os algoritmos multiescala são escritos como uma série de operações matriciais simples utilizando estes operadores.

Apesar de todos esses esforços, a família de métodos Multiscale Finite Volume padrão ainda sofre com problemas ao simular reservatórios altamente heterogêneos e anisotrópicos (HAJIBEYGI et al., 2008). Para garantir que a solução multiescala convirja para a solução de escala fina dentro de uma certa tolerância, desenvolveu-se uma família de métodos iterativos (HAJIBEYGI et al., 2008; HAJIBEYGI; JENNY, 2011a; LUNATI; TYAGI; LEE, 2011).

O Algebraic Multiscale Solver (AMS) (ZHOU; TCHELEPI, 2011; WANG; HAJIBEYGI; TCHELEPI, 2014) generalizou o esquema clássico Multiscale Finite Volume e tornou-se seu sucessor moderno. Neste método, a partir de uma simples notação matricial é possível calcular os operadores de prolongamento multiescala e um conjunto de funções de correção através uma série de operações algébricas diretas realizadas no sistema de equações discreto da malha de maior resolução. Combinado a um método multiescala iterativo, este método mostrou-se eficiente e robusto, com resultados comparáveis aos métodos multigrid (WANG; HAJIBEYGI; TCHELEPI, 2014). Vários autores modificaram com sucesso o AMS para incorporar novos recursos, como modelos de fraturas incorporados (ŢENE; KOBAISI; HAJIBEYGI, 2016), física mais complexa (ŢENE; WANG; HAJIBEYGI, 2015), simulações multiníveis multiescala (CUSINI et al., 2018; HAJIBEYGI et al., 2020) e fornecer uma estrutura geral parar permitir a integração de novos modelos de forma unificada (CORTINOVIS; JENNY, 2017).

No entanto, estes métodos não são compatíveis a malhas não estruturadas. Isso ocorre devido a três fatores: a Two-Point Flux Approximaton (TPFA), aproximação de fluxo de dois pontos, padrão nesses métodos é consistente apenas em malhas k-ortogonais; as dificuldades em generalizar os algoritmos de criação das entidades multiescala, como as malhas grosserias primais e duais, e a falta da definição adequada dos operadores multiescala para este tipo de malha (SOUZA et al., 2020).

O trabalho de Moyner & Lie (2013) abordou este segundo tópico e desenvolveu uma generalização do MsFV para lidar com malhas multiescala de baixa resolução não estruturadas. Moyner & Lie (2015) foi além e desenvolveu novos algoritmos para defini-

ção das malhas multiescala assim como um novo operador de prolongamento criando portanto o Multiscale Restriction-Smoothed Basis (MsRSB), que é consistente apenas em malhas grosseiras não estruturadas. Bosma et al. (2017) trabalhou na extensão do multiscale as entidades multiscale, e desenvolveu um operador de prolongamento para malhas não estruturados com *rescaling*. Já Mehrdoost (2019) e Mehrdoost (2021) estudaram técnicas para criar malhas grosserias duais e primais adaptáveis e não estruturadas.

Apesar de contribuições significativas, esses métodos carecem de uma aproximação de fluxo realmente consistente para problemas anisotrópicos em malhas não estruturadas quaisquer. Neste contexto, vários autores tem se dedicado a construir novas aproximações de fluxo, chamadas de Control Volume Distributed Multipoint Flux Approximations (CVD-MPFA), para super as limitações do TPFA (CRUMPTON; SHAW; WARE, 1995; AAVATSMARK et al., 1998; EDWARDS; ROGERS, 1998; CARVALHO; WILLMERSDORF; LYRA, 2007a; EDWARDS; ZHENG, 2008; CHEN et al., 2008; GAO; WU, 2010; FRIIS; EDWARDS, 2011; CONTRERAS et al., 2016; CONTRERAS; LYRA; CARVALHO, 2019; EDWARDS; ZHENG, 2010). A monotonicidade é uma propriedade importante desejada por autores de métodos numéricos. Em reservatórios de petróleo altamente anisotrópicos, a perda de monotonicidade pode levar a soluções que violem as restrições de entropia (YUAN; SHENG, 2008), fazendo com que o óleo flua de regiões de baixa pressão para pressões mais altas. Em meios com altas taxas de anisotropia e variações de permeabilidade, a perda de monotonicidade também pode levar à ocorrência de pressões absolutas negativas. No entanto, a monotonicidade não é suficiente para garantir que uma solução discreta não tenha oscilações espúrias. Em contraste, métodos que obedecem ao Princípio do Máximo Discreto (PMD) produzem soluções discretas livres dessas oscilações indesejadas. Para isso, se um método numérico linear tem uma matriz do tipo M-Matrix, então isso seria condição suficiente para garantir que a solução tenha um PMD local (EDWARDS; ZHENG, 2010). O método TPFA clássico aplicado à equação de pressão produz uma M-Matrix e como consequência tem soluções discretas livres de oscilações espúrias. No entanto, o método é inconsistente em malhas não K-ortogonais, o que ocorre quando campos tensores completos ou malhas não estruturadas são utilizadas.

Já os métodos CVD-MPFA mais recentes com Full Pressure Support (FPS) e.g. (EDWARDS; ZHENG, 2010; GAO; WU, 2010) e os métodos anteriores com Triangular Pressure Support (TPS) CVD-MPFA têm DMP e M-Matrix condicionais. Para alguns casos de teste cujos tensores de permeabilidade são altamente anisotrópicos e cheios, todas as formulações de CVDM-MPFA não têm DMP local. Entretanto apenas os métodos do tipo TPS e anteriores induzem oscilações espúrias graves. Este comportamento é atribuído ao desacoplamento (EDWARDS; ZHENG, 2008; EDWARDS; ZHENG, 2010) onde foi feita uma análise para explicar este fenômeno e demonstrado que as formulações FPS não sofrem deste desacoplamento podendo calcular soluções livres das oscilações

não físicas a nível da malha, apesar da falta de um DMP local formal em tais casos.

B.1.1 Objetivos Principais

Neste contexto, o objetivo geral deste trabalho é investigar e desenvolver esquemas multiescala conservativos para simulação 2-D e 3-D de escoamentos multifásicos em meios porosos heterogêneos e anisotrópicos utilizando malhas não k-ortogonais.

Objetivos Específicos

1. Investigar e desenvolver algoritmos para a criação de entidades geométricas multiescala em 2-D e 3-D.
2. Implementar esquemas de aproximação de fluxo linear e não linear para a discretização da equação de pressão.
3. Investigar e desenvolver um esquema multiescala para simulação de escoamentos multifásicos em reservatórios de petróleo altamente heterogêneos e anisotrópicos consistentes em malhas gerais não estruturadas.

B.2 Equações Governantes

A ideia principal deste capítulo é discutir brevemente o modelo matemático que governa o escoamento bifásico água-óleo em meios porosos. Como este tema já foi objeto de extensos estudos por nosso grupo de pesquisa e outros autores (SOUZA, 2018; CARVALHO, 2005; SOUZA, 2015; CONTRERAS, 2017; AZIZ; SETTARI, 1979), o foco aqui é apenas explicar os modelos e as equações diferenciais parciais (EDPs) que descrevem este modelo. Para encontrar as equações a seguir, manipula-se a lei de conservação de massa juntamente com a lei de Darcy para o escoamento de fluido em meios porosos totalmente saturados, assumindo que o petróleo é um fluido newtoniano imiscível, incompressível e isotérmico escoando através de um meio totalmente saturado com compressibilidade desprezível. Além disso, efeitos térmicos, de capilaridade e reações químicas entre fases não são levados em consideração. Por fim, desprezamos os efeitos de dispersão e adsorção. O modelo matemático resultante descreve um escoamento bifásico, água-óleo, usando duas EDPs diferentes, uma equação elíptica (pressão) e uma hiperbólica (saturação).

B.3 Formução de Volumes Finitos

O conjunto de EDPs descrito no capítulo anterior governa o comportamento do escoamento de fluidos em reservatórios porosos. No entanto, assim como acontece com a maioria dos fenômenos, a complexidade das equações diferenciais faz com

que soluções analíticas sejam possíveis apenas com várias condições simplificadoras, ou atualmente impossíveis de serem resolvidas. Desta forma, os métodos numéricos aparecem como uma alternativa viável, pois permitem obter soluções aproximadas dentro de uma certa tolerância desejada. Nesse contexto, simuladores de reservatórios de petróleo são uma ferramenta fundamental para o gerenciamento de reservatórios de petróleo subterrâneos. A peça fundamental desses simuladores são os método do tipo Volumes Finitos (VF) ou Finite Volumes (FV), em inglês, uma família de esquemas localmente conservativos, cujo membro mais conhecido é o esquema TwoPoint Flux (TPFA). As principais vantagens do TPFA em relação a outros métodos são sua eficiência, simplicidade e a garantia de soluções livres de oscilações espúrias, pois este esquema satisfaz o Princípio do Máximo Discreto (PMD). Isso acontece porque métodos capazes de gerar uma matriz do tipo M-Matrix, como o TPFA, garantem soluções com PMD local (EDWARDS; ZHENG, 2010). No entanto, este esquema falha em produzir uma solução consistente para malhas não k-ortogonais e para meios com tensores de permeabilidade total. Esses problemas foram superados pela primeira vez quando dois grupos de autores (EDWARDS; ROGERS, 1998; AAVATSMARK et al., 1998) , separadamente, generalizaram o trabalho de Crumpton, Shaw & Ware (1995) e criaram a família Control Volume Distributed (CVD), também conhecida como MultiPoint Flux Approximation (MPFA), para trabalhar em malhas não estruturadas. Com o sucesso deste novo ramo de métodos lineares de volumes finitos, vários autores se dedicaram a melhorar e criar novos métodos do tipo CVD-MPFA (EDWARDS; ZHENG, 2008; CHEN et al., 2008; GAO; WU, 2010; CONTRERAS et al., 2016; CONTRERAS; LYRA; CARVALHO, 2019). No entanto, qualquer esquema linear que seja mais acurado que um esquema com aproximação de primeira ordem pode levar a extremos locais de acordo com o teorema de Godunov. Isto é, esses métodos não garantem o PMD. No contexto de simulação de reservatórios subterrâneos de petróleo, as oscilações espúrias causadas pela perda de PMD podem levar ao aparecimento de bolsões virtuais de gás quando a pressão cai abaixo do ponto de bolha levando o óleo a fluir de zonas de baixa para alta pressão(QUEIROZ et al., 2013). Vale a pena notar que os esquemas CVD-MPFA modernos com suporte de pressão total, por exemplo, (EDWARDS; ZHENG, 2010; GAO; WU, 2010) e suporte de pressão triangular anterior conseguem gerar M-Matrix sob determinadas condições e, portanto, PMD local condicionado. Ainda assim, meios com tensores completos, anisotropia e fortes variações no campo de permeabilidade podem fazer com que esses métodos percam o PMD. Neste capítulo, apresentamos os esquemas membros da família de volumes finitos centrados na célula e empregados neste trabalho para aproximar a solução das PDEs mencionadas. Neste capitulo, descrevemos brevemente os tópicos utilizado nesta tese. Primeiramente, começamos apresentando os aspectos comuns dos esquemas de Volume Finito (FV), descrevemos posteriormente os métodos TPFA e a MPFA com um estêncil Diamante (CVD-MPFA-D), apresentamos o esquema

semi-implícito M-Matrix Flux Splitting (EDWARDS, 2000) e por fim apresentamos a nossa formulação Flux Limited Splitting.

B.3.1 MPFA-D com estêncil Diamante

A aproximação de fluxo por múltiplos pontos com estêncil diamante (MPFA) é um método não ortodoxo membro da família CVD-MPFA. Ele foi desenvolvido originalmente por Gao & Wu (2010) e trazido para o contexto de escoamento multifásico por Contreras et al. (2016). Assim como outros métodos da família MPFA, o MPFA-D foi desenvolvido para lidar com as limitações TPFA clássico. Semelhante ao MPFA-FPS (FRIIS; EDWARDS, 2011), o diamante possui suporte de pressão total para cada subcélula do domínio discreto. Como consequência, este método não sofre tão severamente com desacoplamento. Assim, as suas soluções são bem comportadas e consistentes com oscilações espúrias significativamente menos visíveis em comparação com os métodos CVD-MPFA anteriores.

B.3.2 M-Matrix Flux Splitting

O M-Matrix Flux Splitting é uma técnica proposta por (EDWARDS, 2000) para formulações CVD-MPFA que divide a matriz CVD-MPFA em termos do fluxo TPFA e do fluxo dos termos de difusão cruzada (TDC) dando origem a um esquema iterativo semi-implícito que garante a conservação de massa a cada iteração. No contexto de Volume Finito, M-Matrix diagonalmente dominantes são obtidas com o operador discreto mais comum, o TPFA. No entanto, a maioria dos problemas relacionados a reservatórios de petróleo requerem uma aproximação de fluxo consistente para meios anisotrópicos que geralmente não estão alinhados com os eixos principais da malha (EDWARDS; ZHENG, 2010). A ideia principal do método M-Matrix Flux Splitting é criar um esquema semi-implícito que explore o recurso de convergência rápida da propriedade M-Matrix do TPFA, onde a única matriz a ser invertida é uma matriz M definida positiva simétrica, mesmo em malhas não estruturadas.

B.3.3 Flux Limited Splitting não linear

O Flux Limited Splitting (FLS) é uma generalização não linear do método de (EDWARDS; ZHENG, 2010; PAL; EDWARDS, 2006; PAL; EDWARDS, 2011) proposta por nós. A ideia deste método é desenvolver uma técnica geral de reparo para métodos lineares do tipo CVD-MPFA com base no M-Matrix Flux Splitting, mas limitando a quantidade de difusão cruzada do método MPFA original de forma a melhorar ou restaurar o DMP, sem perder a conservação de massa

B.4 Formução Multiescala

Os métodos multiescala são uma família de métodos aproximados baseados em técnicas de transferência de escala que permitem o uso de malhas de alta resolução mesmo em simulações de reservatórios comerciais. Ao contrário das técnicas de upscaling que transfere informação de uma escala de alta resolução e permanece na escala de baixa resolução, os métodos multiescala criam um conjunto de operadores para projetar o sistema de equações de escala fina no espaço da malha de escala grosseira. O novo sistema é então resolvido e posteriormente, se necessário, projetado de volta no espaço da malha de alta resolução para calcular uma solução conservativa razoavelmente precisa (SOUZA et al., 2020). A ideia por trás deste e de outros métodos multiescala é que resolver uma série de sistemas locais de alta resolução com um problema global em escala de menor resolução (LUNATI; TYAGI; LEE, 2011) é mais barato do que uma simulação direta na escala de alta resolução. Os métodos do tipo Multiscale Finite Volume (MsFV) são um subconjunto dos métodos multiescala com graus de liberdade centrados nas células, capazes de gerar soluções conservativas em qualquer escala da simulação(LUNATI; JENNY, 2006; ZHOU; TCHELEPI, 2008; JENNY; LUNATI, 2009; LUNATI; JENNY, 2008; LEE; WOLFSTEINER; TCHELEPI, 2008). Além disso, a família multiescala iterativa é capaz de fazer a solução multiescala aproximada convergir para a solução a solução da escala fina(HAJIBEYGI et al., 2008; HAJIBEYGI; JENNY, 2011a; LUNATI; TYAGI; LEE, 2011). Dessa forma, os métodos multiescala podem ser aplicados de três maneiras diferentes: i) como uma técnica robusta de upscaling, ii) como um método para aproximar a solução de escala fina e iii) como uma solução inicial de um método procedimento iterativo de maneira a garantir que a solução multiescala convirja dentro de uma certa tolerância para a solução da simulação em escala fina (ZHOU; TCHELEPI, 2008; SOUZA et al., 2020). Esta seção apresenta a formulação e os métodos associados usados para derivar o Algebraic Multiscale Solver for Unstructured grids (AMS-U), formulação multiescala desenvolvida por nós nesta tese. Os algoritmos de pré-processamento multiescala são apresentados nos apêndices onde apresentamos a estratégia Background Grid desenvolvida por nós para construção e preprocessamento das malhas primais e duais multiescala.

B.5 AMS-U

O Algebraic Multiscale Solver (AMS) (WANG; HAJIBEYGI; TCHELEPI, 2014) é um método moderno que surgiu da generalização do método Multiscale Finite Volume (JENNY; LEE; TCHELEPI, 2003; JENNY; LEE; TCHELEPI, 2006; ZHOU; TCHELEPI, 2008). A notação matricial simples permite que o operador de prolongamento e um conjunto de funções de correção sejam calculados através de uma série de operações algébricas diretas executadas nas matrizes do sistema de equações para a malha de

alta resolução. Combinando esta técnica a uma método multiescala iterativo, temos um esquema numérico eficiente e robusto com resultados comparáveis aos métodos multigrid (WANG; HAJIBEYGI; TCHELEPI, 2014). Nesta seção, derivamos o Algebraic Multiscale Solver for Unstructured Grids (AMS-U), uma generalização do AMS para a simulação de escoamento multifásico em meios porosos heterogêneos e anisotrópicos em malhas não estruturadas. O método resolve os três problemas principais necessários para simulação multiescala em malhas não estruturadas: i) a técnica do Background grid é utilizada para construção da malha primal e dual multiescala, ii) utlizamos a aproximação de fluxo do tipo MPFA-D; e iii) generalizamos os operadores do AMS e os modificamos para evitar o vazamento das funções de base fora de suas respectivas regiões de suporte. Por fim, adaptamos procedimentos iterativos (ŢENE; KOBAISI; HAJIBEYGI, 2016; BOSMA et al., 2017; MOYNER; LIE, 2015) e usamos para melhorar a qualidade da solução multiescala diminuindo os erros de alta frequência.

B.6 Resultados

Esta seção é dedicada a testar as formulações desenvolvidas por nós nos capítulos anteriores. Para isso, diversos problemas de referência da literatura foram adaptados para o contexto de malhas não estruturadas com intuito de testar os métodos numéricos desenvolvidos por nós. Na primeira seção, apresentamos os resultados do Flux Limited Splitting acoplado ao MPFA-D para simulação de fluxo monofásico em meios altamente heterogêneos e anistrópicos. Na seção seguinte apresentamos os resultados do Algebraic Multiscale Solver for Unstructured Grids para escoamentos monofásicos e bifásicos do tipo água-oleo.

B.7 Conclusões

No presente trabalho, investigamos e desenvolvemos formulações do tipo volumes finitos centrados na célula células. Nosso trabalho foi dividido em dois grupos: o estudo de aproximações de fluxo consistentes em malhas não estruturadas que respeitam o PMD e o estudo de métodos multiescala conservativos. Ambas as formulações resultantes foram usadas para resolver problemas monofásicos de escoamentos incompressíveis em meios altamente heterogêneos e anisotrópicos, mas a última também foi testado para problemas de escoamento bifásico em domínios desafiadores. Neste caso, usamos uma estratégia implícita sequencial na qual a solução de pressão e as equações de saturação são resolvidas separadamente. No primeiro grupo, investigamos e estudamos técnicas de aproximação de fluxo não lineares consistentes em malhas não estruturadas. Desenvolvemos com sucesso uma nova técnica de reparo para métodos lineares MPFA baseados no M-Matrix Flux Splitting (EDWARDS, 2000) que é capaz de converter esses esquemas em métodos não lineares que obedecem ao Princípio do

Máximo Discreto. Esta estratégia foi testada usando o MPFA-D para malhas 2D não estruturadas com a interpolação LPEW2. O método foi testada em problemas benchmark levando o MPFA-D original ao seu limite. Nosso método foi capaz de produzir soluções que reproduziram qualitativamente a qualidade da formulação do MPFA mas respeitando o PMD. No entanto, em alguns exemplos, observou-se que nosso método adicionou mais difusão artificial para isso. Vale salientar, que nosso método foi desenvolvido usando um operador matemático criado por nós que permite que a matriz de transmissibilidade seja escrita como uma multiplicação da matriz do nosso operador e a matriz de transmissibilidade de face. Desta forma, o balanço de massa é realizado de maneira inteiramente matricial. Este operador permitiu a vetorização do código, o que aumenta o desempenho do nosso método. Os resultados de nossa formulação foram comparáveis aos métodos TPFA não lineares de última geração.

Quanto ao segundo grupo, investigamos e desenvolvemos métodos e algoritmos necessários para a simulação de métodos multiescala da tipo MsFV em malhas não estruturadas. Em particular, desenvolvemos uma generalização do Algebraic Multiscale Solver (WANG; HAJIBEYGI; TCHELEPI, 2014) para malhas não estruturadas. Isso foi feito desenvolvendo a Background Grid strategy, uma nova técnica que usa uma malha adicional para ajudar na criação das malhas multiescala em 2-D e 3-D, usando um MPFA para a escala fina e modificando os operadores do AMS clássico para garantir que as funções bases sejam restritas às suas respectivas regiões de suporte. Combinado com um estágio de suavização iterativo, nosso método mostrou-se ser consistente mesmo em meios altamente heterogêneos e anisotrópicos. Além disso, nossa formulação é a técnica mais flexível para criação de malhas multiescala, pois é capaz de fazer uso de malhas não estruturadas que adaptam as características geométricas de domínios físicos complexos. Por fim, os resultados positivos obtidos nos motivam a realizar novas pesquisas para aprimorar e estender as formulações para problemas mais gerais. Em particular, os algoritmos de ambos métodos construídos foram desenvolvidos de tal forma que podem ser facilmente estendidos para 3-D. Citamos assim como possíveis extensões futuras de nosso trabalho:

1. Estender o FLS para 3-D.
2. Investigar novos algoritmos para limitar os termos de difusão cruzada.
3. Investigar e comparar formulação FLS com outros métodos robustos de aproximação de fluxo capazes de lidar com malhas não estruturadas como MPFA-H, FPS etc.
4. Estender a estratégia background grid para se adaptar automaticamente ao campo de permeabilidade do meio de maneira a melhorar a solução multiescala.

5. Acoplar a estratégia FLS com esquemas multiescala criando assim métodos que multiescala que respeitem o PMD.

6. Estender o AMS-U para 3-D.